ABSTRACT

Title of dissertation: TUNNELING PROPERTIES AND ELECTROMAGNETIC RESPONSE IN IRON BASED SUPERCONDUCTORS AND OTHER SYSTEMS

Tamoghna Barik, Doctor of Philosophy, 2023

Dissertation directed by: Professor Jay Deep Sau
Department of Physics, University of Maryland

An iron-based chalcogenide compound, $FeTe_{1-x}Se_x$ (FTS), has recently attracted attention as a potential candidate for a readily available platform for hosting the exotic topological superconducting (TSC) phase on its surface. In its 3D sample the co-existence of the strong topological insulating (TI) phase and cylindrical Fermi sheets provide the two necessary ingredients for the TSC phase on its surface - i) the topologically protected helical surface states and ii) the intrinsically induced s-wave pairing from the bulk superconductivity.

The strong TI phase in the FTS alloy is crucially dependent on the relative composition ratio between Te and Se atoms. The topological FTS sample, $FeTe_{.55}Se_{.45}$, that is widely studied for having the highest critical temperature (T_c) in this class, interestingly, lies close to the topological-trivial phase boundary (estimated to be close to $x = .5$ as observed by a recent experiment [1]). Furthermore, due to its alloy nature a typical sample of FTS suffers from spatial inhomogeneity in Te/Se composition at multiple length scales ranging from few nm to 100 μm. Thus, in a topological FTS sample there might be patches where the phase is driven out of its topological natures

due to the local deficit of Te composition induced by Te/Se fluctuations. Such trivial domains would be scattered throughout the sample - hence, we call such a phase a topological domain disordered phase. The trivial domains in such a disordered sample would inflict inhomogeneity in the topological surface state (TSS) density distribution which we study in Chapter 2 of this thesis. After carefully exploring the effects of topological domain disordered phase in an effective model of FTS, we conclude that the non-topological domains on the surface are characterized by suppressed local density of states (LDOS) surrounded by ridges of enhanced LDOS throughout the energy range of the Dirac dispersion of the TSS. Moreover, the appropriately scaled LDOS at various energies within the Dirac window collapse on each other for a given disordered sample which, as we show, is in stark contrast to the case of conventional chemical potential disorder. Hence, these features are expected to appear in measurements of tunneling conductance such as in scanning tunneling spectroscopy (STS) of the FTS surface when the sample is not in the superconducting phase.

Another kind of exotic modes, namely the helical Majorana modes, appear in the 2D TSC phase at a linear defect when the TSC gap on either side differs by a phase difference of π from the other side - thus, forming a π shifted Josephson junction (JJ) on the TSC surface. Signatures of such helical Majorana modes have been observed by a recent tunneling experiment on the surface of FTS. In FTS such signatures are characterized by the non-zero flat density of states (DOS) in an STS measurement at a crystalline domain wall (DW) which is associated with the in-plane half-unit-cell-shift (HUCS) of the lattice. Such non-zero flat DOS within the SC gap which is consistent with the existence of linearly dispersing 1D modes is absent in the non-topological

FeSe sample - hinting towards the topological origin of the same in FTS. Even though the TSC phase on the surface is expected in FTS, the origin of a π shifted order parameter that is crucial to accommodate the helical Majorana modes at the DW, is yet to be fully understood. In chapter 3 of this thesis we propose a mechanism that stabilizes a π-junction at the HUCS domain wall when the intrinsic superconducting pairing is of $s_{\pm}$ character as is the case for bulk FTS superconductivity that consists of hole-like pockets around Γ and electron-like pockets around M point of the Brillouin zone (BZ). We argue that if the DW induces inter-pocket transmission between the Γ and M pockets strongly enough, the coupling between the order parameters (OPs) of the two pockets (Γ and M) is also enhanced. Since the $s_{\pm}$ nature of the pairing implies an intrinsic π-phase difference between the OPs associated with the Γ and M pockets, strong DW-induced coupling between them can stabilize a Josephson junction with π-phase shift. We explore the possibility of such π-junction in FTS by constructing an effective model of the Fermi surface of FTS and computing the Bogoliubov-de-Gennes (BdG) spectrum with $s_{\pm}$ pairing at the HUCS DW. Varying our model parameters within the regime of the observed FTS Fermi surface we find that for a wide range of parameters the π-junction accommodates Andreev bound states (ABSs) that have lower occupied energies than those for trivial 0-phase shifted junction. Simultaneous numerical computation of the DW-induced scattering problem reveals that the strong inter-pocket transmission strength is positively correlated with the stability of the π-junction, supporting our proposed mechanism for the π-junction stability as described earlier. Such π-Josephson junctions can in principle be detected using superconducting quantum interference device (SQUID) using either a mesoscopic

device or corner junction.

In the next chapter 4 of the thesis we consider another setup of Josephson junction (JJ) consisting of an interacting one-dimensional quantum wire sandwiched between two semi-infinite SC leads of conventional s-wave pairing. The low energy Physics of such interacting 1D system which is known as Luttinger liquid (LL) is controlled by the two decoupled sets of eigen modes - namely, the charge and spin density waves. The SC leads in such a JJ thus allow easy access to the charge degrees of freedom in the LL - also known as plasmons which can also be probed optically using near field optical microscopy [2, 3]. An interesting aspect of an S-LL-S setup is that the NS interface blocks the flow of spin current due to the perfect Andreev reflection at low energies. Hence, the spin modes of the LL would typically be obscure to a transport measurement due to the aforementioned spin-charge decoupling. Hence, a conductivity measurement would not be able to detect the spin degrees of freedom if they are separated from the charge modes. However, we note that the impurity induced back-scattering processes which involve low energy but large momentum transfer can couple the spin and charge densities in the LL and we study the signatures of such spin-charge coupling in the electromagnetic (EM) response measurements. In our numerical evaluation which incorporates the impurity potential perturbatively and we calculate the resultant EM absorption spectrum using linear response theory which is measurable in a similar S-LL-S setup. We find that the signatures of back-scattering induced spin-charge coupling appear in the absorption spectrum as excitation peaks at the energies that are associated with the spin excitations of the LL. Tuning the total density of the 1D system and hence the Fermi momentum we find a regime where the

spin peaks are roughly of equal amplitude as that of the charge peaks. Since in a 1D wire the density can be tuned by means of gating [3], such regime is accessible to a transport measurement. In that regime tuning the Coulomb interaction strength one can distinguish the charge peaks as they shift on the energy axis whereas the spin peaks are insensitive to such interaction strength variation. We conclude that such impurity induced signatures of spin modes can thus be probed in an S-LL-S setup by investigating the EM response of the sample in a conductivity measurement.

In the last chapter 5 of the thesis we go beyond the regime of linear response formalism that is discussed in relation to the EM response of the S-LL-S setup in the previous paragraph and consider the optical response up to second order in the applied EM field. A fundamental feature of non-linear response is its non-equilibrium nature which is absent in linear responses. Such non-equilibrium character is manifested as the out-of-time-ordered correlators (OTOC) in response theory associated with the second power of the applied EM field magnitude. Such correlators for a generic interacting system cannot be described using the standard Feynman diagrams, rather one requires its non-equilibrium extension which is known as the Keldysh formalism. We focus on this non-equilibrium nature of the response by considering the bulk photovoltaic effect (BPVE) in a non-centrosymmetric system where we include electron-phonon (e-ph) coupling as the mode of relaxation. Considering the semi classical limit where the e-ph scattering is stronger than the applied field strength we show how the contribution of the OTOC appears in the BPVE induced DC current measurement when the system is illuminated by an inhomogeneous profile of optical intensity similar to the case of a irradiation on a finite portion of the sample. We also introduce the Floquet master

equation approach to treat the e-ph coupling quantum mechanically and demonstrate a shift in the scaling of the DC response from quadratic to linear in the limit of the e-ph coupling strength being much smaller than the applied EM field.

TUNNELING PROPERTIES AND ELECTROMAGNETIC RESPONSE IN IRON BASED SUPERCONDUCTORS AND OTHER SYSTEMS

by

Tamoghna Barik

Dissertation submitted to the Faculty of the Graduate School of the
University of Maryland, College Park in partial fulfillment
of the requirements for the degree of
Doctor of Philosophy
2023

Advisory Committee:
Prof. Jay D Sau, Chair/Advisor
Prof. Sankar Das Sarma
Prof. Victor Yakovenko
Prof. Maissam Barkeshli
Prof. Ichiro Takeuchi, Dean's representative

Acknowledgments

Throughout this journey to complete my PhD thesis there have been many people around me both in my academic environment and in my personal life. I am grateful for all the interactions that I have had with all of them as well as experiences I had with them.

First and foremost I'd like to mention the immense support I have received from my advisor, Prof. Jay Deep Sau. Starting from my TA ship in my beginning year of my graduate life, he has been advising to start and shape my research profile and at the same time gain important skills of critical and objective thinking. Then on I have been working with him for six years and he has always been available for academic and career suggestions. He has always reached out to me at times to point out my mistakes which gave me insight for later times.

Besides, prof. Sau, I have also had chance to work with two postdoctoral fellows in our group, Dr. Yang-Zhi Chou and Dr. Junhyun Lee who were very supportive besides being competent in their research capabilities. They have been quite friendly in discussions with me regarding research, at the same time providing personal experiences and thoughts/advice for my career path in general.

Needless to say, I owe my gratitude to other faculty members who I have interacted with as well. Prof. Maissam Barkeshli, Prof. Sankar Das Sarma, Prof. Victor Yakovenko, Prof. Ted Jacobson and Prof. Victor Galitski are to name only a few who have enriched me a lot with their technical knowledge and insights.

I would also like to specially thank Prof. Ichiro Takeuchi for serving as the Dean's

representative on my dissertation committee.

My fellow graduate students at our group have also been a valuable and integral part of my life throughout these years. I have shared lot of lively discussions with Yahya Alavirad, Yi-Hua Lai, Ali Lavasani, Subhayan Sahu, Naren Manjunath, Gautam Nambier, Jeet Shah who have provided me with wide perspectives regarding the ongoing topics of research and the techniques they use to tackle problems in areas outside my purview of particular interests.

I must thank the staff members who have been helpful with all administrative activities. A special thanks to Janet Das Sarma who has been a call for support to all the members at Condensed Matter theory center (CMTC) managing every needs of all the individuals with great pleasure and smile. I am also thankful to our current CMTC assistant, Erika Martin, for providing all necessary administrative services. Besides, I have been greatly helped by Josiland Chambers, Donna Hammer and Jessica Crosby at the Dept. of Physics. Also Danielle Watkins at the Physics payroll office has been very helpful handling payroll related responsibilities.

Besides these people, several fellow graduate students at the University of Maryland have been a close part of day to day life during this period.

Table of Contents

List of Figures

List of Abbreviations

ABS	Andreev bound state
ARPES	Angle resolved photo emission spectroscopy
BdG	Bogoliubov de-Gennes
BHZ	Bernevig-Hughes-Zhang
BZ	Brillouin zone
CdGM	Caroli-de Gennes-Matricon
DFT	Density functional theory
DOS	Density of states
DW	Domain wall
EDS	Electron diffraction spectroscopy
HUCS	Half-unit-cell-shift
LDOS	Local density of states
MBS	Majorana bound state
MZM	Majorana zero mode
OP	Order parameter
SC	Superconductor
SOC	Spin orbit coupling
STM	Scanning tunneling microscopy
STS	Scanning tunneling spectroscopy
TI	Topological insulator
TRIM	Time reversal invariant momentum
TRS	Time reversal symmetry
TSC	Topological superconductor
ZBP	Zero bias peak

Chapter 1

Outline of the thesis

In this introductory chapter we briefly outline the contents that are covered in the subsequent chapters of the thesis.

The potential of the topological qubits in performing fault-tolerant quantum computation has enhanced efforts for searching new materials with novel topological character as well as understanding the exotic signatures that are associated with them. To realize the fault-tolerant quantum computation a new platform has emerged in the past decade or so in the form of the three-dimensional strong topological insulator (TI) phase which is characterized by a $\mathbb{Z}_2$ invariant. The 2D surface of such a TI hosts topologically protected helical surface states which upon induction of s-wave pairing provides a platform for realizing topological qubits at the magnetic vortex cores. In that regard an iron-based chalcogenide compound, $FeTe_{1-x}Se_x$ (FTS), has attracted great attention due to the existence of the strong TI phase [4, 5, 6] as well as the intrinsically induced s-wave pairing on its surface from the bulk superconductivity [7, 8, 6, 9].

However, the strong TI phase in this material is controlled by the relative Te/Se composition percentage [5]. For example, $FeTe_{1-x}Se_x$ with $x = 0$ (i.e., FeSe) is topologically trivial whereas the widely studied sample with $x = .45$, i.e., $FeTe_{.55}Se_{.45}$ hosts the strong TI phase. The alloy nature of this material gives rise to inhomogeneity in the Te/Se composition throughout the sample. Along with that the sensitivity of

the topological phase to the Te/Se composition gives rise to a possible scenario where a topological FTS sample bears regions of trivial domains. The implication of such trivial domains in an overall topological sample near the surface can be quite interesting. The effects of such topological domain disordered phase is studied in Chapter 2 which is based on [10].

The topological superconducting (TSC) phase that exists on the surface of FTS when the sample is in the strong TI phase provides the possibility of another exotic phase boundary at linear defects when the TSC gaps on both sides of the defect differ by a phse of π. Such π-shifted Josephson junction (JJ) on the TSC phase captures helical Majorana modes that linearly disperse along the junction boundary. In a recent experiment [11] using scanning tunneling spectroscopy (STS) on the surface of FTS signatures of such helical Majorana modes have been found at a crystalline domain wall (DW) associated with half-unit-cell-shift (HUCS) of the lattice across the DW. The flat non-vanishing density of states (DOS) within the SC gap as observed at the DW - is consistent with the existence of the 1D dispersing helical Majorana modes. In addition, absence of such features when the sample is not in the topological phase, e.g., in FeSe, hints at the topological nature of the signature. However, given the TSC phase on the surface, the appearance of helical Majorana modes along a linear defect requires the TSC gap to flip sign across the defect [12]. In other words, the HUCS DW must accommodate a π-junction which naturally gives rise to the question regarding its origin. In Chapter 3 we provide a mechanism favoring such a π-junction along with its numerical justification in an effective model of FTS layer which is based on a manuscript [13].

In the next part of the thesis we consider Josephson junction (JJ) of a different kind which can be constructed by sandwiching an interacting one-dimensional (1D) quantum wire, known as Luttinger liquid (LL), between two semi-infinite superconducting (SC) leads. The SC leads provides easy access to the charge degrees of freedom in the LL which can also be probed optically using near field optical microscopy in single-walled carbon nanotube systems [2, 3]. A key effect of having semi-infinite SC leads is that the spin density modes in the LL regions gets trapped when the system is clean due to the perfect Andreev reflections that take place at the normal - superconductor (NS) interfaces. The implication of such spin opacity of the NS interfaces is that in conductivity measurement with such a setup would not be able to probe the spin excitations of the 1D wire. However, the impurity induced back-scattering potential can in principle couple the spin and charge density modes of the system [14]. In Chapter 4, based on [15], we investigate the signatures of such spin-charge coupling in the absorption spectrum which would generically contain peaks due to both spin and charge mode excitations.

In the last Chapter (Chapter 5) of the thesis, based on [16], we go beyond the regime of linear response as discussed in relation to the absorption spectrum of the JJ setup in the previous paragraph and focus on the non-linear responses. A key distinction between the linear and non-linear response is that the full second order response to an applied electromagnetic (EM) field involves correlators that are out-of-time-ordered [17]. Existence of such out-of-time-ordered correlators (OTOCs) in the response points to its non-equilibrium nature which is absent in linear responses. Considering the bulk photovoltaic effect (BPVE), where a DC current response is

generated in the bulk of a non-centrosymmetric system when irradiated by light which is proportional to second power of the applied field, as the example of a non-linear response we look into the non-equilibrium nature of this effect. We also investigate the scaling shift of the DC response from quadratic to linear by considering electron-phonon (e-ph) coupling in the limit when the applied field is much larger than the e-ph coupling strength.

Chapter 2

Signatures of non-topological patches on the surface of topological insulators

2.1 Introduction to strong topological insulating (TI) phase in FTS

In this chapter we investigate the signatures of the topological domain disordered phase which is characterized by trivial domains scattered throughout a topological sample. Such a phase might arise in a topological alloy sample such as $FeTe_{1-x}Se_x$ (FTS) where the sample suffers from composition fluctuations which can drive the phase out of its topological nature locally, thus, creating trivial domains spread across the sample. The results presented in this chapter is based on a published paper [10].

In three-dimensions the topological classification of time reversal ($\mathcal{T}$) invariant insulators can be characterized by four $\mathbb{Z}_2$ invariants that are denoted by $(\nu_0; \nu_1, \nu_2, \nu_3)$ [18]. We will define these invariants shortly, but let us briefly describe the topological classes associated with the possible values of the four invariants.

The insulators with

i) $\nu_0 = 1$ are classified as strong topological insulators (TIs),

ii) $\nu_0 = 0$ and $\nu_{i=1/2/3} = 1$ are called weak TIs,

and

iii) $\nu_{0,1,2,3} = 0$ are topologically trivial insulators that are equivalent to vacuum.

The strong TI phase hosts surface states that are topologically protected from disorder induced localization [19]. In contrary, even though the weak TIs possess surface states on certain surfaces they are not immune to such localization. In case of the strong TIs the surface states, in in-plane momentum space, have spin-momentum locked helical dispersion with a single Dirac point enclosed by surface Fermi arcs. The π Berry phase enclosed by the Fermi arc characterises the non-trivial phase that is topologically protected as long as the system maintains the TRS. In contrast, for weak TIs the Fermi arcs enclose even number of time-reversal invariant momenta (TRIM) on the surface Brillouin zone (BZ) which results in surface Berry curvature to be multiple of 2π or 0 equivalently. This in turn destroys the topological protection from the disorder induced localization [18].

2.1.1 $\mathbb{Z}_2$ invariants

The $\mathbb{Z}_2$ invariants mentioned above can be expressed in terms of Pfaffians of time reversal polarization (TRP) matrices at the time reversal invariant momenta (TRIM) of the bulk band structure [20]. Consider the 3D BZ of the TRS system and hence, there are 8 points that are invariant under TRS and thus, the bands are two-fold (or multiples of two) - fold degenerate at those points which form the Kramer's degenerate pairs. The TRIMs in the BZ can be represented as

$$\Gamma_i = \frac{1}{2}\left(n_1\mathbf{b_1} + n_2\mathbf{b_2} + n_3\mathbf{b_3}\right) \tag{2.1}$$

where $\mathbf{b_i}$s are the reciprocal lattice vectors and $n_i = 0, 1$.

The four invariants, $\nu_{0,1,2,3}$ are defined in terms of the sign of the Pfaffian of the

time reversal operator, Θ at the appropriate subsets of the TRIMs for the occupied bands.

Let us define [20]

$$\delta_i = \frac{\sqrt{\det[w(\Gamma_i)]}}{\mathrm{Pf}[w(\Gamma_i)]} = \pm 1 \tag{2.2}$$

where assuming N bands along with their Kramer's partners are occupied, w is a $2N \times 2N$ matrix given by

$$w_{mn}(\mathbf{k}) = \langle u_{m,-\mathbf{k}} | \Theta | u_{n,\mathbf{k}} \rangle \tag{2.3}$$

such that $|u_{n,\mathbf{k}}\rangle$ denotes the periodic part of the Bloch wave solution for the nth band at momentum $\mathbf{k}$.

In terms of δ_is the $\mathbb{Z}_2$ invariants are defined as [20]

$$\begin{aligned} (-1)^{\nu_0} &= \prod_{i=1}^{8} \delta_i \\ (-1)^{\nu_i} &= \prod_{n_k=1, n_{j\neq k}=0,1} \delta_{i=(n_1 n_2 n_3)} \end{aligned} \tag{2.4}$$

In addition to the TRS, if the system also obeys spatial inversion symmetry, the $\mathbb{Z}_2$ invariants determining the TI phases become particularly easy to calculate. In presence of inversion symmetry, the δ_i s in that case can be expressed as product of the parity eigen values of the Bloch states of the occupied bands under a certain Gauge choice [18] given by

$$\delta_i = \prod_{m=1}^{N} \xi_{2m}(\Gamma_i) \tag{2.5}$$

where ξ_{2m} is the parity eigen value of the $2m^{\text{th}}$ Bloch state.

Combining Eqs. 2.4 and 2.5 it is easy to see that a system would be a strong TI ($\nu_0 = 1$) when the number of odd parity eigen states combining all the TRIMs is odd. This criteria is relatively easier to test for a given material system since it requires checking only the parity eigen values of the occupied manifold in the subspace where hybridization with unoccupied bands take place via band crossing and gap openning. It turns out that at certain percentage of average Te/Se composition in the alloy $FeTe_{1-x}Se_x$ an odd parity and an even parity band hybridizes along the ΓZ line which gives rise to the strong TI phase in this material [5].

2.1.2 Topological superconductivity on the surface of strong TI

As we discussed that the helical surface states are protected from localization when the bulk possesses the strong TI phase, it provides a platform for realizing topological superconducting (TSC) phase. On the spin-momentum locked surface dispersion when an order parameter of even parity is induced the resultant superconducting phase is a non-trivial topological phase of matter which in 2D can be characterized by a $\mathbb{Z}$ invariant which denotes the number of chiral Majorana channels at its interface with vacuum. Such a TSC phase can also contain a zero energy particle-hole symmetric mode called Majorana zero mode inside a magnetic vortex. At the core of the vortex the TSC gap is killed and thus effectively forms a hole inside the TSC phase which then accommodates gapless modes at that interface. If the vortex threads a flux of $h/2e$, a zero energy state is trapped within the vortex core. Such a Majorana zero mode (MZM) bound at the vortex core is of great interest as its potential to be used

as a qubit for the purpose of Fault tolerant quantum computation. Since the MZMs are bound at the vortex cores as long as the vortices are sufficiently far away from each other the corresponding quantum state is protected as long as hybridization of the MZMs are not allowed. Thus the localized MZMs provide a degenerate manifold on which computation can be performed by braiding the vortices around one another adiabatically without destroying the coherence of the quantum state.

Thus, 3D strong TIs provide a great platform by providing a robust helical surface dispersion on which superconductivity can be induced.

2.1.3 The strong TI phase in FTS

In the Fe-based chalcogenide compound, $FeTe_{1-x}Se_x$ (FTS), the chalcogen atoms can be treated equivalently. The structure of material in 3D can be thought of mono layers of FTS stacked on top of each other with the layers weakly coupled. The weak inter layer coupling manifests itself as the negligible dispersion along the out-of-plane direction compared to the in-plane momentum directions of the electronic bands. The material is time-reversal symmetric and even though it has Fermi pockets that contribute to superconductivity, there is a region in momentum space that has a topological band gap which produces protected helical surface states as we discuss here. Due to time-reversal symmetry (TRS) of the system the corresponding bulk topological phase can be classified by the $\mathbb{Z}_2$ invariants defined in earlier paragraph. In addition to TRS, FTS also possesses inversion symmetry and thus the $\mathbb{Z}_2$ invariants can be expressed as a product of the parity eigen values of half of the two-fold degenerate

occupied bands as in Eq. 2.5.

2.1.4 Band inversion in FTS

To understand the non-trivial $\mathbb{Z}_2$ invariant, let us focus on the ΓZ band dispersion which is schematically shown in Fig. 2.1. The dotted bands refer to the case when there is no spin-orbit coupling (SOC). The two bands have opposite parity characteristics, i.e., at the TRIMs the parity eigen values associated with those bands are opposite to each other. Specifically, the parity for the states of the band, that appears as conduction band at the Γ point, is odd, we would call this p_z-type band which is due to its symmetry properties under rotation at the high symmetry points. On the other hand the band, that appears below at the Γ point, has even parity eigen values at the TRIMs, we call this $d_{xz/yz}$ band. As hinted by the dotted lines, without SOC these two bands cross each other along the ΓZ line. Once SOC hybridizes them, a gap opens up and if the Fermi level lies in the gap, the system becomes an insulator. Now for the conduction band the parity eigen values are even at the Γ point which reflects its $d_{xz/yz}$ character whereas the parity at Z point is odd due to its p_z character. Since at all other TRIMs the occupied bands have even parity (all d-type bands with different rotational symmetries), the odd parity at the Z point makes the $\mathbb{Z}_2$ invariant non-trivial according to Eq. 2.5.

As described above the inversion of parity at the Z point is reminiscent of the band crossing between the odd and even parity bands as shown by the dotted lines in Fig. 2.1. DFT based electronic structure provides insight in this band inversion

mechanism [21]. In FeSe the p-type band is has higher average energy and stay disconnected from the d-type valence band. As a result the occupied band manifold is d-type for FeSe which is classified as a topologically trivial phase associated with $\nu_{0,1,2,3} = 0$. With Te doping the p-type band is shifted downwards approaching the d-type valence band [21]. At enough Te concentration they eventually intersect as shown in Fig. 2.1 and SOC opens up the required gap to have an insulating phase. It turns out that the p-type band in FTS is much more dispersive compared to the d-type band from the DFT based band structure. Thus, the relative composition of the Te/Se atoms appears to be key in determining the topological character in FTS. Keeping in mind the role of Te composition in determining the topological character it is thus important to understand the topological - trivial phase transition as a function of x in $FeTe_{1-x}Se_x$ for experimental purposes. In most of the experiments the sample corresponds to $x = .45$. This is because the superconducting transition temperature T_c is the highest ($T_c \approx 14.5K$) at this composition under ambient pressure. However, in a recent experiment carried out in the Brookhaven lab [1], a large sample of about 1mm $\times$ 1mm area where the relative Te/Se composition varied naturally due to inhomogeneity associated with the alloy nature of the material, a close investigation of the topological surface states (TSS) associated with the strong TI phase revealed a phase boundary between the trivial and topological phases. The composition at various spots of the sample was measured locally by electron diffraction spectroscopy (EDS) and the composition was correlated with the presence/absence of the TSS associated with the topological and trivial phases. The experiment revealed that the phase boundary lies precariously close to the typical sample that is used with $x = .45$.

2.1.5 Topological domain disordered phase

The scenario near the phase boundary becomes interesting while taking into account the Te/Se density inhomogeneity in the sample. The inhomogeneity in the Te/Se composition is seen in STM topographs of the sample surface [22]. Since $x = .45$ is very close to the topological-trivial phase boundary, this inhomogeneity can give rise to regions of the sample where the Te/Se composition can be associated with topologically trivial composition for a bulk sample. In fact the experiment by the Brookhaven lab [1] directly supports this fact where the composition (averaged over blocks of $1\mu m \times 1\mu m$ area) varied considerably in a large sample. The STM topograph in a rather smaller field of view shows composition fluctuations in a much smaller scale of about $\sim$ 3nm. Such inhomogeneity might locally drive the sample out of the topological phase and the resultant trivial patches would be scattered across all regions of the sample giving rise to a disordered phase - we call such a phase the topological disordered phase since the disorder effectively alters the topological invariant, more precisely the topological gap/mass term in a disordered manner.

One can imagine the implications of such a topological disordered phase while considering its effect on the surface states. Let us consider a scenario where some regions on the sample-surface are trivial creating domain boundaries with topological regions. For simplicity let us consider that the layer below the surface is topological as expected if the composition were homogeneous. In that case as opposed to the clean case the surface states would also be inhomogeneously distributed on the sample surface - specifically they would be repelled by the trivial patches. The trivial patches

would be avoided by the surface states and in those regions they would tunnel below the top layer into the next layer. From the topological phase perspective the trivial regions would effectively simulate the vacuum in this case. This inhomogeneity in the topological surface state density would be a key signature in a topological disordered phase. Thus, motivated by the possibility of such a disordered phase in the alloy, FTS, we investigate the resultant TSS signatures in this chapter.

To simulate the topological disordered phase in FTS we start by constructing an effective model of the strong TI phase for a clean sample. We then introduce a disorder potential to spatially vary one of the model parameters, that controls the band inversion in the electronic structure, which effectively simulates the local domains of trivial regions in the topological sample.

2.2 Construction of the effective model Hamiltonian

Here we construct an effective model for the strong TI phase in FTS. As explained earlier the band inversion in this material occurs due to hybridization between a d-type and a p-type band along the ΓZ. Thus, the relevant manifold includes the $d_{xz/yz}$ bands which have orbital angular momentum $l_z = \pm 1$ and the p_z band with orbital angular momentum $l_z = 0$. Combining the spin degree of freedom the $d_{xz/yz}$ bands form a manifold with total angular momentum $j = l + s, l - s = 3/2, 1/2$. The spin-orbit coupling thus split the $l_z = \pm 1$ manifold into two separate angular momentum sectors $j_z = \pm 3/2, \pm 1/2$. On the other hand the p_z band along with spin composes another manifold of $j_z = \pm 1/2$. The band crossing happens between the two sectors of same

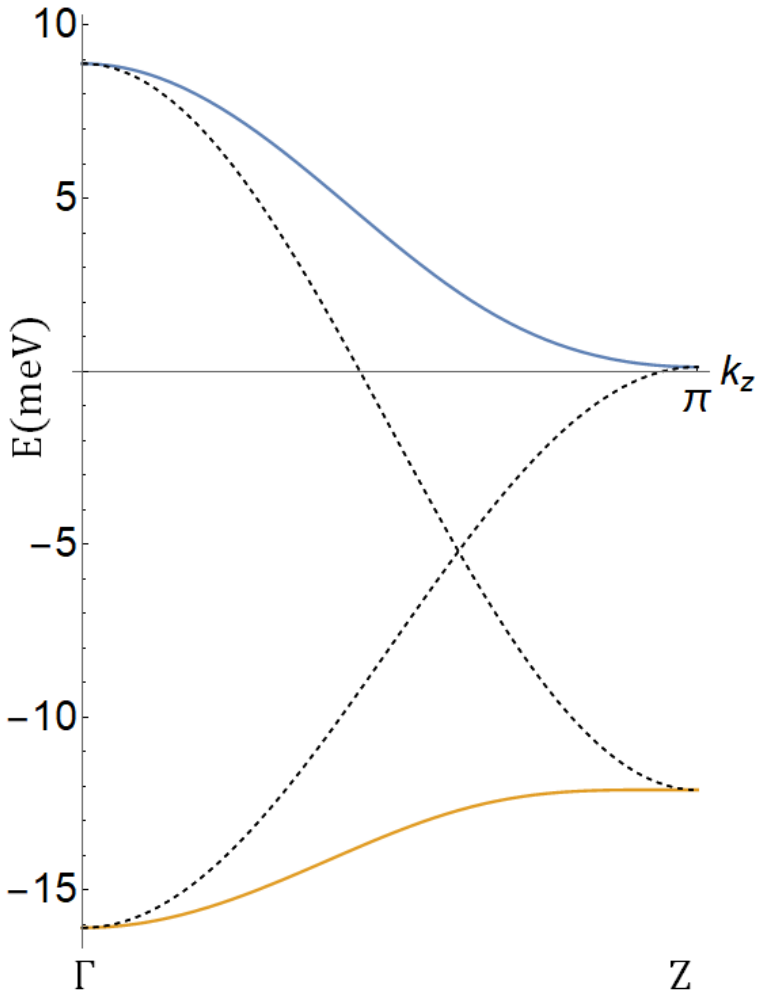

Figure 2.1: ΓZ band dispersion from our model $\hat{H}_{\mathrm{I}}$, for the parameter values described in the text, without SOC (dashed curve), i.e. $t' = 0$ in our model, and with SOC (solid curve) are shown. Crossing between d-type and p-type bands happens for $|\delta_{\parallel}| < |\delta_z|$ (dashed). Hybridization between them via SOC opens up a gap (solid).

angular momentum, $j_z = \pm 1/2$ - the d-type band being even under parity whereas the p-band is odd at the TRIMs. The SOC between the two $j_z = \pm 1/2$ manifolds form d-type and p-type bands gives rise to an insulating gap. The $j_z = \pm 3/2$ bands of $d_{xz/yz}$ lie above the Fermi level and possibly intersects with the largely dispersive p_z

band. Since those two manifolds are in different angular momentum space, SOC do not hybridize them. For our effective model however, we ignore the $j_z = \pm 3/2$ manifold as they do not take part in the topological band inversion that we are interested in. We represent the $j_z = \pm 1/2$ sector by the Pauli matrices $\sigma^{x,y,z}$. And we label the parity sectors by another set of Pauli matrices denoted by $\rho^{x,y,z}$. The even (d-type) and odd (p-type) parity bands are labelled by $\rho_z = +1$ and $\rho_z = -1$ respectively. In more rigorous group theoretic notation $\rho_z = \pm 1$ represents the $\Gamma_6^{\pm}$ representation at the Γ and Z points in DFT band structure [21]. In this basis described above we build a model similar to the Bernevig-Hughes-Zhang (BHZ) model that incorporates the band inversion [23] as elaborated below.

Our model for FTS respects inversion symmetry and TRS. The inversion symmetry is described by the operator ρ^z in the Hilbert space described above. The anti-unitary time reversal symmetry (TRS) is described by the operator $i\sigma^y K$ where K is the complex conjugation operator. Additionally at long wave lengths the system possesses C_4 rotational symmetry around the z-axis. Given the representation of the angular momentum sector by $\sigma_z = \pm 1$ and accordingly $\sigma^z = 2j^z$, the C_4 operator can be represented by $C_4 = e^{i\pi j^z/2} = e^{i\pi\sigma^z/4}$.

We focus on the small in-plane momenta ($k_x, k_y \approx 0$) since the band inversion happens at $k_x, k_y = 0, 0$. We introduce nearest neighbor hoping along z-direction between adjacent layers. In that limit the Hamiltonian takes the form

$$\hat{H}_{\mathrm{I}}(k_{\parallel} \approx 0, k_z) = \left[\delta_{\parallel} + \delta_z \cos k_z - \frac{A}{2}\left(k_x^2 + k_y^2\right)\right] \sigma^0 \rho^z + t' \sin k_z \, \sigma^z \rho^x. \tag{2.6}$$

where $\rho_z = \pm 1$ correspond to even and odd parity sectors and $\sigma_z = \pm 1$ correspond

to the two angular momentum sectors of $j_z = \pm 1/2$ as described above. Here the parameters $\delta_{\parallel,z}$ determine the energy differences between the p-type and d-type band states at the Γ and Z point. The gap between the d-type and p-type band states at the Γ point is given by $\delta_\parallel + \delta_z$ whereas the same gap at the Z point is $\delta_\parallel - \delta_z$. Thus, if $|\delta_z| > |\delta_\parallel|$, the gap changes sign as it goes from Γ to Z. This sign flip results in the valence band state shifting from $\rho_z = +1$ sector to $\rho_z = -1$ sector at Z. Thus, the band inversion criteria for our model is $|\delta_z| > |\delta_\parallel|$ which facilitates the two bands to cross somewhere along the ΓZ line as shown in Fig. 2.1. The second term in $\hat{H}_\mathrm{I}$ is an SOC term that hybridizes the d-type and p-type bands via hoping across adjacent layers of FTS and opens up a gap along ΓZ [Fig. 2.1]. The band structure plotted in the Fig. 2.1 is for $\delta_z = -9.3\,\mathrm{meV}$, $\delta_\parallel = -3\,\mathrm{meV}$ and $t' = 7.5\,\mathrm{meV}$. The parameter A in the first term of $\hat{H}_\mathrm{I}(k_\parallel \approx 0, k_z)$ determines the curvature of the parabolic dispersion for small in-plane momenta ($k_\parallel \approx 0$) around the Γ point.

We note that since FTS is a superconducting material it has bands crossing the Fermi level. In fact there are two hole-like Fermi pockets around Γ and two electron-like pockets around M point. Thus, FTS is a metal. However, the Fermi sheets for the 3D system is approximately cylindrical owing to the layered nature of the FTS with little dispersion along the z-direction and the topological surface states reside in a region of momentum space that do not overlap with the Fermi pockets. Thus, there exists a clear window in energy and momentum space where the TSS are decoupled from the bulk metallic states which preserves them and the Dirac cone associated with the Helical TSS can be observed in ARPES measurements. Furthermore, the spin texture of the dispersion has also been seen in spin - selective ARPES experiments [24, 6]. The

bottom line is that the strong TI phase and the corresponding TSS remain intact in the system even in the presence of metallic Fermi sheets.

In the topological regime of the Hamiltonian described by Eq. 2.6 (i.e., $|\delta_z|/|\delta_\parallel| > 1$) the (001) surface hosts gapless helical modes with in-plane Dirac dispersion. The corresponding velocity for the Dirac dispersion near the Γ point is determined by another in-plane SOC term. Such an SOC term has the form

$$\hat{H}_{\rm SOC} = \alpha \left(k_x \, \sigma^x + k_y \, \sigma^y\right) \, \rho^x \tag{2.7}$$

Finally, we note that the ΓZ dispersion for FTS is far from particle-hole symmetric. To simulate this particle-hole asymmetry we include a term that breaks that symmetry of the band energies. Such a term would be simply identity in the parity and spin basis and is given by,

$$\hat{H}_{\rm eh} = \delta_2 \, \cos k_z \, \sigma^0 \, \rho^0 \tag{2.8}$$

The three terms together gives rise to the desired effective model for our purpose:

$$\hat{H} = \hat{H}_{\rm I} + \hat{H}_{\rm SOC} + \hat{H}_{\rm eh} \tag{2.9}$$

We use this model and explicitly obtain the surface states spectra by numerically solving the eigen values problem with a finite size sample along z-direction. The characteristics of the surface states are determined by the model parameters which we tune to match our results with the ARPES data as we describe in the next section.

2.3 The numerical results

2.3.1 Ideal surface spectra

To calculate the surface states with the model Hamiltonian Eq. 2.9 we need to discretize our model along z-direction. For that purpose, $\cos k_z$ is replaced by $|z\rangle\langle z + c| + |z + c\rangle\langle z|$ and $\sin k_z$ is replaced by $i(|z\rangle\langle z + c| - |z + c\rangle\langle z|)$. Here z is the real-space coordinate representing planes stacked in the z direction and c is the unit cell length along that direction. Using the resulting discretized Hamiltonian we simulate the surface states for each (k_x, k_y) around the Γ point numerically.

To obtain an effective Hamiltonian one needs to adjust the parameters so that the key features of the band structure as has been observed in ARPES measurements match with the simulated features from the model. We recognize the following three key features to be important part of our simulated band structure which are:

(i) the band width of the valence band along the ΓZ direction in Fig. 2.1 (about 4 meV [25])

and for the topological surface states

(ii) the energy gap between the Dirac point and the top of the bulk valence band (~ 10 meV) [25]

and

(iii) the Dirac velocity for the surface states dispersion (~ 370 meV-Å) [25, 24].

To tune the band width the three $\delta_{\|}, \delta_z, \delta_2$ parameters can be varies whereas the dispersion of the surface states are determined mostly by A and α.

After parameter tuning the resultant model produces the surface dispersion and

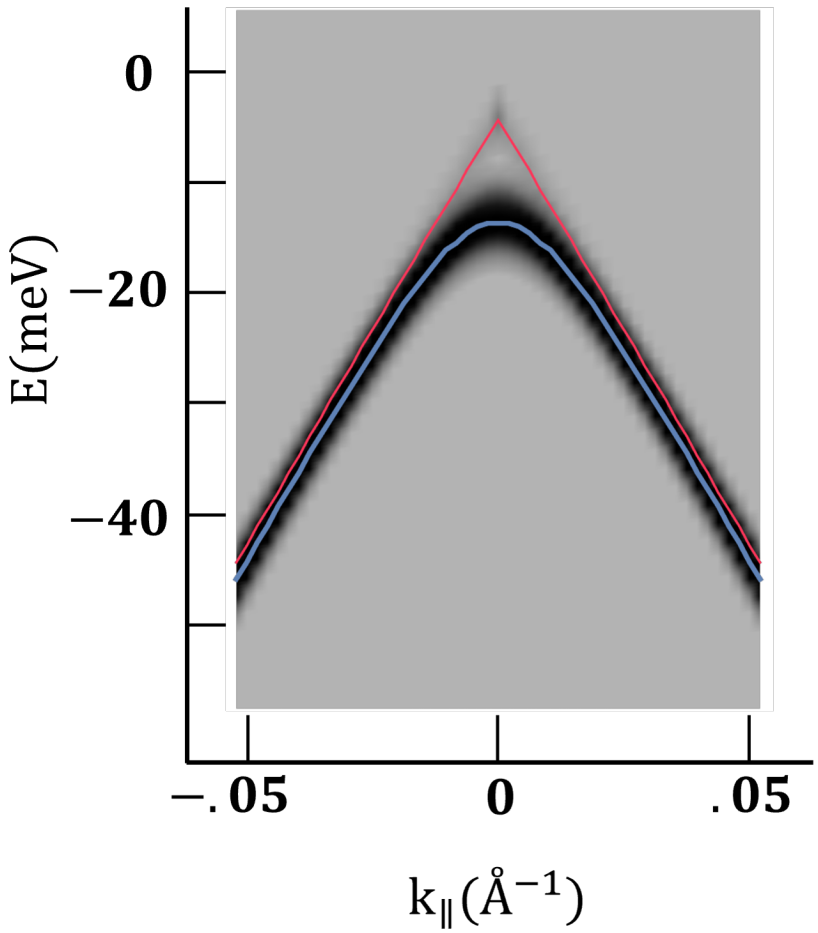

Figure 2.2: Surface-weighted parabolic bulk dispersion and the Dirac dispersion for the surface states along with their energy dispersion curves (EDC) shown in blue and red respectively as obtained from our model with the parameters specified in the text.

the bulk bands near the Γ point that are shown in Fig. 2.2. The energy dispersion curve (EDC) for the broad parabolic bulk band has been shown by the blue line and that of the Dirac dispersion by the red line. The parameters in Eqs. 2.6 - 2.8 are tuned to be $\delta_z = -9.3\,\text{meV}$, $\delta_{\|} = -3\,\text{meV}$, $t' = 7.5\,\text{meV}$, $\delta_2 = 1.2$, meV, $A = 798\,\text{meV-Å}^2$, and $\alpha = 266\,\text{meV-Å}$ such that the relevant quantities from the simulated dispersion match the estimates from the ARPES measurements in [25, 24] as mentioned above.

So now we have an effective model for the surface states described by the Hamiltonian

Eq. 2.9 and also a set of parameters that reasonably features the experimentally measured properties of the TSS. We also described how the relative magnitudes of $|\delta_z|$ and $\delta_\parallel$ controls the strong TI phase in our model. Now we proceed to spatially vary the $|\delta_\parallel|$ parameter to simulate a phase where patches of the sample becomes topologically trivial as described in the topological disorder section.

2.3.2 The topological domain disorder

To simulate a topological domain disordered phase we incorporate a disorder potential in the definition of spatially varying $\delta_\parallel$ parameter. As discussed in the introduction, such a phase can arise from local fluctuations in the Te/Se concentration, i.e., fluctuations in x in $FeTe_{1-x}Se_x$. We model these fluctuations by allowing the parameter $\delta_\parallel$ in the Hamiltonian (Eq. 2.6) to continuously vary in real space (x-y-z). We add a disorder potential $w(x, y, z)$ to $\delta_\parallel$ as $\delta_\parallel(x, y, z) = \delta_\parallel + w(x, y, z)$. $w(x, y, z)$ is random with a Gaussian correlation of a specific length scale which we will denote by λ.

Motivated by the layered structure of FTS, we assume that $w(x, y, z)$ is uncorrelated between the neighboring layers, but smooth in the x-y plane at each layer. For the purpose of conceptual and computational simplicity, we start our analysis by assuming that $w(x, y, z)$ varies along the x and z direction but is uniform along the y-direction, i.e., $w(x, y, z) = w_{1D}(x, z)$. As mentioned earlier, we assume that the disorder fluctuations are uncorrelated between different layers along z. The correlation along the in-plane direction can be estimated from the length-scale associated with

Te/Se density fluctuations as observed in STM topography [22, 26].

The Gaussian disorder potential $w_{1D}(x)$ can be modeled by choosing its momentum space components randomly with a momentum dependent Gaussian weight. The momentum-space function has the following form:

$$w_{1\mathrm{D}}(k_x, z) = \frac{\sigma_w}{\sqrt{2}} \exp\left[-\frac{(k_x\lambda)^2}{2}\right] \left[X_{k_x} + i\, Y_{k_x}\right]. \tag{2.10}$$

In the above, X_{k_x} and Y_{k_x} are two normal $[N(0,1)]$ random variables identical and independently chosen for each value of k_x. σ_w is the disorder strength and λ is the characteristic length scale of the disorder potential. We estimate σ_w from the broadening of the ARPES observed band structure which is about $\sim$ 3meV. The typical length scale of Te/Se density variation is chosen to be about $\sim 3\,\mathrm{nm}$ as estimated from STM topographic images from the experiments [22].

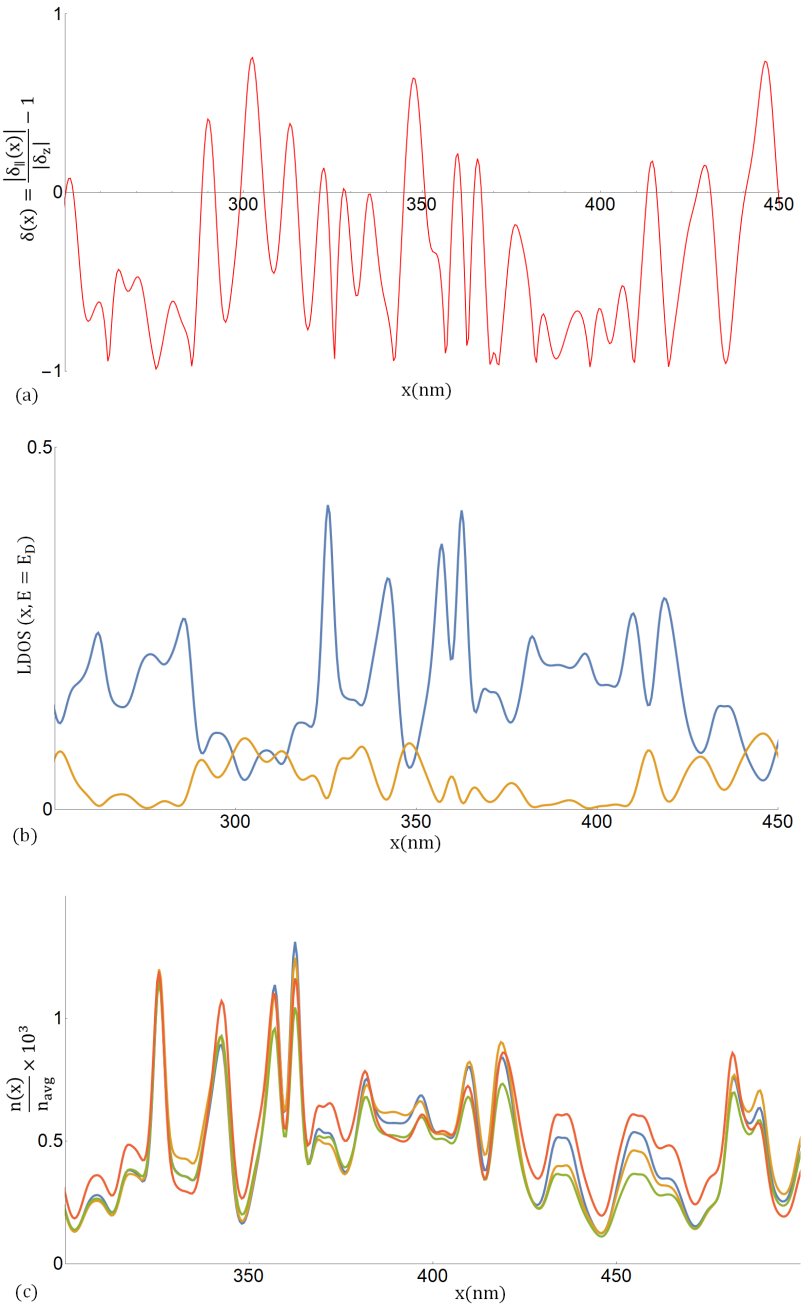

Figure 2.3: (a) $|\delta_{\parallel}(x)|/|\delta_z| - 1$ plotted as the red curve where the black lines show some of the topological ($\delta(x) < 0$) and trivial ($\delta(x) > 0$) phase boundaries. (b) Top layer (blue) and second layer (yellow) LDOS for the topological domain disorder. (c) Normalized top layer LDOS at different energies within the Dirac dispersion window collapse on each other.

After introducing the variation for $\delta_{\parallel}$ along the x-direction, the periodicity of the model is compromised. Hence, we need to replace k_x in Eq. 2.6 by $-i\partial_x$ where ∂_x should be interpreted as the discretized derivative with an in-plane lattice parameter a.

To gain an insight about the effect of topological disorder we introduce the disordered mass $\delta_{\parallel}(x)$ only on the top layer of a finite size sample. To capture the behavior of the TSS when the disorder is on the top layer, we plot the local density of states for the top layer and the layer beneath as we anticipate the TSS density avoids the trivial regions on the top layer and instead accumulates at the layer below. As we will see that as a result the suppression of TSS on the top layer is correlated with the enhancement at the layer beneath. The resultant variation in the surface state density is shown in Fig. 2.3. In three panels of Fig. 2.3

(a) local topological invariant as a result of particular disorder realization,

(b) the local density of states for the TSS associated with that realization for the top and the next layer

and

(c) the scaling of the top layer density variation for different values of energy within the Dirac dispersion window

are shown from simulating the topological domain disorder phase along x only on the top layer of the sample.

Fig. 2.3(a) shows the variation of $\delta_{\parallel}(x)$ from a particular realization of Eq. 2.10 on the top layer, i.e., $z = 0$. As discussed in Sec. 2.2, regions with $|\delta_{\parallel}(x)| < |\delta_z|$ are in a nominally trivial phase, while the rest of the region is in the topological phase. To help

identify trivial regions, Fig. 2.3(a) plots $\delta(x) = |\delta_{\|}(x)/\delta_z| - 1$, so that trivial domains are associated with the regions with $\delta(x) > 0$. Since topological phase is strictly a global property, this local attribution of trivial and topological regions works only as a crude guide to understanding the numerical results that follow rather than a strict identification of the phase.

The LDOS associated with this disorder realization is plotted for the top (i.e. $z = 0$) and the second layer (i.e. $z = c$) of the system in Fig. 2.3(b). We notice that, as anticipated, the top layer LDOS is suppressed whereas the second layer LDOS is enhanced at the nominally trivial regions (i.e., where $\delta(x) > 0$). The same observation holds for the entire energy window of the Dirac dispersion. In fact, when the top layer LDOS is normalized by the total DOS at a specific energy the resultant quantity at different energies collapse on each other as shown in Fig. 2.3(c). This is expected since the TSS for most of the Dirac energy window would avoid the trivial regions suggests. The almost perfect collapse of the scaled LDOS throughout the sample strongly substantiates that intuition and this energy scaling would be unique for topological domain disorder as we will see shortly. The transfer of LDOS between the layers would be difficult to measure in STS since it can only probe the top layer. However, a closer examination of Fig. 2.3(b) shows that the trivial regions represented by LDOS enhancement in the second layer occur in the vicinity of large LDOS peaks in the top layer near the topological-trivial boundaries. Such peaks that demarcate the trivial domains persist across the entire Dirac energy window may be visible in STS. Furthermore, the signatures of the energy scaling that discussed above should also be visible when the density is measured for a range of energy window.

An obvious signature of a trivial patch on the surface of a strong topological insulator would be the reduced local density of states seen in Fig. 2.3(b). However, as also apparent from this plot, dips in local density of states are also seen in areas of strong fluctuations of $\delta(x)$, which are otherwise topological. This is consistent with the fact that disorder-induced Fermi energy fluctuations on the surface can lead to the Dirac point crossing the local Fermi level. The local density of states can be suppressed in such scenarios since the density of states of the Dirac dispersion in two dimensions vanishes at the Dirac point.

In the next section we compare the effects of the chemical potential disorder and distinguish from the signatures of the topological domain disordered phase described above. Since the Te/Se fluctuations would inevitably give rise to fluctuations in the chemical potential as well, comparison to that is key in order to observe the topological disorder signatures in an STS experiments.

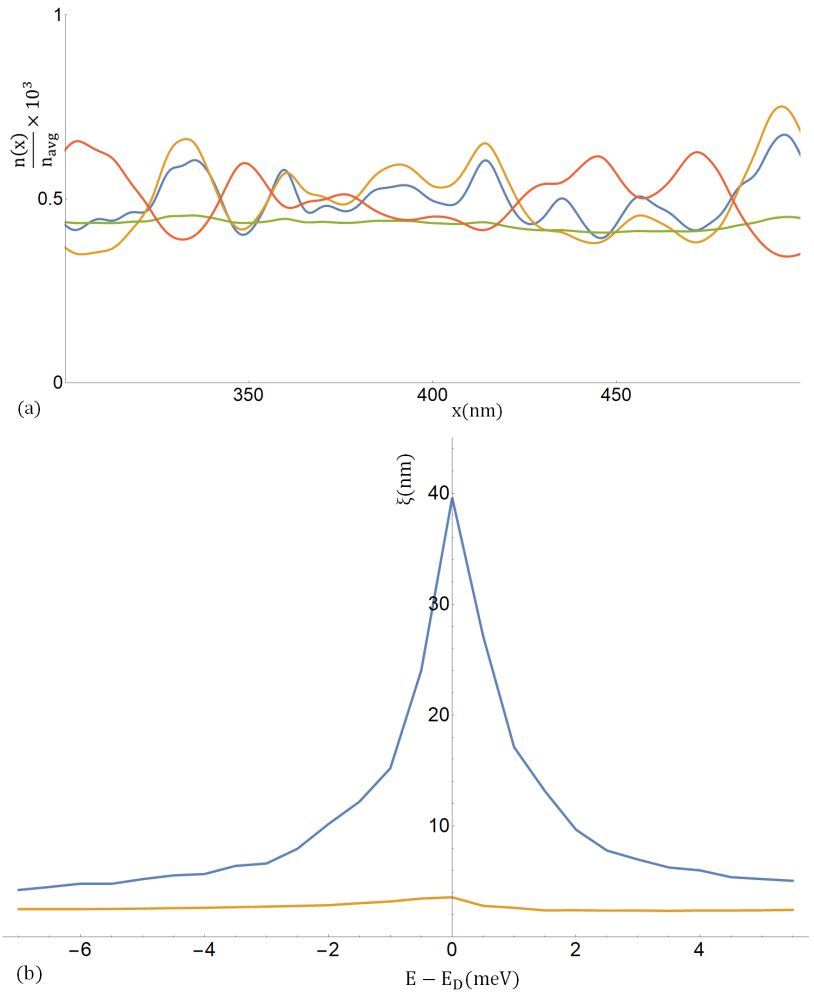

Figure 2.4: (a) Normalized LDOS at different energies for the chemical potential disorder. (b) Comparison of energy dependence of LDOS-LDOS correlation length between the topological domain disorder (orange) and the chemical potential disorder (blue) cases

2.3.3 Topological domain disorder vs chemical potential disorder

As the next step of our numerical calculation we investigate the effects of chemical potential disorder on the LDOS of the TSS.

Disorder in chemical potential can be simply modeled by a spatially varying function that is proportional to the identity matrix in parity and spin basis. Such a term would have the form as $w(x)\rho^0\sigma^0$ where $w(x)$ can be chosen to be a random potential in a similar fashion as before with the same length scale associated with the Te/Se density fluctuations. Since the disorder in general broadens the bands, one way to estimate the strength of the disorder could be to look at the ARPES measured band structure. For example in a typical ARPES data the Dirac point in the TSS dispersion appears to be broadened by about $\sim$ 2meV [25, 24]). As before we put the chemical potential disorder only on the top layer and study its impact on the LDOS of the top layer TSS.

From the similar plot of top layer normalized LDOS (Fig. 2.4(a)) the most obvious distinction w.r.t. the topological domain disorder case is that the scaled LDOS at the different energies do not appear to be correlated. To quantitatively establish this anticipation we compute the spatial correlation length associated with the variation of the TSS LDOS for both the cases of i) topological domain disordered phase and ii) chemical potential disordered phase. In the topological disordered phase since the scaled LDOS collapse for different values of energy, it is expected that the length scale for LDOS variation would be more or less constant as a function of energy. On the other hand the same length scale may vary for the case of chemical potential disordered phase.

The correlation length for the LDOS variation can be estimated from the Fourier transform of the real space density as the inverse of its spread in the momentum space, $\xi \approx 1/\sqrt{(\Delta k_x)^2}$. This quantity when plotted as a function of energy in Fig.

2.4(b) shows stark difference between the cases of chemical potential disorder and the topological domain disorder.

For the case of chemical potential disorder ξ decays with increase in energy w.r.t. the Dirac point. In particular, a variation of $\xi(E)$ as $\xi \propto 1/(E - E_D)$ where E_D is the energy of the Dirac point would fit the curve reasonably well. In contrast, ξ is effectively constant for the case of topological disorder. This conclusion is consistent with the collapse of the various LDOS peaks seen in Fig. 2.3(c), which shows that the widths of scaled LDOS peaks at the edge of trivial regions are independent of energy. This can be understood intuitively as the peaks being associated with tunneling into domain walls, whose widths are controlled by spatial variation of the disorder parameter $\delta(x)$.

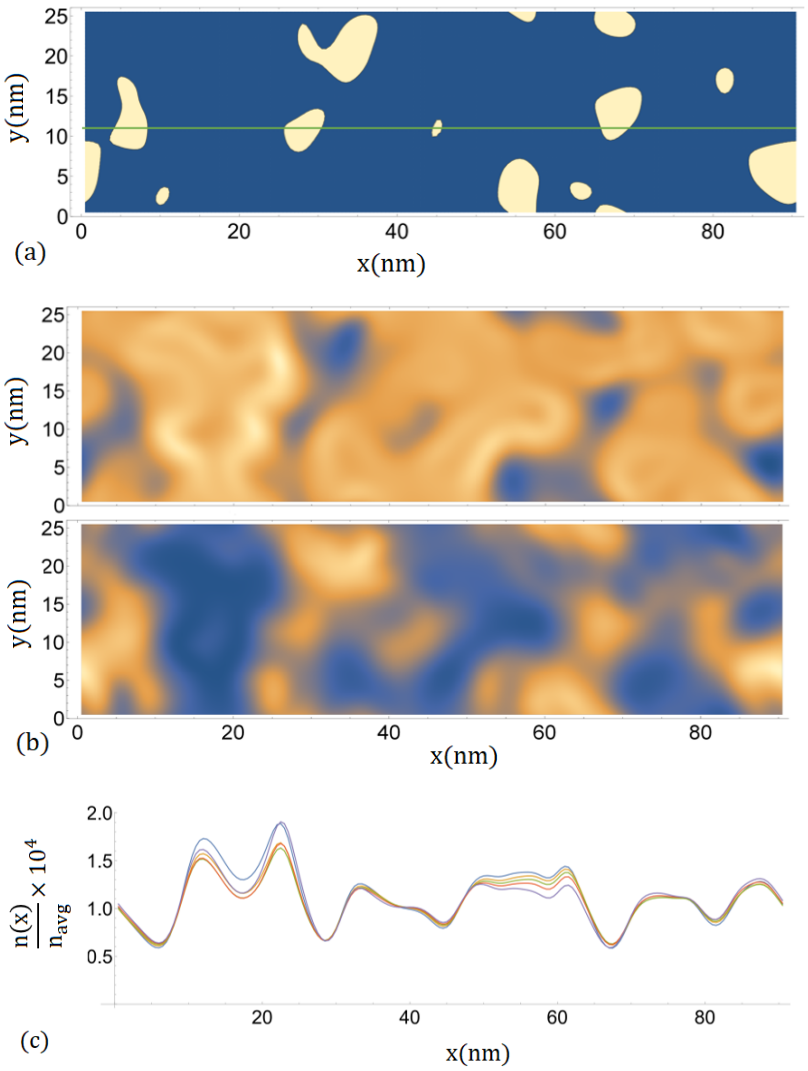

Figure 2.5: (a) Trivial islands shown as white patches whereas dark blue region is topological, (b) top layer 2D LDOS and next layer 2D LDOS shown in colour map in the upper and lower panel respectively where the density gradient goes high to low from yellow to dark blue. (c) Normalized top layer LDOS plot at five different energy values along the green line marked in (a)

2.3.4 Extending to 2D disorder potential

So far we have only modeled disorder that varies effectively along one spatial dimension where we kept the other in-plane direction periodic. This would be associated with stripe like disorder potential. Even though the same calculation provides key insights that distinguishes the cases of topological and chemical potential disorder, it is not particularly realistic.

Hence, we generalize our numerical calculation to incorporate a more realistic scenario when the disorder potential varies along both the directions in the plane. The 2D disorder potential can be similarly modeled in the momentum space for $w_{2D}(k_x, k_y, z)$ with the exception that the Gaussian weight given by Eq. 2.10 would depend on the magnitude of the 2D momentum vector, $k_{\parallel} = \sqrt{k_x^2 + k_y^2}$. In addition the Hamiltonian has to be discretized along both the x- and y- directions. With that included in the resultant 3D finite size model we can obtain the desired TSS LDOS for the 2D layers.

We present the results in Fig. 2.5. The trivial islands in Fig. 2.5 (a) are shown as light colored patches and are finite in size along all directions. The 2D LDOS is plotted using color plot in Fig.2.5 (b) for the top layer and the next layer in the upper panel and lower panel respectively. Similar to the 1D disorder case it can be noted that at the trivial regions the top layer LDOS is suppressed whereas the next layer LDOS is enhanced with high peak-like density surrounding the trivial regions on the top layer associated to the topological- trivial domain boundary. More importantly, the energy collapse feature of the LDOS at different energies (as shown for a section of the sample on the top layer in Fig. 2.5(c)) is also present in the 2D disordered case.

Thus, in summary the trivial regions on the top layer that may arise due to Te/Se composition fluctuations repel the TSS shifting them to the layer beneath which results in peak like enhanced density on the top layer associated with the topological-trivial boundary. The energy invariance of the scaled LDOS is another key feature in the topological disordered phase which is completely distinct when compared to the usual chemical disordered phase.

2.4 Summary and Conclusion

In this work, we have studied the effect of alloy disorder (i.e. Te/Se composition fluctuations) on the topological surface state of FTS. In order to do this, we have introduced a variant of the BHZ model [23] for the strong TI phase that is appropriate to a layered system such as FTS where the bandwidth from out-of-plane tunneling is much smaller than the in-plane bandwidths. Similar to the BHZ model, the topological properties such as the surface state dispersion and the near-gap bulk band structure can be characterized with a few phenomenologically determined parameters. We have fit our model to ARPES [25, 24] and been able to reproduce the qualitative structure of the surface ARPES dispersion. The BHZ model, which is based on a small wave-vector approximation, is not appropriate to FTS because of the narrow band width in the out of plane direction. Our phenomenological model can be combined with input from DFT calculations [21] to model the effect of Te composition fluctuations as a shift of the odd parity p_z band. As a side note, our phenomenological approach to model topological invariant fluctuations can be modified for the 2D FTS system which

also possesses non-trivial topological properties as a function of x [27]. We find that fluctuations in the position of the odd parity band can drive local fluctuations in the topological invariant, which in turn can lead to the disappearance of the surface state in parts of the surface for the 3D sample. More generally the fluctuations in topological invariant can also be driven by the change of the inter layer hopping term, denoted by δ_z in our model as the invariant is determined by the ratio of the onsite potential difference, $\delta_\parallel$, and inter layer hopping amplitude, δ_z, denoted by $\delta(x) = |\delta_\parallel(x)/\delta_z|$. Since the inter layer hopping amplitude is mediated by the atomic orbitals from the next-to-top layer, the composition of Se/Te only on the top most layer may not correlate to the local topological property on the surface of the sample. The disappearance of the surface state at the trivial domains is marked by a reduced local density of states on the top surface in these areas, which are bounded by domain-walls of peaks in the LDOS. One complication that we discuss is that the suppressed density of states in the non-topological domains may appear similar to topological areas where the Fermi-level crosses the Dirac point. We have shown that the effects of topological domain disorder can be distinguished from other forms of disorder by considering the energy dependence of the pattern of the fluctuation of density of states (also known as quasiparticle interference). Another relevant issue regarding the LDOS measurement of the surface states using STM is the presence of large M pockets near the in-plane BZ corner at the same energy as the Dirac cone. Hence, the states from the M pocket, in spite of them being from bulk bands, can contribute to the STM measured surface electronic density of states. However, states near M pocket carry large momentum and the corresponding density oscillates at the scale of in-plane lattice constant (≈ 0.4nm)

which is an order of magnitude smaller than the length scale of density fluctuations due to the proposed domain disorder ($\approx$ 3nm). Thus, averaging of the electronic density over a length scale which is in-between these two lengths should suppress the contribution from the states near M pocket. As a relevant point we note that the experimental evidence of a nearly V-shaped density of states around the Dirac point [28], which is the characteristics of a 2D Dirac dispersion, indicates that the long wave length surface state density is not affected by the states from any other non-topological bands.

As mentioned in the introduction, our motivation to study the effect of alloy disorder on the topological surface states was based on its potential effect on the vortex MBSs. As an example of how local fluctuations in the topological character of a system can affect MBSs, consider a scenario where in the SC state a vortex core penetrates through a trivial region on the top surface. Since the trivial region does not support topological states on the surface, such a vortex would not be expected to support any MBS. This would in principle be a potential explanation for the absence of MBSs in a large fraction of vortex cores in experiments [26, 29]. Furthermore, such a topological domain disordered phase might also help explain the absence of quantized conductance in a large set of vortices [30]. This would occur when the trivial region is small in size relative to the superconducting coherence length so that the MBS wave-function is still accessible to tunneling but at a reduced tunneling strength. Quantitative effect on MBS wave-function would depend on the actual correlation length for the alloy disorder and must be left to future work.

The alloy disorder that is natural in FTS can have other effects such as change in

band width of the odd parity band and the topological gap. In fact, the disappearance of the topological surface state in experiments [1] can in principle arise from a reduction or shift in the topological gap as opposed to a change in the topological invariant discussed in the manuscript. However, since DFT calculations or experimental data are not available to estimate these effects, it is difficult to estimate at present. Furthermore, correlation between the alloy disorder i.e. Te/Se positions may complicate the analysis of the disorder effects. However, one can hope that these effects together with iron impurity induced Zeeman field [31] as well as nematic fluctuations and strain effects can be included into the surface state model to develop a complete understanding of the evolution of vortex level spectra with magnetic field [26].

Chapter 3

Half unit cell shift defect induced sign-reversal of the induced superconductivity in Fe-based chalcogenide superconductors

3.1 Introduction

In this chapter we would study the possibility of an exotic Josephson junction (JJ) at a crystalline domain wall (DW) associated with in-plane half-unit-cell-shift (HUCS) on the surface of FTS which is characterized by the SC gap differing by a phase of π across the defect. Such π-junction is of particular importance on the TSC phase since it captures helical Majorana modes at the defect [12]. In this chapter we discuss a mechanism that can give rise to such a π-junction. The results presented here is based on a manuscript, in preparation for publication [13].

The topological band inversion between an odd and even parity bands in FTS gives rise to a topologically non-trivial strong 3D TI phase which is characterized by helical Dirac surface states. In addition to the TI phase FTS also possesses an unconventional $s_{\pm}$ superconducting state which is characterized by the s-wave order parameter (OP) having opposite signs between the Γ and the M pockets. The Fermi surface in this material is well-separated in momentum space from the bulk TI gap owing to its almost cylindrical shape with same radius throughout its axis which allows the TI gap to reside within the Γ Fermi circle and doesn't mix them together.

Furthermore, this cylindrical Fermi sheet induces strong enough s-wave pairing on the topological surface states. A helical surface dispersion where the Fermi level encloses a single Dirac mono pole, along with s-wave superconductivity gives rise to a 2D superconductor which is topologically non-trivial in nature. Such a topological superconducting (TSC) phase can be characterized by a $\mathbb{Z}$ integer and a magnetic vortex passing through it by a $\mathbb{Z}_2$ integer. The vortices when in the topologically non-trivial phase captures a zero-energy particle-hole symmetric state known as Majorana bound state (MBS). The Majorana zero modes (MZMs) must occur in pairs. Hence, within a vortex that penetrates through a 3D material perpendicular to the TSC surface, the two MZMs appear at the two ends of the vortex. Each such MZM is exponentially localized which protects it from hybridizing with its partner MZM at the other end of the vortex. Such a hybridization is detrimental for the MBS and splits their energy to open up a gap in the spectrum. For the purpose of quantum computation one typically requires multiple such vortices on the surface that penetrates through the TSC phase, then each vortex is expected to host an MBS as long as the vortices are sufficiently far away from each other. As a result, one has a manifold of multiple zero energy states that create the degenerate ground state for quantum memory. The state of such degenerate manifold is protected from environmental local noise as long as the vortices do not interact with each other. A gate operation on such a manifold is achieved by non-abelian braiding a subset of vortices and during such process as long as the time scale associated with the operation is larger compared to the inverse of excitation gap of the system, the state remain in the ground state manifold by the adiabatic theorem [32, 33, 34]. The protection against local noise in the system is the

key advantage of the topological quantum computation scheme for which the Majorana zero modes are sought after entities to be use as qubits in quantum computation.

In addition to previously known platforms for vortex Majorana bound states VMBS [35, 36, 37] the recent discovery of the strong topological insulator (TI) phase in the iron-based superconductor, $FeTe_{1-x}Se_x$ (FTS) [4, 5] has attracted attention as a promising candidate due to the intrinsically induced s-wave pairing on its topological surface states. In addition to multiple promising results for realization of VMBS states in this material already [7, 8, 6, 9], further theoretical and experimental efforts for understanding certain detailed aspects of the MBS, such as conductance quantization of zero bias peaks (ZBP), inhomogeneity in ZBPs, etc., are ongoing. Apart from the Majorana zero modes (MZMs) localized at the vortex core, another characteristic feature of the TSC phase arises in the form of dispersing Majorana modes along a linear defect when the TSC gap flips sign across the defect [12].

Motivation: A mono layer of FTS consists of an Fe- square lattice along with the chalcogen atoms (Te and Se) which are located off the Fe-plane alternately above and below the plane. As shown in Fig. 3.2 the Fe atoms are marked with dark filled small circles and the chalcogen atoms are represented by the larger circles - among which the hollow circles are below the plane and the shaded circles are above the plane. The alternating above and below locations of the chalcogens in the lattice breaks the symmetry represented by translation along the nearest Fe-Fe bond that exists in the Fe-square lattice. Instead, such translation applied twice becomes the symmetry of the lattice. The operators that translate the Fe atoms by Fe-Fe nearest bonds thus becomes the half translation operators which are represented by $\hat{T}_{x,y}$ in Fig.

3.2. A shift of the lattice by $\hat{T}_x$ or $\hat{T}_y$ creates a crystalline domain wall (DW) which is referred to as the half-unit-cell-shift (HUCS) defect [22]. In a recent scanning tunneling spectroscopy (STS) measurement an exciting density of states (DOS) feature has been observed along such a DW on FTS surface. The DOS is characterised by the suppressed superconducting gap associated with the DOS flat as a function of energy. Such a DOS signature originates from a linearly dispersing modes in such 1D domain wall. In addition, such signatures are absent along same DWs in the non-topological samples in the FTS class, e.g., FeSe, which indicates that the DOS may have a topological regime.

An explanation for the DOS signature can be provided if the TSC gap changes sign across the DW in which case a linearly dispersing helical particle-hole modes known as the helical Majorana modes appear at the boundary of the sign-changing TSC gap [12]. Such a linearly dispersing helical Majorana modes has a flat DOS signature as seen in the STS experiment [22]. Thus, it is natural to ask about the origin of such a sign flip in the gap. Ref. [38] proposes that ferromagnetic order that is spontaneously formed along the DW can give rise to a π- phase shift in the order parameter (OP) for appropriate strength and width of the magnetized region. In this chapter we propose a different mechanism for the origin of π - phase shift across the DW which we briefly describe below. The TSC gap on the surface is induced by the bulk OP. Thus, if the bulk OP has a natural π-shift, it would also induce a π-junction on the surface as well. Hence, we propose a mechanism that would give rise to an exotic π-junction across the DW in the bulk OP that is thermodynamically more stable than the trivial junction with no phase shift.

Our mechanism is based on the $s_{\pm}$ pairing state in FTS. The OPs for both the Γ

and M pockets have s-wave symmetry, but the sign of the OP between the two pockets are opposite to each other. This sign flipping s-wave OP is called $s_{\pm}$ pairing state. Given such a pairing state if a linear defect such as the HUCS DW strongly couples the electronic modes between the two pockets, the OPs of the Γ and M pockets at the opposite sides of the DW get mixed via Andreev reflection. Since the two pockets on both sides of the DW have an intrinsic π phase shift, an additional π shift would effectively cancel the phase difference and this would imply that a π-junction would accommodate Andreev bound states (ABS) that have lesser energy for the occupied levels compared to the trivial junction with no phase shift as we elaborate in Sec. 3.2. Thus, the strong inter-pocket mixing in a background of $s_{\pm}$ pairing gives rise to the energetic stability of a π-junction across the half shifted DW. We numerically calculate the junction spectrum using an effective model of an FTS mono layer and show that indeed for a wide range of model parameters that reasonably simulate the Fermi pockets of the FTS band structure favors the π-junction over the 0-junction.

As hinted above since the surface TSC gap is induced by the bulk pairing of subsequent layers beneath the surface, a π-shift in TSC gap would occur when the shifted DW continue beneath the top surface up to few layers into the bulk. We note that the energy cost associated with such a defect is dominantly due to the lattice mismatch that span across the shifted area of the sample. If we consider the scenario where a few layers are half-shifted across the DW, the number of lattice mismatches is a sum of the same on the shifted surface and the shifts along the DW interfaces. Clearly the number of inter layer mismatches on the surface area is proportional to the shifted area whereas the same at the DW interface is proportional to the interface length times

the number of layers. Thus, if only few layers are shifted as opposed to a single layer, the extra energy cost associated with it is statistically insignificant w.r.t. the cost due to the interface area. Thus, continuation of the half shifted DW up to multiple layers is effectively as likely as having just the top lyaer shifted. In that case where as small number of layers are shifted forming the DW, a HUCS induced π-junction for the bulk pairing would also induce a π-shift for the TSC gap on the surface. Hence, the mechanism we provide for the π-shift of the bulk OP would naturally translate to the π-shift in the TSC gap explaining the origin of helical Majorana modes along the DW which has signatures consistent with the STS observation of the DOS in Ref. [22].

The Fermi surface in FTS, as mentioned earlier, is cylindrical with little variation along the out-of-plane momentum direction. Thus, it is quite reasonable to approximate its superconducting Fermi pockets by considering a mono layer of FTS. In this chapter, hence, we focus the problem of the HUCS DW separating a mono layer of FTS into two halves and show that in a wide range of model parameters the π-junction is energetically more favorable than the 0-junction.

Outline of this chapter: In Sec. 3.2 we start by explaining the intuitive idea for the π-shift mechanism in a FTS mono layer. For this purpose we consider the the two limiting cases of scattering, viz.

i) Pure intra-pocket transmission: when the DW doesn't mix the Γ and M pockets at all during transmission,

and,

ii) Pure inter-pocket transmission: when an electron from Γ pocket incident on the DW transmits entirely as an M pocket electron and vice-versa.

For these two limiting cases one can analytically compare the energetic stability of the ABS between the 0-junction and the π-junction. Such an analysis shows that for pure inter-pocket transmission the π-junction accommodates ABS with lesser energy than the same for 0-junction. The conclusion is opposite for the case of pure intra-pocket transmission. Such an analysis indicates that the DW induced inter-pocket transmission is the key mechanism for the origin of π-junction. To substantiate this intuitive idea, we turn to numerical evaluation of the Bogoliubov-de-Gennes (BdG) spectrum. First building an effective model of an FTS mono layer and incorporating the half-shift defect in the model, we numerically solve the BdG spectrum with an $s_{\pm}$ pairing for the cases of 0-junction and π-junction. In parallel, we also numerically solve the scattering problem with the DW using the python based package KWANT to obtain the intra-pocket and inter-pocket scattering strengths. By correlating the inter- vs intra- pocket transmission and the ABS energy levels for the 0- and π-junctions we find that strong inter-pocket transmission amplitude is positively correlated to the energetic favorability of the π-junction.

For the purpose of modeling the FTS mono layer we choose the 3 Fe-3d orbitals, viz. $3d_{x^2y^2}$, $3d_{xz/yz}$ which are the dominant orbitals according to DFT based band structure calculations. The parameters in our effective Hamiltonian are chosen to reasonably simulate the size and shape of the Fermi pockets around the Γ and M points which can be estimated from the ARPES measurements. In addition, the relative Fermi energies between the Γ and M bands were also maintained.

In the next section we first lay out the intuitive explanation of the π-shift mechanism using schematic representation of the Γ and M pockets.

3.2 Qualitative origin of π-junction

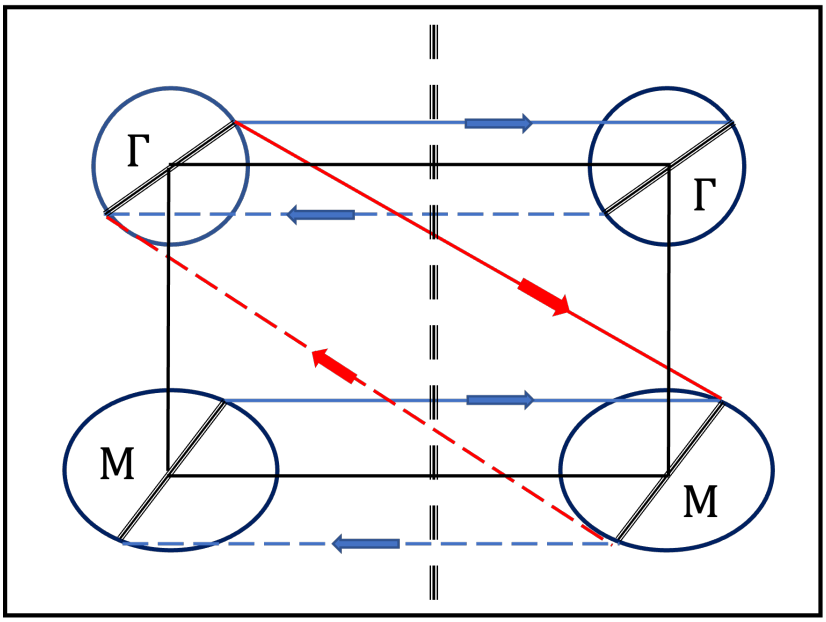

Figure 3.1: The schematic representation of the Andreev bound states (ABS) for the cases of (a) pure intra-pocket and (b) pure inter- pocket transmissions. The solid arrows correspond to electrons and dashed arrows to holes. For pure intra-pocket transmission (a) the ABS loop consists of electron and hole modes from same pocket (either Γ or M pocket). In contrast for pure inter-pocket transmission (b) electron and hole modes on both sides of the DW are entirely of the opposite pockets

Here we analyze the energetic stability between the π- and 0-junctions for the two extreme cases of scattering due to the DW, viz., i) pure intra-pocket transmission and ii) pure inter-pocket transmission. Such an analysis would help us to gain an understanding of the underlying mechanism for the π-shift.

We would assume that the SC gap is much smaller than the Fermi energy of the bands that form the Fermi pockets. This approximation validates our analytical

description of the ABS energy levels. In our numerical calculation (Sec. 3.4.2) this assumption is no longer a constraint. Analyzing the ABS energies in a setting of $s_{\pm}$ pairing we show that in case of pure inter-pocket transmission the energy of the occupied ABS levels is minimized when the overall phase-shift in OP is π across the DW, as opposed to 0-phase shift that is stabilized in case of intra-pocket transmission.

In the Fig. 3.1 we schematically show the loops that represent the ABSs. Since the SC regions on both sides of the DW are semi-infinite we assume that the electrons approaching at the NS interface perfectly Andreev reflects as their counter propagating time-reversed hole counterparts. An ABS can be thought of as an electron from the left incoming on the DW transmits through it and Andreev reflects from the SC gap on the right side as a hole which again transmits through the DW and Andreev reflects from the SC gap on the left to form a loop consisting of electron and hole modes. Such loops are shown in the Fig. 3.1 where the solid lines with arrow represent electrons and dotted lines represent holes. In that schematic representation the Γ pocket is shown by a circle and the M pocket by an elliptical shape on both sides of the defect which is represented by the vertical split line in the middle (Fig. 3.1). The blue loops represent the case of intra-pocket transmission whereas the red loops correspond to the inter-pocket transmission cases. As a result the blue loops connect same pockets on both sides of the defect whereas the red loop connects opposite pockets.

With that let us consider the case when there is pure- intra pocket transmission, i.e., the DW just lets through the electron and hole modes without scattering to any other pockets. For example, consider the case when a Γ electron is incident on the DW. The corresponding ABS loop is shown by the blue loop on the upper half of the

Fig. 3.1. Similarly for the case when an M pocket electron is incident on the DW, where the loop is the blue loop in the lower half of the Fig. 3.1.

In contrast, for the case of pure- inter pocket transmission, the DW completely flips the pocket of an incoming electron. In that case the ABS loop is shown in red in Fig. 3.1.

The key point determining the ABS energies is the phase difference of the SC gaps on both sides of the DW since during the Andreev reflections the electron and hole modes are connected by the phase of the SC gap. The ABS energy basically depends on the effective phase difference between the SC gaps on two sides that Andreev reflects an incoming electron to its hole counterpart. The phase differences between the two SC gaps from where the Andreev reflections happen is thus the key in determining the energy of the ABS levels in the two transmission limiting cases considered here. A clear distinction between the two scenarios is that the SC phase difference of the two sides is 0- and π for the cases of pure intra-pocket and pure inter-pocket transmission respectively.

In other words in the loop representation the twist in the phase throughout the loop determines the ABS energies as $|E_{\rm ABS} - \mu| \propto \sqrt{1 - |t|^2 \sin^2 \varphi/2}$. This formula is valid for a single channel transmission and φ is the effective SC phase difference in the OP and $|t|$ is the transmission amplitude. Thus, for a single channel $\varphi = 0$ would lower the energy of the ABS as opposed to the $\varphi = \pi$ case.

Now consider the case of pure intra-pocket transmission where the Γ (M) pocket electrons reflect off the SC gap from the same pocket. In that case there is no intrinsic phase difference between the two OPs on both sides of the DW. Hence, if there is no

additional phase difference put by the junction, the ABS energies will be minimized. Thus, in the case of pure intra-pocket transmission the 0-junction would accommodate lower energy ABS than that of the π-junction.

The key difference for pure inter-pocket transmission is that an electron incoming on to the DW switches pocket and reflects off the SC gap of the other pocket implying that the two Andreev reflections on both sides of the DW happen by the SC gaps of opposite pockets OP. Due to the intrinsic π phase difference between the s-wave OPs between the two pockets, such cross-pocket Andreev reflections would stabilize the π-junction compared to the 0-junction. The π-junction puts an additional π phase twist on the intrinsic π phase difference induced by the inter-pocket transmission. Thus, the total phase twist accumulates to 2π which is equivalent to no phase twist. In contrast, 0-junction in that case has π phase difference intrinsically which increases the ABS energies. Hence, DW induced pure inter-pocket transmission effectively couples OP of opposite sign s-wave gap in the $s_{\pm}$ pairing state which gives rise to an intrinsic phase difference of π and thus, the π-junction accommodates lesser energy ABS than the 0-junction.

This argument also indicates why $s_{\pm}$ pairing state is important for the mechanism of π-junction. If both the pockets around Γ and M points had s-wave OP of same sign, then even the inter-pocket transmission wouldn't give rise to any intrinsic phase difference like for the case of $s_{\pm}$ pairing. And hence, only the 0-junction would have been more stable.

We note that in the realistic case the DW induced transmission is neither pure intra-pocket nor pure inter-pocket, rather the transmission process is represented by a

2X2 transmission matrix for two pockets with off-diagonal elements corresponding to inter-pocket transmission and diagonal elements to intra-pocket transmission. To be consistent with the limiting cases, when the inter-pocket transmission is much larger than the intra-pocket transmission amplitudes, one can expect that the π junction would be more favorable and vice-versa. When we calculate the BdG Hamiltonian spectrum for the 0-junction and π-junction after we introduce an effective model for the FTS mono layer Fermi pockets, we can compare the junction stability to the relative inter-pocket transmission strength.

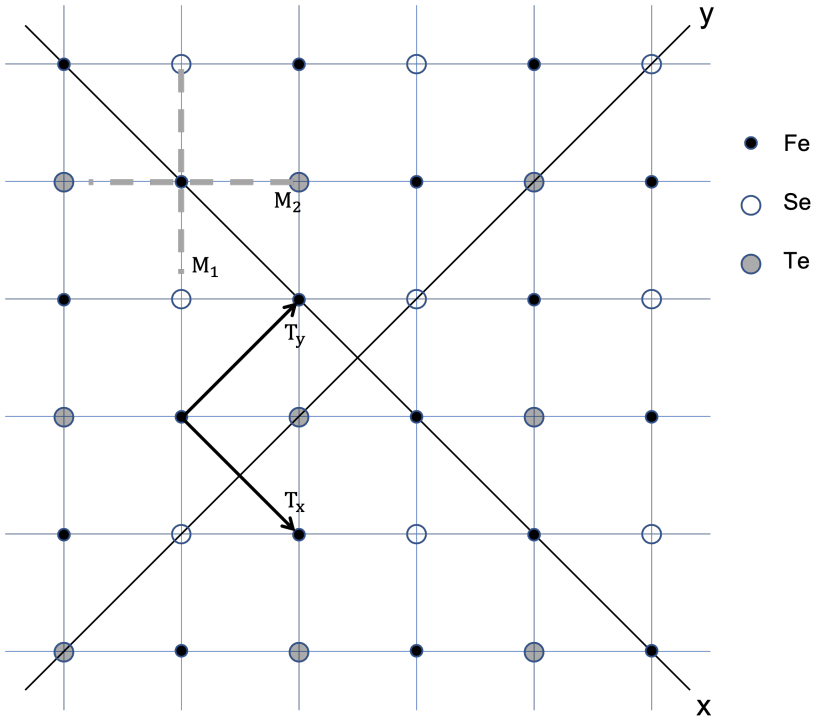

Figure 3.2: The lattice structure of an FTS monolayer. Fe-atoms are marked by dark circles, Se/Te atoms that are located off the Fe-plane alternately above and below the plane,by the shaded circles for above and hollow circles for below. The half-translations $\hat{T}_{x/y}$ and the mirror planes $M_{1,2}$ are also shown.

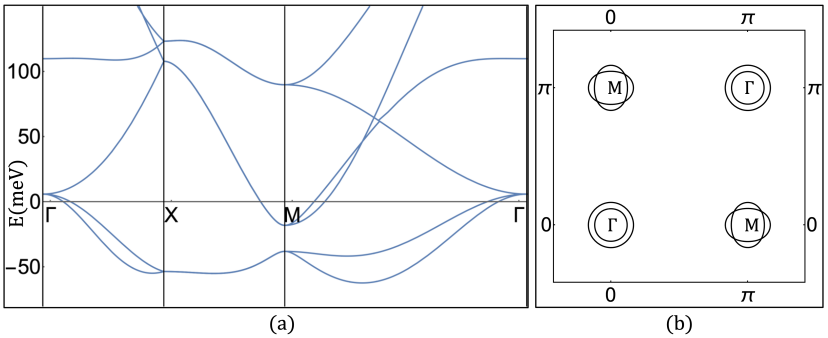

Figure 3.3: The band structure of FTS monolayer along the high symmetry line $\Gamma X M \Gamma$ showing the two hole-like pockets around Γ point and two electron-like pockets around M point (a). The Fermi contour is shown where the Γ pockets are circular and M pockets are slightly elliptical (b).

3.3 Microscopic model

After setting up the π-junction mechanism with a schematic of Γ and M pockets with $s_{\pm}$ pairing state, we now construct an effective model for the Fermi pockets of FTS mono layer.

In order to understand the symmetries of the FTS mono layer let us briefly describe its structure as shown in Fig. 3.2. The Fe atoms forms a square lattice on a 2D plane – we can call it the Fe-plane. In the Fig. 3.2 the Fe-atoms are shown by dark filled circles. The chalcogen atoms (Te/Se) are located off the Fe-plane alternately above and below the plane. In the Fig. 3.2 the atomic locations that are above the plane are marked by shaded circles and the ones below the plane by hollow circles. The alternate up and down chalcogen locations break the original translation symmetry of the Fe-plane along the nearest Fe-Fe bond directions that are represented by $\hat{T}_{x,y}$ in the Fig. 3.2.

A mono layer of FTS has:

i) The inversion symmetry

ii) The time-reversal symmetry (TRS)

iii) The two fold rotation symmetry around the x and y axes that pass through the Fe atoms ($C_2^{x,y}$ in Fig. 3.2)

iv) The Mirror reflections across the diagonal directions of the plane ($M_{1,2}$ in Fig. 3.2)

v) The glide reflection symmetries that are a combination of a half-translation ($\hat{T}_{x,y}$) followed by a mirror reflection about the xy-plane (M_z).

With the symmetries of the Hamiltonian described we now move on to describe the relevant basis for our model.

The superconductivity of the FTS mono layer originates from the two circular hole-like Γ pockets and two slightly oblate-shaped electron-like M pockets. The orbitals that contribute to these Fermi pockets are the three Fe-3d orbitals, viz., $3d_{x^2-y^2}$, $3d_{xz}$, $3d_{yz}$ orbitals according to the DFT based band structure calculations [39, 40]. The band components are also compatible with the polarization selective ARPES measurement of the band states near the high symmetry points. Thus, it is reasonable to consider these three orbitals as the basis for our effective model of the FTS Fermi pockets.

Now we describe the construction of the tight binding model (TBM) that we will use for our investigation of the BdG spectrum and the DW induced scattering problem. We note that we are ignoring the chalcogen orbitals for our modeling as near the Fermi level they do not contribute to the band structure. However, the alternate up and down locations of the Fe-plane, the two nearest Fe-atoms in the square lattice

become inequivalent and hence the Fe-lattice picks up a two-dimensional sub lattice index. In other words, the basis for our model consists of three d-orbitals located at the Fe-sites along with a sub lattice index, thus, there are total six degrees of freedom and total six bands from our model (neglecting spin for which each band would be doubly degenerate in general).

Each of the d-orbitals have different symmetry properties. For instance, the d_{xz} (d_{yz}) orbital remains invariant under the rotation around y-axis (x-axis) but changes sign under rotation around x-axis (y-axis). These symmetry properties are used to constrain the hoping matrix elements of the Hamiltonian between various orbitals in our TBM model. In particular, the behavior of orbitals involved in a specific hoping term, under various symmetry operators of the Hamiltonian, constrains and connects various hoping terms for the Hamiltonian. A detailed discussion for this symmetry constrained approach of constructing TBM of the FeSe can be found in Ref. [41]. Hence, we avoid that discussion for the purpose of brevity. We will only discuss on specific property of the Hamiltonian under the half-translation symmetries ($\hat{T}_{x,y}$) since that would be useful in modeling the half-unit-cell-shift domain wall in the lattice.

As can be intuitively understood from the Fig. 3.2, the operators that translate the lattice by nearest Fe-Fe bond length both along x- and y- directions (denoted by $\hat{T}_{x,y}$) are not exact symmetries of the system. Rather, they are half of lattice translations. This implies that such an operator applied twice keeps the Hamiltonian invariant which means that the terms in the Hamiltonian are either even or odd under $\hat{T}_{x,y}$, based on which the Hamiltonian can be split into two parts, $\hat{H} = \hat{H}_+ + \hat{H}_-$ such that $\hat{T}_{x,y}\hat{H}_\pm\hat{T}_{x,y}^{-1} = \pm\hat{H}_\pm$. Such a decomposition is useful in thinking about the effect

of the HUCS defect in our model. If we consider a scenario where the HUCS defect is along y-direction, on one side of the defect the terms associated with $\hat{H}_-$ would flip sign w.r.t. the defect free lattice Hamiltonian, i.e., $\hat{H}_-^D(x>0) = -\hat{H}_-(x>0)$.

With these discussions about the symmetry properties of the system Hamiltonian we now list out the possible nearest neighbor and next-nearest neighbor terms that our allowed by our basis choice. The resultant momentum-space Hamiltonian matrix elements, $H_{ij}^{\alpha\beta}(k) \equiv \langle \phi_i^\alpha(k)|\hat{H}(k)|\phi_j^\beta(k)\rangle$, have the following form,

$$
\begin{aligned}
&\text{Intra-sub-lattice hoping terms:} \\
&H_{ii}^{aa} = H_{ii}^{bb} = \epsilon_i + 4u_i \cos k_x \, \cos k_y \quad : \quad i = 1,2,3 \\
&H_{12}^{aa} = 4iu \cos k_x \sin k_y = -H_{21}^{aa} = -H_{12}^{bb} \\
&H_{13}^{aa} = 4iu \sin k_x \cos k_y = -H_{31}^{aa} = -H_{13}^{bb} \\
&H_{23}^{aa} = -4u_{23} \sin k_x \sin k_y = H_{32}^{aa} = H_{23}^{bb} \\
&\text{Inter-sub-lattice hoping terms:} \\
&H_{11}^{ab} = 2t_1(\cos k_x + \cos k_y) \\
&H_{22,33}^{ab} = 2(t_{x,y} \cos k_x + t_{y,x} \cos k_y) \\
&H_{12}^{ab} = H_{21}^{ab} = -2it \sin k_y \\
&H_{13}^{ab} = H_{31}^{ab} = 2it \sin k_x
\end{aligned}
\tag{3.1}
$$

Due to rotational symmetries we have $\epsilon_2 = \epsilon_3$ and $u_2 = u_3$. Furthermore, among all the matrix elements listed above $H_{12,13}^{aa}, H_{12,13}^{ab}$ are matrix elements of $\hat{H}_-$ whereas the rest are of $\hat{H}_+$ [41].

Now that the form of the Hamiltonian is set, the next step is to adjust the model parameters to simulate the Fermi pockets of the system. As discussed earlier the Fermi

contour of FTS mono layer consists of two circular shaped hole-like pockets around the Γ point $(k_x, k_y = 0, 0)$ and two slightly oblate-shaped electron-like pockets around the M point $(k_x, k_y = 0, \pi)$ as shown in the Fig. 3.3. For our purpose we focus on the following properties of the FTS Fermi pockets:

i) The shape and size of the Γ and M pockets

ii) The relative Fermi energies of the electron- and hole-like bands

These parameters can be approximately obtained from ARPES band structure. After fitting the parameters a reasonable band structure along the high symmetry lines and the associated Fermi contour are shown in Fig. 3.3.

This is a typical model that we use for our numerical evaluation of the BdG spectrum and solution of the DW induced scattering problem. We do vary our model parameters in order to study the robustness of the effects, however, we keep the above-mentioned features of the Fermi surface within the error range of various ARPES data. With that constraints the variation of the model parameters mainly have the effect of changing the band curvature and slightly modifying the shape of the Fermi contours which translate to change in DOS at various energy momentum window of the band structure including near the Fermi level.

3.4 Numerical results

Using the model described in the previous section we perform two types of numerical evaluation:

i) Calculation of the scattering problem due to the HUCS DW,

ii) Calculation of the BdG spectrum with $s_{\pm}$ pairing potential.

For the purpose of solving the scattering problem we utilize the python based KWANT package from which we specifically extract the transmission matrix at the Fermi level. For the purpose of calculating the BdG spectrum we introduce an $s_{\pm}$ pairing gap in the model Hamiltonian and study the ABS spectrum when there is an HUCS DW.

3.4.1 Solving the scattering problem

Let us consider the case when the DW is along the y-axis which means that the defect destroys the translational symmetry of the lattice only along x-direction keeping y-direction intact. Thus, we can treat the problems independently for each k_y in the Brillouin zone. The DW would then mix the states between various values of k_x for each value of k_y. Thus, solving the scattering problem would output scattering matrix that is a function of k_y and energy, E.

In KWANT the defect can be modeled for each of value of k_y as two leads that are half-shifted along x-direction w.r.t. each other. In this case, no scattering region is required as this is just a crystalline shift. The half-shift can be modeled simply by changing the sign of terms associated with $\hat{H}_-$ between the two leads.

As we are interested only in the transmission amplitudes for the reasons described in Sec. 3.2, we only take the transmission matrix from the KWANT output. At the Fermi energy since there are four modes for each k_y (two from the Γ pockets and two from the M pockets). Thus, each transmission matrix would be 4×4 where the two

dimensional blocks at the diagonals represent intra-pocket transmission whereas the off-diagonal blocks correspond to inter-pocket transmission.

Denoting the momentum modes from the Γ pockets as k_i and from the M pockets as q_i where $i = 1, 2$ correspond to the two pockets around each high symmetry point, the intra-pocket transmissions can be denoted by $t_{k_i k_j}$ and $t_{q_i q_j}$ and the inter-pocket transmission amplitudes by $t_{k_i q_j}$. Thus, the total intra-pocket transmission probability and the total inter-pocket transmission probability can be expressed as:

$$\begin{aligned} P_{\text{intra}}(E=0) &= \sum_{k_y,i,j} [|t_{k_i k_j}(k_y,0)|^2 + |t_{q_i q_j}(k_y,0)|^2] \\ P_{\text{inter}}(E=0) &= \sum_{k_y,i,j} [|t_{k_i q_j}(k_y,0)|^2 + |t_{q_i k_j}(k_y,0)|^2] \end{aligned} \tag{3.2}$$

For the two limiting cases considered while discussing the π-shift mechanism, only one of these two terms is non-zero. For the cases of pure intra-pocket and pure inter-pocket transmissions these quantities are $P_{\text{intra}} = 1$, $P_{\text{inter}} = 0$ and $P_{\text{inter}} = 1$, $P_{\text{intra}} = 0$ respectively. As we explain in Sec. 3.4.3 the relative difference between the two quantities, i.e., $\delta P = P_{\text{inter}} - P_{\text{intra}}$ can be used to quantitatively correlate to the junction stability.

3.4.2 Calculation of the BdG spectrum

Here we describe the Evaluation of the BdG spectrum. To model a BdG Hamiltonian first we need to choose a pairing for our model. As discussed earlier that the FTS mono layer possesses unconventional $s_{\pm}$ pairing state, we consider the simplest potential that changes sign from Γ $(k_x, k_y = 0, 0)$ to M $(k_x, k_y = 0, \pi)$, which is given by $\Delta(k) = \Delta_0 + 2\Delta_1 \cos k_x \cos k_y$. If $|\Delta_1/\Delta_0|$ is chosen appropriately, $\Delta(k)$, would have

opposite sign at the Γ and the M pockets. For simplicity we consider the pairing to be proportional to the identity matrix in the orbital and sub-lattice indices. Such a pairing term has the form:

$$\Delta_{ij}^{ab}(k_x, k_y) = \delta^{ab}\delta_{ij}(\Delta_0 + 2\Delta_1 \cos k_x \cos k_y) \tag{3.3}$$

With this $s_\pm$ pairing we construct the HUCS DW similar as before by discretizing our model in x-direction whereas keeping the y-direction periodic and across the defect the terms associated with the $\hat{H}_-$ are flipped in sign. As we want to compare the ABS levels between the cases of 0- and π-junction, we model both the junctions in our BdG Hamiltonian and calculate the corresponding spectra separately.

Let us look at a typical BdG spectrum from modeling such a junction in Fig. 3.4. One can see that the spectrum as a function of k_y has a gap which is the SC gap, but also possesses levels that lie in between the gaps, which correspond to the ABS. In the Fig. 3.4 the BdG spectrum for a typical set of model parameters for the FTS mono layer is plotted both for the cases of 0-junction and π-junction. From the spectrum it is apparent that the ABS levels are closer to the Fermi level for the case of 0-junction than the case of π-junction. Since at zero temperature the levels till the Fermi level are occupied, this implies that the π-junction has lower energy in this case since the bulk states that are outside the SC gap remain insensitive to the phase-twist across the junction [42]. Hence, one can use the difference in the occupied energies of the ABS levels between the cases of 0- and π-junction as the indicator to determine the stability of the junction. In particular, for a given set of model parameters, whichever junction has lower ABS energies up to the Fermi level is more stable than the other junction.

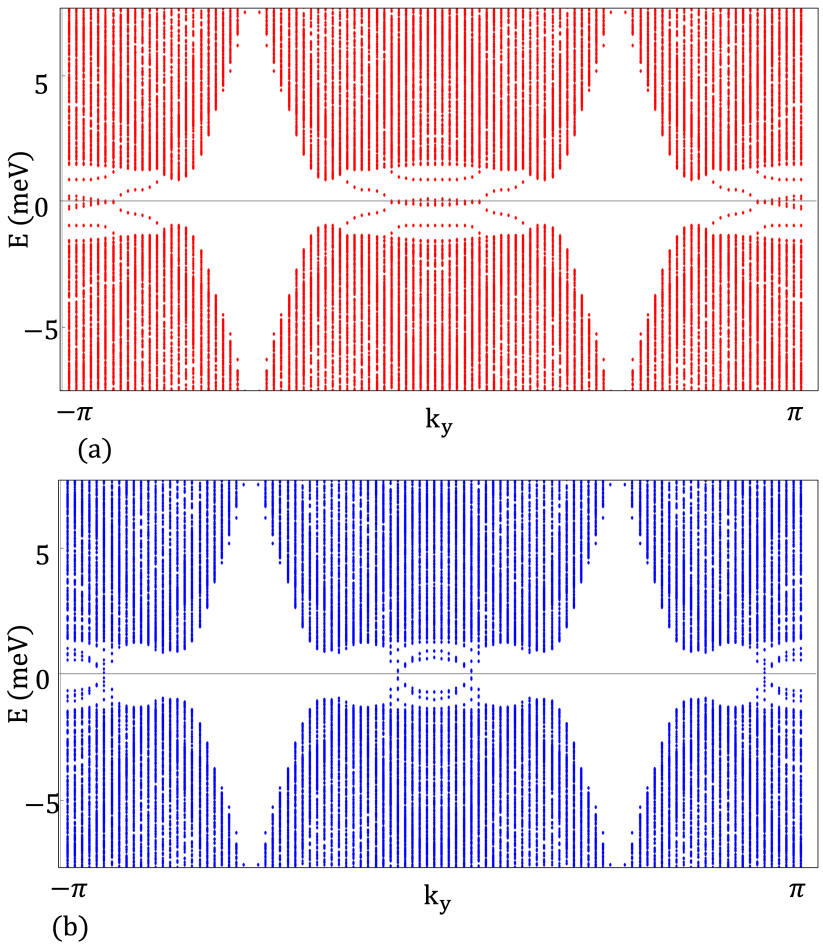

Figure 3.4: Typical BdG spectra for the cases of (a) 0-junction and (b) π-junction. The sub gap energy levels are typically much closer for the case of 0-junction (a) than that of π-junction (b).

To further formalize the stability criteria of the junction, we define the difference between the ABS energies as follows:

$$\delta E \approx E^{\pi}_{\mathrm{ABS}} - E^{0}_{\mathrm{ABS}} = \sum_{k_y,n} [|E^{n}_{\mathrm{ABS}}(k_y,\pi)| - |E^{n}_{\mathrm{ABS}}(k_y,0)|] \tag{3.4}$$

where n spans the set of discrete levels correspond to the ABS.

The sign of δE would determine which junction has lesser energy as $\delta E < 0$ and $\delta E > 0$ would imply 0- junction and π-junction are preferred respectively. In fact larger

the value of δE more the π-junction is stable as the probability of π-junction stability is proportional to exponential of δE as $p_\pi \propto \exp[\beta\, \delta E]$. For the model parameters that simulate a band structure as shown in Fig. 3.3, $\delta E > 0$ implying that π-junction is thermodynamically stable.

3.4.3 Analysis of the numerical results

In order to substantiate the intuitive mechanism that we proposed in Sec. 3.2, we vary our model parameters such that all of them roughly simulate the FTS band structure near the Fermi surface. Variation of the parameters alter the band structure in this case keeping the main features of FTS mono layer intact that are listed before. Only the band curvatures and the Fermi contour shapes are slightly altered by this variation. In Fig. 3.5 the resultant band structure from such a parameter variation is shown.

While studying the BdG spectrum for a wide range of parameters provides an opportunity to verify the robustness of the π-junction, a comparison to the relative inter-pocket transmission probability would facilitate us to substantiate our claim of the mechanism as we discuss in later part of this section.

The results from performing BdG spectrum calculation for a range of model parameters reveal that for a large fraction of models the π-junction is indeed favored. Such events are characterized by $\delta E > 0$. Furthermore, for each such model we also evaluate the relative inter-pocket transmission probability via $\delta P = P_{\text{inter}} P_{\text{intra}}$. When we plot δE and δP together in Fig. 3.6 we see that the two quantities are

positively correlated which basically shows a strong correlation between larger inter-pocket transmission strength and the stability of the π-junction. The quantitative correlation shown in the plot supports the fact that inter-pocket mixing due to the HUCS DW tends to favor the π-junction over the 0-junction.

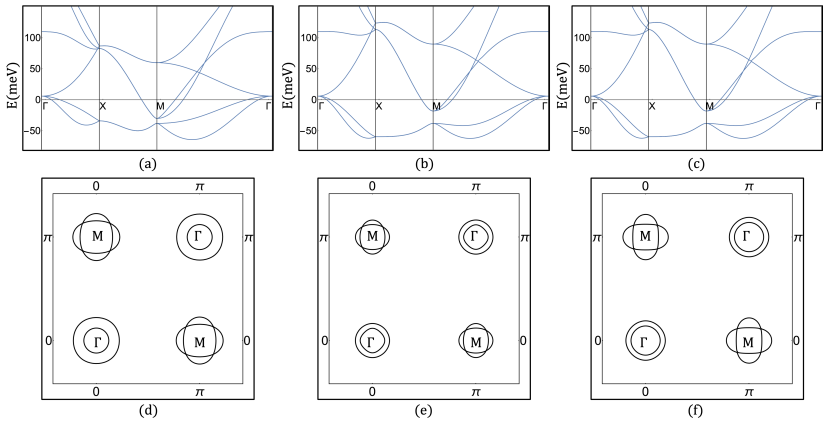

Figure 3.5: A sample of resultant band structures (a)-(c) and the corresponding Fermi contours (d)-(f) due to variation of the model parameters.

3.5 Summary and Conclusion

In this paper we have proposed a mechanism that favors a π-shifted order parameter across a crystalline defect associated with half-unit-cell-shift of the lattice when the bulk s-wave OP has opposite signs between two pockets. In such a scenario the crystalline defect can couple the modes between the two pockets which effectively couples the corresponding OPs of opposite signs from the two sides of the domain wall. As discussed, using Andreev reflection process, if the inter-pocket transmission is dominant, a π-shifted OP lowers the energy of the occupied ABS at the junction compared to the 0-junction case. This mechanism can give rise to a π-shifted OP in

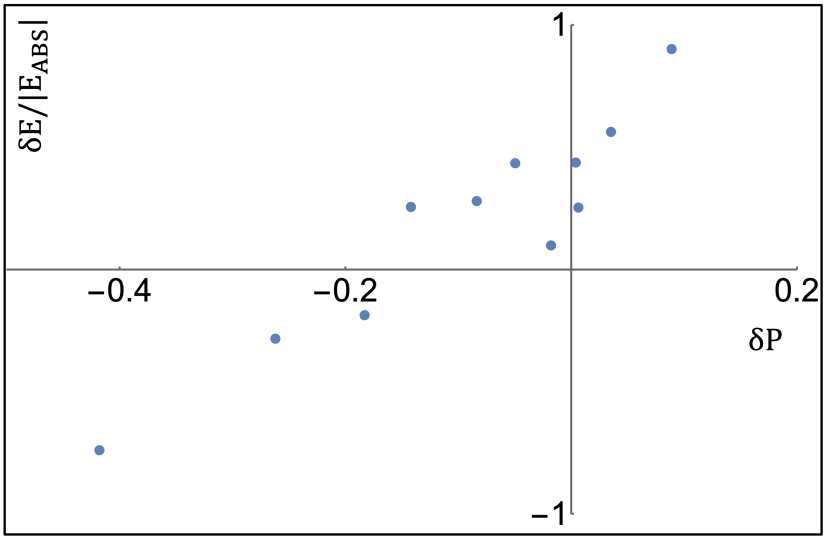

Figure 3.6: The energy of π-junction relative to 0-junction is plotted along y-axis with the x-axis plotting the corresponding inter-pocket transmission strength relative to the intra-pocket transmission.

mono layers of FTS across the HUCS DW.

We built an effective model for an FTS monolayer using the tight binding approach including the three d-orbitals that are centered at the Fe atomic sites. The parameters for the model were chosen such that the shape and size of the Fermi contours reasonably match the ARPES data along with the relative Fermi energies of the electron- and hole-like bands of the system. Variation of our parameters around the base model allowed us to conclude from the BdG spectrum that for a large fraction of the model parameters, indeed, the π-junction has lower energy than the 0-junction. More importantly, comparison with the relative inter-pocket transmission showed a strong correlation between larger inter-pocket transmission and the stability of the π-junction which we show in Fig. 3.6 by plotting the energy difference between the occupied levels of the 0-junction and

the π-junction. This is the central result of this study that supports our proposed mechanism that domain wall induced mixing between the Γ and M pockets favors the π-junction across the defect.

We also discussed how a π-junction at the shifted bulk mono layer of FTS would naturally induce a π-shift in the TSC gap on the surface which would then accommodate helical Majorana modes with the signatures as observed in the recent STS experiment.

In conclusion we have presented a mechanism for a π-shift of the OP when in case of a multi-pocket superconductivity where the OPs between two pockets are intrinsically π-phase shifted. In such scenario if a linear domain boundary can mix the modes between the two pockets strongly enough, the junction would favor an overall π-phase shift contrary to the more conventional case of no phase shift.

Chapter 4

Probing spin modes in a Luttinger liquid with superconducting leads

4.1 Introduction

In this chapter we consider another kind of Josephson junction (JJ) which can be formed by sandwiching an interacting 1D quantum wire, known as Luttinger liquid (LL), between two semi-infinite superconducting (SC) leads. We focus on the electromagnetic (EM) response of such a setup in presence of impurity potential that is measurable in a transport measurement. The results presented are based on a manuscript, in preparation for publication [15].

The problem of interacting electrons in a one-dimensional metal can be solved exactly for arbitrary interaction strength as long as the interaction is local density-density type owing to the Luttinger liquid (LL) theory [14]. This is a very special case of one-dimensional systems. The LL theory is valid around the Fermi level within an energy scale much smaller than the Fermi energy of the bands. More interestingly, for the case of spin-1/2 electrons, at long wavelengths, the eigen states for the interacting Hamiltonian are separated into two sets, viz. the charge density excitations and spin density excitations. This decoupling of the charge and spin modes is known as the spin-charge separation.

However, the spin-charge separation breaks down if the Hamiltonian has terms allowing back-scattering processes where a right moving electron is scattered to a left

moving electron by the impurities present in the system. This low energy process that requires large momentum transfer can happen when the length scale associated with the impurity potential is of the order of inverse Fermi momentum, k_F^{-1}. Since impurity is ubiquitous in any system, the pure spin-charge decoupling is expected to break down in a real quantum wire. The signatures of such impurity induced spin-charge coupling will be the focus of this chapter.

Specifically we investigate how the signatures of the spin modes in the system can be experimentally probed with a setup involving a 1D quantum wire between two semi-infinite superconducting (SC) leads. We find that in an experiment where only the charge modes are accessible the impurity induced spin-charge coupling can facilitate the observation of spin modes in the optical absorption spectrum in certain limits of density and interaction strength that may be accessible to a realistic experiment.

The setup we consider is shown in Fig. 4.1 where a long wire is sandwiched between two SC leads. In the limit where the length of the wire is much larger than the SC coherence length, perfect Andreev reflection at the two normal-superconductor (NS) interfaces form the Andreev bound states (ABS). One key aspect of having SC leads is the blockage of spin current through the NS interface. This is because during the Andreev reflection an electron is converted to a counter-propagating hole of opposite spin via a phase shift. As a result at the interfaces the densities of the electronic species are constrained as $\rho_{R\uparrow}(x_{\rm bdy})+\rho_{L\downarrow}(x_{\rm bdy}) = 0$ and $\rho_{R\downarrow}(x_{\rm bdy})+\rho_{L\uparrow}(x_{\rm bdy}) = 0$. Considering the expression of the spin current, $j_\sigma \propto [\rho_{R\uparrow} - \rho_{R\downarrow} - \rho_{L\uparrow} + \rho_{L\downarrow}]$, these constraints imply that $j_\sigma(x_{\rm bdy}) = 0$. Thus, in the low energy limit the spin modes get trapped within the normal region as long as there is no spin-charge coupling. However, spin-charge

coupling can allow the spin modes to leak through the interfaces which would be visible in transport measurements. As discussed above in a real system impurity induced back-scattering processes can couple the spin and charge modes and thus, facilitate a way to probe the spin modes experimentally. In our work using numerical evaluation we find specific signatures of the impurity induced spin-charge coupling in an SC-LL-SC (S-LL-S) setup as represented in Fig. 4.1.

Thus, considering a model of 1D low energy interacting electronic system we introduce a disorder potential to model the impurity induced scattering processes. The bosonization procedure we use to tackle the interactions are modified due to the SC leads imposing non-trivial boundary conditions in a similar way discussed in [43]. We treat the impurity potential perturbatively and derive the absorptive part of the conductivity response function. The key signatures that we point out in the absorption spectrum is that the peak strength associated with the charge mode and spin mode excitations are comparable when the Fermi momentum, k_F, is of the order of the length scale associated with the impurity potential. In that regime specifically the spin modes can be distinguished by tuning the Coulomb interaction strength. As varying the same alters the charge gap while keeping the spin gap intact, the energy spacing corresponding to the charge peaks will shift accordingly, keeping the spin peaks constant on the energy axis. Since in a 1D system the density and hence k_F as well as the interaction strengths are tunable to a certain extent by gating [44], the spin modes that are low energy signatures of the back-scattering processes can be probed experimentally in a transport measurement with S-LL-S setup.

Now we layout a brief outline of this chapter. We start by describing the low

energy non-interacting fermionic spectra for an SNS junction in Sec. 4.2.1. In the particle-hole basis the spectrum have been previously [45] obtained by solving the Schrodinger's equation with appropriate boundary conditions that simulate the leads [See Fig. 4.1 for a schematic setup]. The non-trivial effect of SC leads is the well-known Andreev reflection that takes place at the NS interfaces which connects an electron to its counter propagating hole counterpart via a phase shift assuming semi-infinite SC leads. This connections are discussed in the following subsection [Sec. 4.2.2] where we introduce a set of two chiral fields, defined on an extended manifold of twice length [Fig. 4.1], that naturally connects the particle fields and the reflected hole fields. In the next subsection, Sec. 4.2.3, by bosonizing the chiral fields and the conventional particle fields and using their connections derived in Sec. 4.2.2 we derive the boundary constraints for the charge and spin bosonic fields due to the SC leads. The constraints that are originally put on the fermionic fields are thus translated to the spin-charge bosonic fields. The detailed steps to derive the boundary conditions for the spin-charge bosonic fields due to the SC leads are derived in Appendix A.1. Since the interacting Hamiltonian is solved in terms of these bosonic fields, finding the correct boundary conditions for those fields is a crucial step while expanding them in second quantized discrete operators. The interacting Hamiltonian is then diagonalized and the transformations leading to the diagonal basis are described in Appendix A.2. The diagonal basis obtained would be used in our numerical calculation part (Sec. 4.3.2) to explicitly calculate the absorption spectrum which contains matrix elements of the impurity Hamiltonian in terms of the interacting diagonal bosonic basis. In Sec. 4.3.1 we introduce the Hamiltonian that models the back-scattering impurity potential. We

introduce a Gaussian disorder potential as an envelope to the back-scattering terms in the Hamiltonian. The resultant form of the absorption spectrum is obtained using linear response formalism by treating the impurity potential perturbatively [details of the linear response formalism in Appendix A.3]. The correlators contain the matrix elements of the impurity Hamiltonian between the ground and excited states of the unperturbed system. In Sec. 4.3.3 the explicit computation of the required matrix elements are described in Sec. 4.3.3 and in Appendix A.4. Finally, the numerical results are described in Sec. 4.4. After describing the length scale regime where the bosonization scheme is valid we tune the Fermi momentum of the system and present the consequent results in Sec. 4.4.1. We find that when the Fermi momentum, k_F, is of the order of inverse of length-scale, λ, associated with the variation of the disorder potential, the spin peaks have the highest intensity in the absorption spectrum which is comparable to the charge peak strengths. It is this regime of the Fermi momentum where the spin peaks would be most visible in an experimental setup. The Fermi momentum in a 1D system can be tuned by varying the total density of the electrons via gating as discussed in Ref. [44]. After setting the appropriate Fermi momentum for our numerical evaluation we then, in Sec. 4.4.2, tune the interaction strength which only results in the charge excitation gap variation while keeping the energy spacing of the spin excitations fixed. This can be achieved in an experiment by tuning the Coulomb interaction strength. The tuning of the interaction strength helps to distinguish the spin peaks from the charge peaks as the charge peaks shift along the energy axis whereas the spin peaks remain stationary. Finally, in Sec. 4.5 we summarize the numerical results.

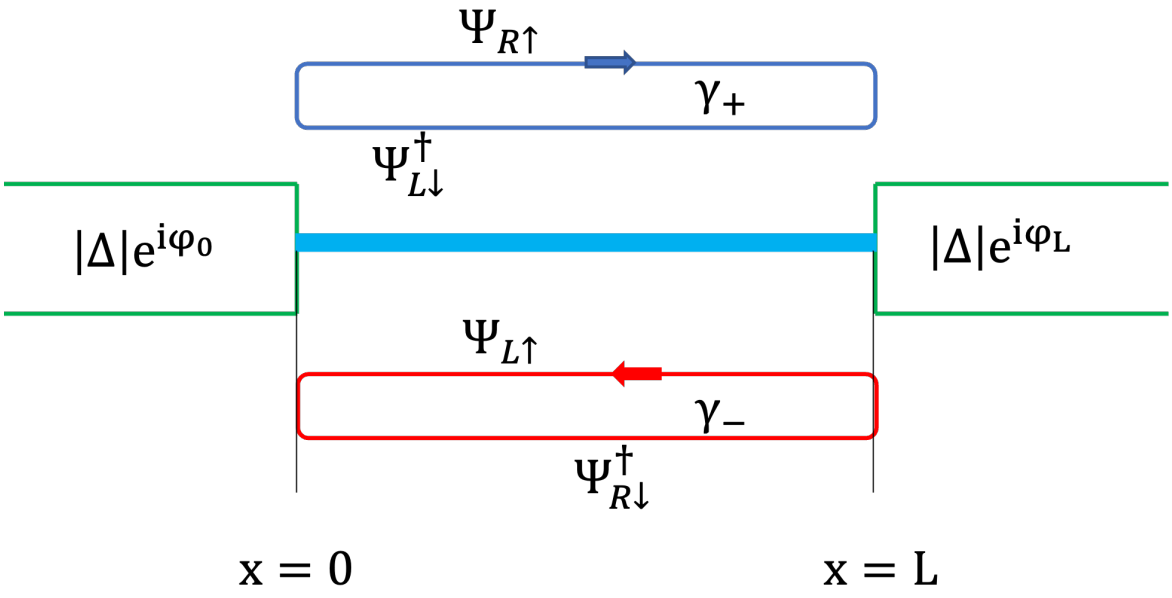

Figure 4.1: Schematic for the 1D S-LL-S junction setup. At low energy the chiral fields denoted by γ_+ (for right moving current) and γ_- (left moving current) contain the eigen modes of the non-interacting system.

4.2 The low-energy Andreev bound states and bosonization

In this section we build the theoretical framework for the interacting 1D wire in the S-LL-S setup. The conventional bosonization scheme of an infinite 1D system needs modification if there are boundaries in general [46, 14]. In the special case of a finite size quantum wire between two SC leads the fermionic dispersion on which bosonization is performed consists of the Andreev bound states that are trapped within the normal region. In the low energy limit compared to the SC gap, the spectrum of the ABS modes is approximately linear which is where the density-density interaction can be treated exactly in the LL theory. We consider this low energy limit for the ABS modes and perform bosonization and obtain the diagonal second quantized basis for

the interacting case that would facilitate us to incorporate the impurity potential and calculate the resulting absorption spectrum.

4.2.1 The non-interacting fermionic spectrum

The treatment of the non-interacting problem with SC leads requires introduction of the Nambu spinor basis to incorporate the particle and hole fields for spin-1/2 electrons. The Nambu spinor is defined as a vector with its components corresponding to the particle and hole component for each spin, viz., $\hat{\Psi}^T = (\psi_\uparrow, \psi_\downarrow^\dagger)$. The SC gap at the semi-infinite leads couple the particle and hole sectors via Andreev reflection at the NS interfaces that result in the ABS being an equal superposition of electron and hole modes.

In the Nambu basis introduced above the Bogoliubov de Gennes (BdG) Hamiltonian has the following form [47]:

$$\hat{H}_{\text{BdG}} = \int dx\, \hat{\Psi}^\dagger(x) \begin{bmatrix} \hat{H} - \mu & \Delta(x) \\ \Delta^*(x) & \mu - \hat{H} \end{bmatrix} \hat{\Psi}(x) \tag{4.1}$$

where $\hat{H}$ represents the spin-symmetric single-particle Hamiltonian, μ is the chemical potential which we assume to be same for the normal region and the two SC leads and $\Delta(x)$ is the SC order parameter (OP).

In our setup (Fig. 4.1) since we focus on a long quantum wire such that the SC coherence length (typically denoted by ξ) is negligible compared to the length of the system, L. In that limit $\Delta(x)$ in Eq. 4.1 can be approximated to be zero within the

normal region and constant at the leads where the SC phase might differ between the two leads. Such a profile for $\Delta(x)$ can be expressed as

$$\begin{aligned} \Delta(x<0) &= \Delta_0\, e^{i\varphi_0}, \\ \Delta(x>L) &= \Delta_0\, e^{i\varphi_L}, \\ \Delta(0<x<L) &= 0. \end{aligned} \tag{4.2}$$

where Δ_0 is the constant magnitude of the SC gap for the leads and φ_0 and φ_L are the associated phases of order parameter (OP) at the two boundaries, $x = 0$ and $x = L$, respectively.

In the limit of long-wavelengths and low energies, the problem given by Eq. 4.1 decouples to a pair of simpler problems each with a 2D Hilbert-space as we discuss below. When the length of the system, L, is much larger than the microscopic length-scales such as inverse Fermi momentum, k_F^{-1}, the particle fields can effectively be expanded around the two Fermi points, $\pm k_F$, as $\psi_s \approx \psi_{Rs}\, e^{ik_F x} + \psi_{Ls}\, e^{-ik_F x}$, where the fields ψ_{Rs} and ψ_{Ls} describe the right and left moving electrons for each spin, $s = \uparrow / \downarrow$, with energies around the Fermi level, μ. Furthermore, to capture only the low energy processes the single-particle Hamiltonian can be expanded around the Fermi level as $\hat{H} - \mu \approx -iv_F\partial_x$ where v_F is the Fermi velocity. Substituting these approximations in Eq. 4.1 and ignoring the short-wave length terms, the resultant low energy Hamiltonian

decouples to two parts, $\hat{H}_{\rm BdG} \approx \hat{H}_+ + \hat{H}_-$, which are given by [43]:

$$\begin{aligned}
\hat{H}_+ &= \int dx \begin{bmatrix} \psi^\dagger_{R\uparrow} & \psi_{L\downarrow} \end{bmatrix} \begin{bmatrix} -iv_F\partial_x & \Delta(x) \\ \Delta^*(x) & iv_F\partial_x \end{bmatrix} \begin{bmatrix} \psi_{R\uparrow} \\ \psi^\dagger_{L\downarrow} \end{bmatrix} \\
\hat{H}_- &= \int dx \begin{bmatrix} \psi^\dagger_{L\uparrow} & \psi_{R\downarrow} \end{bmatrix} \begin{bmatrix} iv_F\partial_x & \Delta(x) \\ \Delta^*(x) & -iv_F\partial_x \end{bmatrix} \begin{bmatrix} \psi_{L\uparrow} \\ \psi^\dagger_{R\downarrow} \end{bmatrix}
\end{aligned} \tag{4.3}$$

where $\hat{H}_+$ and $\hat{H}_-$ describe the right and left moving up-spin electrons along with their corresponding counter propagating holes in the normal region. Thus, $\hat{H}_\pm$ effectively describes two chiral channels associated with particle current flowing along right and left directions.

The spectrum for $\hat{H}_\pm$ can be independently obtained by solving the corresponding eigenvalue problems given by

$$\begin{bmatrix} \mp iv_F\partial_x & \Delta(x) \\ \Delta^*(x) & \pm iv_F\partial_x \end{bmatrix} \begin{bmatrix} u_\pm \\ v_\pm \end{bmatrix} = E_\pm \begin{bmatrix} u_\pm \\ v_\pm \end{bmatrix} \tag{4.4}$$

For the setup described by $\Delta(x)$ in Eq. 4.2, the solutions $(u_\pm,\, v_\pm)^T$ are obtained by separately solving for the normal region ($\Delta = 0$) and the SC leads ($\Delta \neq 0$) and matching the resultant wave functions at the NS interfaces, $x = 0, L$[45, 48] according to the standard quantum mechanical scattering theory.

For the bound states, when $|E| < \Delta_0$, the solutions in the SC regions ($|\Delta(x)| \neq 0$) are evanescent waves and can be obtained by substituting $(u_\pm,\, v_\pm)^T = (1,\, \alpha_\pm)^T e^{iq_\pm x}$ in Eq. 4.4 and solving for $\alpha_\pm$. On the other hand the propagating solutions for the normal region ($\Delta(x) = 0$) have the form $(u_\pm,\, v_\pm)^T \propto (e^{\pm iq_\pm x},\, \beta_\pm e^{\mp iq_\pm x})^T$ and $\beta_\pm$ can be

obtained similarly by substituting this form in the differential equation. Matching the two solutions at the boundaries ($x = 0,\ L$) the resultant ABS modes become discrete according to the finite length of the system. The solutions for the discrete ABS modes in the particle-hole basis are given by [45, 48, 43]

$$\begin{bmatrix} u_{\pm}^{n} \\ \\ v_{\pm}^{n} \end{bmatrix} = \frac{1}{\sqrt{2L}} \begin{bmatrix} e^{\pm i q_{\pm}^{n} x} \\ \\ e^{\pm i\eta(E_{\pm}^{n}) - i\varphi_0} e^{\mp i q_{\pm}^{n} x} \end{bmatrix} \tag{4.5}$$

where the energy dependent phase, $e^{\pm i\eta(E)}$ and the quantized momenta, $q_{\pm}^{n}$, are given by

$$\begin{aligned} e^{\pm i\eta(E_{\pm})} &= \frac{E_{\pm} \pm i\sqrt{\Delta_0^2 - E_{\pm}^2}}{\Delta_0} \\ q_{\pm}^{n} &= (n\pi + \eta)/L \pm \varphi/(2L) \end{aligned} \tag{4.6}$$

where n is an integer that denotes a specific mode and φ is the SC phase difference between two boundaries, i.e., $\varphi \equiv \varphi_L - \varphi_0$. The energy eigenvalue for each mode is related to the momentum as $E_{\pm}^{n} = v_F q_{\pm}^{n}$ and hence both of them need to be solved self-consistently.

In the low energy limit, however, i.e., $|E_{\pm}/\Delta_0| \to 0$, the eigen values can be approximated analytically as η becomes energy independent up to leading order according to Eq. 4.6, i.e., $\eta \to \pi/2$ [43]. As a result, the spectrum becomes linear with the dispersion

$$\begin{aligned} E_{\pm}^{n} &= v_F q_{\pm}^{n} \\ q_{\pm}^{n} &= \left[n + \frac{1}{2}\right] \frac{\pi}{L} \pm \frac{\varphi}{2L} \end{aligned} \tag{4.7}$$

It is this linear regime of the ABS spectrum that enables us to introduce the bosonization formalism to treat the density-density interactions in the system. Before

introducing the bosonization scheme we discuss how the particle and hole fields are connected at the boundaries of the normal region which would set some phase constraints in our bosonization scheme and would also dictate the basis functions for the charge and spin density fields accommodated within the S-LL-S setup.

4.2.2 Particle-hole connection and the chiral fields

The phase relations between the particle and hole fields are set by the Andreev reflections at the NS interfaces in the SNS junction. The solutions describing the ABS, as obtained in the previous subsection 4.2.1, are superpositions of particle and hole modes each having equal amplitude (i.e., $|u(x)| = |v(x)|$). This implies that they can differ only by a phase-factor at the boundaries, $x = 0, L$. Furthermore, we note that the $\hat{H}_{\pm}$ couples fields that carry current in the same direction, viz., $\hat{H}_{+}$ couples $\psi_{R\uparrow}$ and $\psi^{\dagger}_{L\downarrow}$ both of which contain right moving current modes and conversely for $\hat{H}_{-}$. This chiral nature of the fields involving the ABS modes becomes clearer when $\psi_{R,L\uparrow,\downarrow}$ are expressed in terms of operators representing the fermionic eigen modes.

Denoting the operators describing the solutions of $\hat{H}_{\pm}$ with eigen values, $E^{n}_{\pm}$, by $\gamma^{n}_{\pm}$, and using the basis expansion of the particle fields as $\psi_{R/L,\uparrow}(x) = \sum_n u^{n}_{\pm}(x)\gamma^{n}_{\pm}$ and $\psi^{\dagger}_{L/R,\downarrow}(x) = \sum_n v^{n}_{\pm}(x)\gamma^{n}_{\pm}$, in the low energy limit (i.e., setting $\eta = \pi/2$) the particle fields have the following expressions:

$$\begin{aligned} \psi_{R/L,\uparrow}(x) &= \sum_n e^{\pm i q^{n}_{\pm} x}\gamma^{n}_{\pm} \\ \psi^{\dagger}_{L/R,\downarrow}(x) &= -i\sum_n e^{\mp i q^{n}_{\pm} x}\gamma^{n}_{\pm} \end{aligned} \tag{4.8}$$

where $q^{n}_{\pm}$ are given in Eq. 4.6.

We observe that the eigen modes of $\hat{H}_+$, i.e., the γ_+^n operators, appear in the expressions of the right moving up-spin particle field ($\psi_{R,\uparrow}$) and its Andreev reflected hole counterpart ($\psi^\dagger_{L,\downarrow}$). Similarly, the eigen modes of $\hat{H}_-$ appear in $\psi_{L\uparrow}$ and $\psi^\dagger_{R\downarrow}$. This motivates us to combine these two pairs of particle-hole fields on a manifold of twice the length of the system and define two new fermionic fields accordingly. Such a choice of chiral fields are given by,

$$\gamma_\pm(x) = \frac{1}{\sqrt{2L}} \sum_n \gamma_\pm^n \, e^{\pm i q_\pm^n x} \quad x \in [-L, L], \tag{4.9}$$

From Eq. 4.8 we note that each of $\gamma_\pm(x)$ is related to an appropriate pair of particle and hole field in the extended manifold ($x > 0$ and $x < 0$) as:

$$\begin{aligned} \psi_{R\uparrow}(x) &= \gamma_+(x), \qquad & \psi^\dagger_{L\downarrow}(x) &= ie^{-i\varphi_0}\,\gamma_+(-x), \\ \psi_{L\uparrow}(x) &= \gamma_-(x), \qquad & \psi^\dagger_{R\downarrow}(x) &= -ie^{-i\varphi_0}\,\gamma_-(-x). \end{aligned} \tag{4.10}$$

Thus, the two fields, $\gamma_\pm(x)$, defined on $x \in [-L, L]$, represent the appropriate pairs of electron and hole fields that are connected via Andreev reflections. We note that this extended manifold trick is often used for 1D problem with an open boundary condition [46, 14]. Here, we have generalized the idea to the case of perfect Andreev boundaries.

The chiral nature of the $\gamma_\pm$ fields can be described as follows. In Fig. 4.1 we pictorially represent the extended manifold ($x \in [-L, L]$) as a folded loop on which the $\gamma_\pm$ fields are defined such that its upper half represents $x \in [0, L]$ and the lower half represents $x \in [0, -L]$. Thus, $\gamma_+(x)$ is proportional to a right moving particle field on the upper half of the blue loop and left moving hole field on the lower half of the same loop. Hence, modes on both halves of that loop carry particle current to the right as indicated by a rightward arrow in the middle of the loop. Similarly for the red loop in

the figure, $\gamma_-(x)$ is proportional to a field containing modes that carry current to the left, shown by a leftward arrow on the red loop [Fig. 4.1]. From that perspective we call $\gamma_\pm(x)$ as the chiral fields carrying particle currents in directions opposite to each other.

Furthermore, γ_+ and γ_- can be treated as independent variables and the linearized fermionic Hamiltonian within the normal region (i.e., Eq. 4.3) can be expressed in terms of them in the extended manifold as follows:

$$\hat{H}_\pm = \int_{-L}^{L} dx \, \left[\gamma_+^\dagger \left(-iv_F\partial_x\right)\gamma_+ + \gamma_-^\dagger \left(iv_F\partial_x\right)\gamma_-\right]. \tag{4.11}$$

The form of the linearized terms in the Hamiltonian with a sign difference in the velocity parameter v_F between the terms involving γ_+ and γ_- justify the chirality of the $\gamma_\pm$ fields.

Even though the boundary connections between the particle-hole fields can be obtained algebraically from the ABS solutions as shown in [43], the construction of the chiral fields described above, provides perhaps a more intuitive way to obtain the same results using the relations in Eq. 4.10. For instance, the mere continuity of the chiral fields along the extended manifold at $x = 0$, i.e., $\gamma_\pm(0^+) = \gamma_\pm(0^-)$, implies $\psi^\dagger_{L\downarrow}(0) = ie^{-i\varphi_0}\,\psi_{R\uparrow}(0)$ and $\psi^\dagger_{R\downarrow}(0) = -ie^{-i\varphi_0}\,\psi_{L\uparrow}(0)$. Similarly, the particle-hole connection on the other end of the wire ($x = L$) can be obtained by realizing that the chiral fields have a phase-twist between $x = -L$ and $x = L$. We can read off this phase twist from Eq. 4.9 which is given by

$$\gamma_\pm(-L) = -e^{-i\varphi}\gamma_\pm(L) \tag{4.12}$$

where $\varphi = \varphi_L - \varphi_0$. This phase-difference at $x = \pm L$ along with Eq. 4.10 translates to the particle-hole connection at $x = L$, as $\psi^\dagger_{L\downarrow}(L) = -ie^{-i\varphi_L}\,\psi_{R\uparrow}(L)$ and $\psi^\dagger_{R\downarrow}(L) = ie^{-i\varphi_L}\,\psi_{L\uparrow}(L)$. The particle-hole connections thus obtained impose constraints in the bosonic fields when the bosonization scheme is induced.

As alluded in the introduction an important consequence of these particle-hole connections is the opacity of the NS interface to the spin current. Expressing the particle densities as appropriate bi-linears of the particle-hole fields (e.g., $\rho_{R/L,s} = \psi^\dagger_{R/L,s}\psi_{R/L,s}$), the particle-hole connections at the boundaries relate the densities of different species as $\rho_{R\uparrow}(0,L) = -\rho_{L\downarrow}(0,L)$ and $\rho_{L\uparrow}(0,L) = -\rho_{R\downarrow}(0,L)$. Substituting these constraints it's easy to see that the charge density, $\rho_c \propto [\rho_{R\uparrow} + \rho_{L\uparrow} + \rho_{R\downarrow} + \rho_{L\downarrow}]$, and the spin current, $J_\sigma \propto [\rho_{R\uparrow} - \rho_{L\uparrow} - \rho_{R\downarrow} + \rho_{L\downarrow}]$, vanish at the boundaries of the wire:

$$\rho_c(0,L) = 0 \quad J_\sigma(0,L) = 0 \tag{4.13}$$

Vanishing charge density is associated with the energy gap at the Fermi level in the semi-infinite SC regions at both sides of quantum wire. More interestingly, the vanishing spin-current at the boundaries imply that the spin density modes are trapped inside the normal region. We would show, however, in Sec. 4.3.1 that impurity induced back-scattering processes can relax this constraint by coupling the charge and spin modes in the system and thus, allowing the spin modes to leak through the leads and appear in the conductivity spectrum.

4.2.3 Bosonization and the interacting Hamiltonian

In this sub-section we introduce the bosonization formalism for the particle fields following Ref. [14] and derive the constraints on the spin and charge bosonic variables set by the particle-hole connections explained in the previous subsection. Later, we would introduce second quantized operators and expand the spin-charge bosons in terms of them with the appropriate boundary constraints to solve the interacting Hamiltonian exactly.

In the bosonization scheme a fermionic field is expressed as an exponential of appropriate group of bosonic fields where the spatial derivative of the bosonic field is proportional to the long wave length density fluctuations of the fermionic field. If the fermionic non-interacting Hamiltonian can be expanded around the chemical potential in terms of linear power of spatial derivatives only, then the same Hamiltonian can be expressed in terms of the bi-linear of the spatial derivatives of the bosonic variables. Furthermore, since the bosonic variables represent density of the fermions, the density-density interactions between the fermions also appear as bi-linears of the density operators which can be readily solved by Bogoliubov transformations. We would elaborate these steps in this subsection.

Let us first recall the bosonized expressions for the conventional particle fields in terms of charge and spin bosons and then introduce bosonized expressions for the chiral fermionic fields introduced in Sec. 4.2.2. We would then compare the two sets of bosonized expressions and relate them according to the relations Eq. 4.10 which would naturally provide the required boundary conditions for the charge and spin bosons.

The bosonized expressions for the right and left moving particle fields ($\psi_{R/L,\uparrow/\downarrow}$) can be concisely written [14] as

$$\psi_{rs} = \frac{U_{rs}}{\sqrt{2\pi\alpha}} e^{if_r N_{rs}\pi x/L} e^{-\frac{i}{\sqrt{2}}(f_r\phi_c - \theta_c + t_s(f_r\phi_\sigma - \theta_\sigma))} \tag{4.14}$$

Explanation of each term in the bosonized expression is elaborated by Giamarchi in [14]. Here we only briefly describe them. Here $r = R, L$ with $f_{R/L} \equiv \pm 1$, and $s = \uparrow, \downarrow$ and correspondingly $t_{\uparrow/\downarrow} \equiv \pm 1$. U_{rs} is the fermionic annihilation operator associated with the fermionic species ψ_{rs}, a.k.a. the Klein factor, whereas N_{rs} denotes the corresponding occupancy of the same w.r.t. the ground state. In the denominator of the expression α is a length scale such that α^{-1} can be thought of as a momentum cutoff around the Fermi momentum till which the fermionic spectrum can be reasonably approximated to be linear. Finally, $\phi_{c,\sigma}$ and $\theta_{c,\sigma}$ are the density and phase bosonic fields which are conventionally used to describe charge (c) and spin (σ) density fluctuations of the fermions. The spatial derivatives of these bosonic variables are related to the charge and spin density and current according to $\rho_{c,\sigma} = -\partial_x\phi_{c,\sigma}/\pi$ and $j_{c,\sigma} = \partial_x\theta_{c,\sigma}/\pi$ [14].

Now we can similarly bosonize the chiral fields, $\gamma_\pm(x)$ using the same procedure for the particle fields. Keeping in mind that they are defined in the extended manifold, $x \in [-L, L]$, we accordingly introduce two chiral bosonic fields, $\phi_\pm(x)$, that are defined on $x \in [-L, L]$. The associated boundary conditions at $x = \pm L$ [Eq. 4.12] would then translate to the boundary conditions for the bosonic fields. In addition, introducing two Klein factors ($U_\pm$) and occupancy operators ($N_\pm$) for the chiral fermions the bosonized

expressions take the form

$$\gamma_{\pm}(x) = \frac{U_{\pm}}{\sqrt{2\pi\alpha}}\, e^{\pm iN_{\pm}\pi x/L}\, e^{i(\pi+\varphi)x/(2L)}\, e^{-i\phi_{\pm}(x)} \tag{4.15}$$

where $\phi_{\pm}(x)$ describes the long-wavelength density fluctuations of $\gamma_{\pm}(x)$ as in standard bosonization formalism. The phase factor $\exp[i(\pi+\varphi)x/(2L)]$ is intentionally included so that $\gamma_{\pm}$ satisfies the twisted boundary condition given by Eq. 4.12 even when the bosonic fields, $\phi_{\pm}$, can be chosen to be periodic at the two ends of the manifold, i.e., $\phi_{\pm}(-L) = \phi_{\pm}(L)$.

In order to find the constraints on the spin-charge bosonic fields, we relate the two sets of bosonized expressions [given by Eq. 4.14 and Eq. 4.15 respectively] according to Eq. 4.10. In Appendix A.1 we derive the relations between the Klein factors, number operators and the bosonic variables. To save space here we just list the results of that analysis:

$$\begin{aligned}
&U_{R\uparrow} = U_{+}\, e^{i(\pi+\varphi)\frac{x}{2L}} \quad U_{L\downarrow} = -ie^{i\varphi_0}\, U_{+}^{\dagger}\, e^{i(3\pi+\varphi)\frac{x}{2L}} \\
&U_{L\uparrow} = U_{-}\, e^{i(\pi+\varphi)\frac{x}{2L}} \quad U_{R\downarrow} = ie^{i\varphi_0}\, U_{-}^{\dagger}\, e^{i(3\pi+\varphi)\frac{x}{2L}} \\
&N_{R\uparrow} = N_{+} \quad N_{L\downarrow} = -N_{-} \\
&N_{L\uparrow} = N_{-} \quad N_{R\downarrow} = -N_{-}
\end{aligned} \tag{4.16}$$

The phase-factors that are multiplied with the Klein factors are mainly associated with the phase-differences induced by the Andreev reflections on the fermionic fields. The rest of the relations can be intuitively understood as follows. According to Eq. 4.10 since $\psi_{R/L,\uparrow} \propto \gamma_{\pm}$ and $\psi_{L/R,\downarrow} \propto \gamma_{\pm}^{\dagger}$, the Klein factors should also be related accordingly as, $U_{R/L,\uparrow} \propto U_{\pm}$ and $U_{L/R,\downarrow} \propto U_{\pm}^{\dagger}$. And considering the fact that creation of chiral fermion is associated with creation and annihilation of certain particle fields, the

corresponding number operators, $N_{R/L,\uparrow}$ should have the same sign as $N_{\pm}$ whereas $N_{L/R,\downarrow}$ have opposite sign to $N_{\pm}$.

Finally, the relations between the bosonic variables can be expressed separately on two halves of the extended manifold, i.e., $x \in [0, -L]$ and $x \in [0, L]$, as [Appendix A.1]

$$\begin{aligned} \phi_{\pm}(x) &= \pm\frac{1}{\sqrt{2}}\left[\phi_c \mp \theta_c + \phi_\sigma \mp \theta_\sigma\right](x), \\ \phi_{\pm}(-x) &= \pm\frac{1}{\sqrt{2}}\left[\phi_c \pm \theta_c - \phi_\sigma \mp \theta_\sigma\right](x), \end{aligned} \tag{4.17}$$

where $x \in [0, L]$. Following Eq. 4.17 the continuity conditions of $\phi_{\pm}(x)$ at $x = 0$ and $x = \pm L$ constrain the spin-charge bosons as [see Appendix A.1 for derivation]

$$\begin{aligned} \theta_c(0, L) &= 0 \\ \phi_\sigma(0, L) &= 0 \end{aligned} \tag{4.18}$$

The boundary constraints derived here would be useful in order to expand $\phi_{c,\sigma}$ and $\theta_{c,\sigma}$ in terms of second quantized operators while choosing the correct basis functions for the setup which we discuss now. As the bosonic fields contain the density fluctuations of the fermions the momentum spacing for the density modes will be same as the momentum spacing of the fermionic modes, hence, the density modes will be quantized as $k_n = n\pi/L$. For such values of k_n, $\sin(k_n x)$ vanishes at $x = 0, L$ and hence they should be the basis functions for θ_c and ϕ_σ to satisfy the boundary conditions given by Eq. 4.18. This leaves the modes in ϕ_c and θ_σ to be proportional to $\cos(k_n x)$ in order to satisfy commutation relations. Following these arguments we can write down the

expansions in terms of the second quantized operators as follows

$$\begin{aligned}
\phi_c &= \sqrt{\frac{\pi}{2L}} \sum_n \frac{sgn(k_n)}{\sqrt{|k_n|}} \cos(k_n x) \left[b_n + b_n^\dagger\right] \\
\theta_c &= i\sqrt{\frac{\pi}{2L}} \sum_n \frac{\sin(k_n x)}{\sqrt{|k_n|}} \left[b_n^\dagger - b_n\right] \\
\phi_\sigma &= i\sqrt{\frac{\pi}{2L}} \sum_n \frac{sgn(k_n)}{\sqrt{|k_n|}} \sin(k_n x) \left[b_n^\dagger - b_n\right] \\
\theta_\sigma &= \sqrt{\frac{\pi}{2L}} \sum_n \frac{\cos(k_n x)}{\sqrt{|k_n|}} \left[b_n + b_n^\dagger\right]
\end{aligned} \tag{4.19}$$

where b_n, $b_n^\dagger$ are bosonic annihilation and creation operators satisfying the standard commutation relation, $\left[b_n, b_{n'}^\dagger\right] = \delta_{n,n'}$. It can be explicitly verified following the expansions given above that the charge and spin density and phase bosons satisfy the standard commutation relations given by $[\phi_{c,\sigma}, \partial_x \theta_{c,\sigma}] = i\pi\delta(x - x')$.

Now using these second quantized forms we proceed to find the diagonal basis for the interacting problem. The local density-density interactions in terms of the charge and spin densities are given as $\int dx[g_c\, \rho_c^2(x) + g_\sigma\, \rho_\sigma^2(x)]$ where g_c and g_σ are the corresponding interaction strengths. The resultant interacting Hamiltonian, in terms of spin and charge bosonic variables, can be written as [14]

$$\hat{H}_{\text{int}} = \frac{1}{2\pi} \sum_{\nu=c,\sigma} \int_0^L dx\, u_\nu \left[\frac{(\partial_x \phi_\nu)^2}{K_\nu} + K_\nu \left(\partial_x \theta_\nu\right)^2\right] \tag{4.20}$$

where the charge and spin velocities $u_{c,\sigma}$ and interaction parameters $K_{c,\sigma}$ are re-normalized by the interaction strengths as [14]

$$\begin{aligned}
u_{c,\sigma} &= v_F \sqrt{1 + 2g_{c,\sigma}/(\pi v_F)} \\
\frac{1}{K_{c,\sigma}} &= \sqrt{1 + 2g_{c,\sigma}/(\pi v_F)}
\end{aligned} \tag{4.21}$$

where $g_{c,\sigma}/(\pi v_F)$ corresponds to the strength of local density-density interaction for charge and spin density respectively.

In order to solve the interacting Hamiltonian we substitute Eq. 4.19 for the fields, $\phi_{c,\sigma}$ and $\theta_{c,\sigma}$, in Eq. 4.20. The raw substitutions do not have the diagonalized form at the outset. However, a new set of bosonic operators can be defined as $\gamma_{c/\sigma,n}$ in terms of $b_n, b_n^\dagger$ such that the Hamiltonian becomes diagonal in that basis. The required transformations involve two steps of linear transformations for the second quantized operators, $\{b_n,\, b_n^\dagger\}$ which are described in Appendix A.2. In the diagonal basis $\hat{H}_{\text{int}}$ is given as:

$$\hat{H}_{\text{int}} = \sum_{n>0} \left[u_c k_n \, \gamma_{c,n}^\dagger \gamma_{c,n} + u_\sigma k_n \, \gamma_{\sigma,n}^\dagger \gamma_{\sigma,n} \right] \tag{4.22}$$

where the relations between $\{\gamma_{c,n},\, \gamma_{\sigma,n}\}$ and $\{b_n,\, b_n^\dagger\}$ are derived in Appendix A.2. The operators $\gamma_{c,n}$ and $\gamma_{\sigma,n}$ represent the charge and spin density wave with momentum $k_n = n\pi/L$ respectively. The corresponding energy of the modes are given by $u_c k_n$ and $u_\sigma k_n$ accordingly. The diagonal form of the interacting Hamiltonian in Eq. 4.22 reflects the well known fact that in a 1D interacting metal the eigen states are bosonic modes corresponding to charge and spin density wave excitations with linear dispersion characterized by their velocities, u_c and u_σ. Furthermore, the spin and charge modes are decoupled from each other which is known as the spin-charge separation. The velocities $u_{c,\sigma}$ are re-normalized by charge and spin interaction strengths separately as given by Eq. 4.21. Once the diagonal basis is obtained, computation of any correlator can be easily performed by expressing the involved operators in terms of these diagonal basis. Thus, with the interacting problem solved for the S-LL-S setup we now introduce impurity to the system in the next section and calculate the relevant correlator that describes the absorption spectrum.

4.3 Impurity induced absorption spectrum

In this section we study the effects of impurity induced back-scattering on the absorptive part of the linear response function. Since impurity is ubiquitous in any 1D system, to correctly compute any experimentally measurable response function one needs to take into account the role of that impurity while calculating the corresponding correlators. As we will see the impurity induced back-scattering terms would have significant effect of coupling the spin and charge degrees of freedom in the LL wire that are otherwise separated in a clean system. Consequently the spin modes are manifested in the charge conductivity spectrum.

In the next subsection (Sec. 4.3.1) we introduce the impurity potential that models non-magnetic charge impurities. Then we evaluate the absorptive part of the response function by treating the impurity potential perturbatively in the subsequent subsections (Sec. 4.3.2 and Sec. 4.3.3).

4.3.1 The impurity potential induced spin-charge coupling

The low energy contribution of impurity scatterings in 1D can be split into forward-scatterings involving small momentum transfers compared to k_F and back-scatterings involving processes transferring large momentum of around $\pm 2k_F$. The forward-scattering contributions result in a spatial-dependent phase factor, which can be absorbed into the definition of back-scattering potential [14]. In other words, ignoring the forward-scattering contribution does not alter the results. Hence, we can effectively focus on the back-scattering terms induced by non-magnetic charge

impurities and model the corresponding Hamiltonian as

$$\delta\hat{H}_{\rm B} = \sum_{s=\uparrow,\downarrow}\int_0^L dx\ \left[g_{\rm B}(x)\, e^{-i2k_F x}\, \psi^\dagger_{\rm Rs}\psi_{\rm Ls} + h.c.\right] \tag{4.23}$$

where the back-scattering terms $\psi^\dagger_{Rs}\psi_{Ls}$ and $\psi^\dagger_{Ls}\psi_{Rs}$ change the direction of the particle motion by transferring momentum of $\pm 2k_F$. The potential $g_{\rm B}(x)$ which determines the spatial profile of the back-scattering terms can be chosen as a random function defined in the system that is characterised by its momentum space representation, $\tilde{g}_{\rm B}(k)$. We choose $\tilde{g}_{\rm B}(k)$ to be a Gaussian random complex number with a momentum dependent Gaussian weight given by

$$\tilde{g}_{\rm B}(k) = \delta g\, \exp\left[-\frac{(k\lambda)^2}{8}\right](X_k + iY_k) \tag{4.24}$$

where δg is proportional to the amplitude of the disorder potential and X_k and Y_k are two i.i.d. $N(0,1)$ random variables for each k. The parameter λ sets a momentum cutoff for the Gaussian weight. The real space correlation of $g_{\rm B}(x)$, given by $\overline{g^*_{\rm B}(x)g_{\rm B}(y)}$, can be obtained by expanding $g_{\rm B}(x)$ and $g_{\rm B}(y)$ in Fourier space with the amplitudes defined above. Using $\overline{X_k X_{k'}} = \overline{Y_k Y_{k'}} = \delta(k-k')$, it can be shown that the disorder potential has Gaussian correlation in real space given by

$$\overline{g^*_{\rm B}(x)g_{\rm B}(y)} = 4\sqrt{\pi}\frac{(\delta g)^2}{\lambda}\exp\left[-\frac{(x-y)^2}{\lambda^2}\right] \tag{4.25}$$

which indicates that λ can be interpreted as the correlation length of the disorder potential.

The back-scattering induced spin-charge coupling in $\delta\hat{H}_{\rm B}$ can be seen by expressing the terms, $\psi^\dagger_{Rs}\psi_{Ls}$ and $\psi^\dagger_{Ls}\psi_{Rs}$, in their corresponding spin and charge bosonic basis. Using the bosonized expressions for the fermions [Eq. 4.14] and utilizing the relations

given by Eq. 4.16 and Eq. 4.17, the back-scattering terms can be written as

$$\begin{aligned}
\psi^{\dagger}_{R\uparrow,\downarrow}\psi_{L\uparrow,\downarrow} &= \frac{1}{2\pi\alpha}U^{\dagger}_{+}U_{-}\, e^{\mp i(N_{+}+N_{-}+1)\pi x/L} \\
& e^{\frac{i}{\sqrt{2}}(\phi_c-\theta_c)} e^{\frac{i}{\sqrt{2}}(\phi_c+\theta_c)}\, e^{\pm\frac{i}{\sqrt{2}}(\phi_\sigma-\theta_\sigma)} e^{\pm\frac{i}{\sqrt{2}}(\phi_\sigma+\theta_\sigma)} \\
\psi^{\dagger}_{L\uparrow,\downarrow}\psi_{R\uparrow,\downarrow} &= \frac{1}{2\pi\alpha}U^{\dagger}_{-}U_{+}\, e^{\pm i(N_{+}+N_{-}+1)\pi x/L} \\
& e^{-\frac{i}{\sqrt{2}}(\phi_c+\theta_c)}\, e^{-\frac{i}{\sqrt{2}}(\phi_c-\theta_c)}\, e^{\mp\frac{i}{\sqrt{2}}(\phi_\sigma+\theta_\sigma)}\, e^{\mp\frac{i}{\sqrt{2}}(\phi_\sigma-\theta_\sigma)}
\end{aligned} \tag{4.26}$$

From these expressions it is clear that the back-scattering terms, being product of exponentials of charge and spin bosons, couple spin and charge. In the next subsection we show that this spin-charge coupling manifests itself in the optical absorption spectrum as peaks being present at energies corresponding to both charge and spin excitations.

4.3.2 Dissipative conductivity spectrum

In this subsection we calculate the absorption spectrum for the S-LL-S setup in presence of impurity as described above using linear response theory. Specifically we find the expression for the experimentally relevant dissipative part of the response function. We assume the weak disorder limit which is obtained when $\delta g/(\pi v_F) \ll 1$ so that we can treat the impurity Hamiltonian, $\delta\hat{H}_{\rm B}$, perturbatively.

The linear response function is given by the ground state expectation value of the commutator of charge current operators at two different times as

$$\chi(t,t') = -i\left\langle\left[\hat{J}_c(t),\hat{J}_c(t')\right]\right\rangle \tag{4.27}$$

where $\hat{J}_c(t)$ is the current operator in the Heisenberg picture. In the long wave length limit the corresponding time-independent operator can be expressed as the difference

between densities of the right moving and left moving modes as

$$\hat{J}_c = \frac{v_F}{\sqrt{2}L} \sum_{s=\uparrow,\downarrow} \int_0^L dx \, (\rho_{Rs} - \rho_{Ls}) = \frac{\sqrt{2}v_F}{L}(N_+ - N_-) \tag{4.28}$$

where $\hat{N}_\pm$ describes the occupancies of the chiral fermions as described in Sec. 4.2.3. Since $\hat{N}_\pm$ commute with all the bosonic creation annihilation operators ($\{\gamma_{c,n}, \gamma_{\sigma,n}\}$), $\hat{J}_c$ commutes with the Hamiltonian of the clean system, $\hat{H}_{\text{int}}$, as given by Eq. 4.22 and hence $[J_c(t), J_c(t')] = 0$. However, in presence of back-scattering the $U_\pm^\dagger U_\mp$ terms do not commute with $\hat{N}_\pm$ and hence the current operator does not commute with the impurity Hamiltonian. In that case, the response function, $\chi(t, t')$, is renormalized by the impurity Hamiltonian. As we derive in Appendix A.3, up to leading order in impurity strength, $\chi(t, t')$ is given by,

$$\chi(t, t') \approx -2 \sum_{m \neq GS} J_c^2(m) \frac{|\langle m|\delta\hat{H}_{\text{B}}|GS\rangle|^2}{E_m^2} \sin\left[E_m(t - t')\right] \tag{4.29}$$

where $\{|m\rangle\}$ is the set of unperturbed excited states of $\hat{H}_{\text{int}}$, E_m is the associated unperturbed energy eigenvalue and $J_c(m)$ is the matrix element of $\hat{J}_c$, i.e., $J_c(m) \equiv \langle m|\hat{J}_c|m\rangle$.

The experimentally relevant absorption spectrum is obtained from the imaginary part of the response function in frequency space which is given by $\sigma(\omega) = Im[\chi(\omega)]/\omega$. As derived in Appendix A.3 the spectrum has the form

$$Re[\sigma(\omega)] \approx \sum_E Z(E) \, \delta(\omega - E) \tag{4.30}$$

where $Z(E)$ is given by

$$Z(E) = \pi \sum_m J_c^2(m) \, \frac{|\langle m|\delta\hat{H}_{\text{B}}|GS\rangle|^2}{E_m^3} \delta_{E,E_m} \tag{4.31}$$

Thus, the absorption spectrum contains a series of delta-function peaks on the energy axis wherever the impurity potential couples the excited states with the ground state, i.e., $\omega = E_m$ such that $|\langle m|\delta\hat{H}_{\rm B}|GS\rangle| \neq 0$. Since the impurity induced back-scattering terms involve exponentials of both spin and charge bosons [as given in Eq. 4.26], it can be inferred that $\delta\hat{H}_{\rm B}$ can excite arbitrary bosonic excitations containing both spin and charge modes. Hence, we can conclude that the absorption peak strength, $Z(E)$, is non-zero at energies of both charge and spin mode excitations. More specifically the contribution to $Z(E)$ can be divided into three parts for convenience as $Z(E) = Z_c(E)+Z_\sigma(E)+Z_{\rm hyb}(E)$, which are i) due to the charge mode excitations only ($Z_c(E)$), ii) due to the spin mode excitations only ($Z_\sigma(E)$) and ii) from excitations containing both the charge and spin modes ($Z_{\rm hyb}(E)$).

In the next sub-section we discuss the relevant details required for the calculation of the matrix elements appearing in expression for $Z(E)$.

4.3.3 Calculation of the matrix elements

Here we describe the matrix element evaluation that determine the peak strengths, $Z(E)$, in the absorption spectrum. In the expression for $Z(E)$ the unperturbed eigen state, $|m\rangle$, in Fock space, can be represented by the occupancies of the chiral fermions, $\gamma_\pm$, and all the charge and spin bosonic modes, $\gamma_{c,n}$, $\gamma_{\sigma,n}$, as $|m\rangle = |n_+, n_-, \{p_n^c\}, \{p_n^\sigma\}\rangle$ where $n_\pm$ denotes the occupancy of the fermionic $\gamma_\pm$ modes and $p_n^{c,\sigma}$ denotes the occupancy of the charge/spin density mode with momentum k_n described by $\gamma_{c,n}^\dagger$ ($\gamma_{\sigma,n}^\dagger$). Hence, the terms in $\delta\hat{H}_{\rm B}$ needs to be expressed in terms of the diagonal

second quantized basis for the clean interacting system to calculate the required matrix elements.

Since the back-scattering terms in $\delta\hat{H}_{\rm B}$ are proportional to $U_{\pm}^{\dagger}U_{\mp}$ [as in Eq. 4.26], it either transfers a left mover to a right mover (by $U_{+}^{\dagger}U_{-}$) or vice-versa (by $U_{-}^{\dagger}U_{+}$). As a result the matrix element, $\langle m|\delta\hat{H}_{\rm B}|GS\rangle$, is non-zero only when $n_{+}=\pm1$ or $n_{-}=\pm1$. Thus, the matrix elements are non-zero when $|m\rangle$ is $|m_{\pm}\rangle = |\pm 1, \mp 1, \{p_n^c\}, \{p_n^\sigma\}\rangle$. In the expression for $Z(E)$ the matrix element of $\hat{J}_c$ only depends on the difference of the fermionic occupancies, i.e., $(n_{+}-n_{-})$, and thus, is given by $J_c(m_{\pm}) = (n_{+}-n_{-})\sqrt{2}v_F/L$.

In order to calculate the contribution from the bosonic modes to the matrix element, it is useful to express the operators appearing in $\delta\hat{H}_{\rm B}$ [Eq. 4.26] in the diagonal basis for the interacting system (i.e., in terms of $\{\gamma_{c,n},\, \gamma_{c,n}^{\dagger}\}$and $\{\gamma_{\sigma,n},\, \gamma_{\sigma,n}^{\dagger}\}$) and order them such that all creation operators ($\gamma_{c,n}^{\dagger}$ and $\gamma_{\sigma,n}^{\dagger}$) appear on the right. We perform this normal ordering using Baker-Campbell-Hausdorff (BCH) formula in Appendix A.4. Following the normal ordering the calculation of the contribution from the bosonic modes becomes trivial [Appendix A.4] and is given by,

$$\begin{aligned}
&\langle \pm1, \mp1, m_n^c = p_n^c, m_n^\sigma = p_n^\sigma| \sum_{s=\uparrow,\downarrow} \psi_{Rs}^{\dagger}\psi_{Ls}|GS\rangle \\
&= \frac{e^{-i\pi x/L}}{2\pi\alpha} F(x) \frac{(-i\cos(k_n x)\sqrt{2\pi K_c/n})^{p_n^c}}{\sqrt{p_n^c!}} \frac{(-\sin(k_n x)\sqrt{2\pi K_\sigma/n})^{p_n^\sigma}}{\sqrt{p_n^\sigma!}} \left[1 + e^{i2\frac{\pi x}{L}}(-1)^{p_n^\sigma}\right]
\end{aligned} \tag{4.32}$$

where the function, $F(x)$, has the following expression

$$F(x) = \exp\left[-\sum_{n>0}\frac{\pi}{n}\left[K_c\cos^2 k_n x + K_\sigma \sin^2 k_n x\right] e^{-\alpha k_n}\right] \tag{4.33}$$

where α is the same cut-off introduced in Eq. 4.14.

Using Eq. 4.32 each of the three parts of $Z(E)$ has the following expression

$$
\begin{aligned}
Z_c(E) &= \pi \sum_{p_n^\sigma=0} J_c^2(m_\pm)\, \frac{|\langle m_\pm|\delta\hat{H}_{\rm B}|GS\rangle|^2}{E_{m_\pm}^3}\, \delta_{E,E_{m_\pm}} \\
Z_\sigma(E) &= \pi \sum_{p_n^c=0} J_c^2(m_\pm)\, \frac{|\langle m_\pm|\delta\hat{H}_{\rm B}|GS\rangle|^2}{E_{m_\pm}^3}\, \delta_{E,E_{m_\pm}} \\
Z_{\rm hyb}(E) &= \pi \sum_{p_n^c,p_n^\sigma\neq 0} J_c^2(m_\pm)\, \frac{|\langle m_\pm|\delta\hat{H}_{\rm B}|GS\rangle|^2}{E_{m_\pm}^3}\, \delta_{E,E_{m_\pm}}
\end{aligned}
\tag{4.34}
$$

With these matrix element expressions [Eq. 4.32] we are now in a position to numerically calculate the peak strengths given by $Z_{c,\sigma,\rm hyb}$ after averaging over disorder potential realizations that is embedded in $\delta\hat{H}_{\rm B}$. We present the results from our numerical calculations and analyze them in the next section.

4.4 Numerical results and discussion

In this section we present the numerical results of $Z(E)$ and analyze the effects of impurity potential on the same. For the characteristics of interactions, we consider the simple case of local Coulomb repulsion between the electrons which corresponds to $g_c > 0$ and $g_\sigma = 0$ in the interacting Hamiltonian given by Eq. 4.20. It translates for the interaction parameters in $\hat{H}_{\rm int}$ to $K_c < 1$, $K_\sigma = 1$ and $u_c = v_F/\sqrt{K_c}$, $u_\sigma = v_F$ according to Eq. 4.21. Thus, in this regime tuning the interaction strength, g_c, the charge velocity can be tuned that controls the spacing of the charge excitation spectrum [as given by Eq. 4.22], but keeps the spectrum of the spin excitations intact.

Next we describe the comparison of the length scales relevant to our numerical evaluation. The four relevant length scales present in the system are: i) the length of the system, L, ii) inverse of Fermi momentum, k_F^{-1}, iii) the correlation length of the

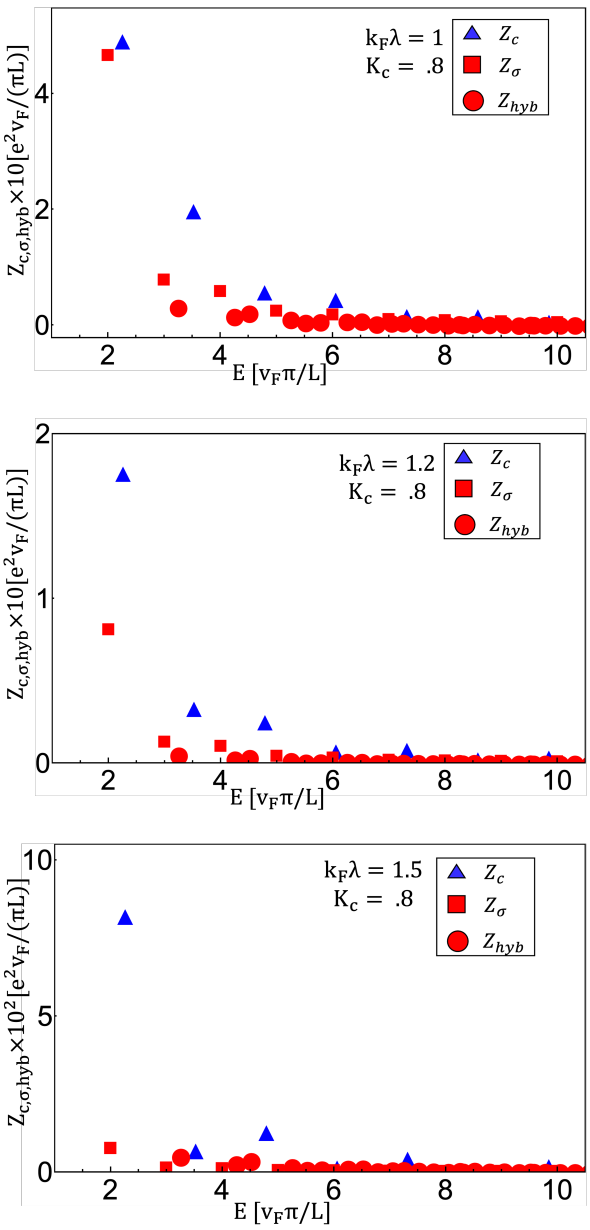

Figure 4.2: The peak strengths Z_c (triangles), Z_σ (squares) and $Z_{\rm hyb}$ (circles) are shown for $K_c = 0.6$ and for (a) $k_F\lambda = 1$, (b) $k_F\lambda = 1.2$, (c) $k_F\lambda = 1.5$. $Z_{c,\sigma,{\rm hyb}}$ are marked in units of $e^2v_F/(\pi L)$ and the energy axis is in units of $v_F\pi/L$. As $k_F\lambda$ increases significantly larger than one (from (a) to (c)), the spin peaks (Z_σ) get attenuated drastically compared to the charge peaks (Z_c) .

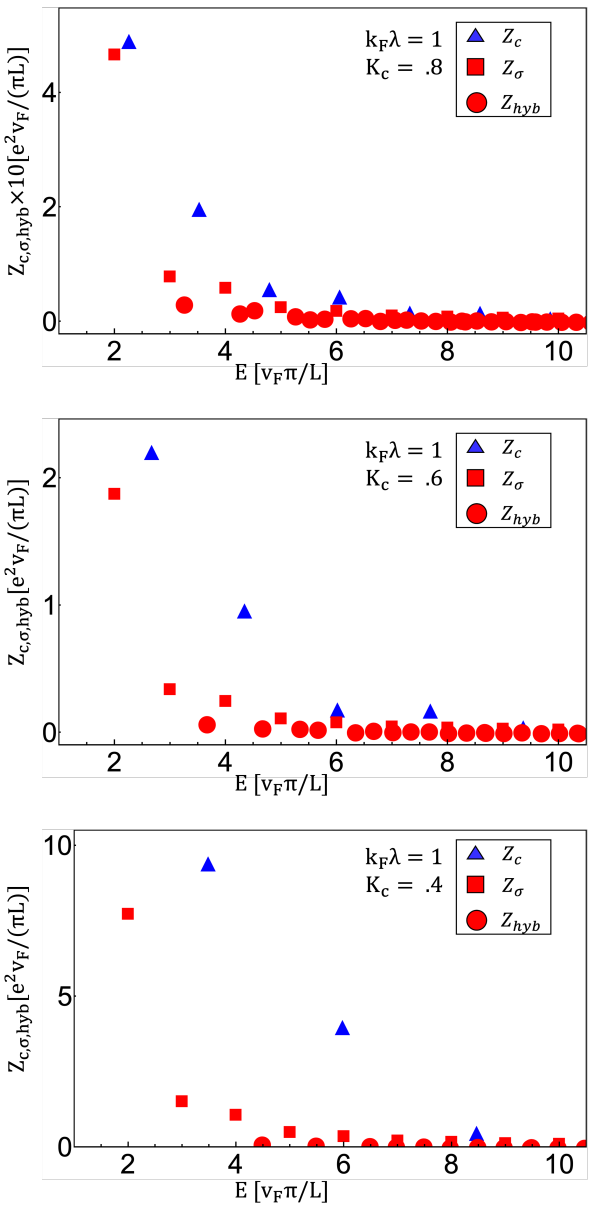

Figure 4.3: The peak strengths Z_c (filled triangles), Z_σ (filled squares) and $Z_{\rm hyb}$ (filled circles) are shown for $k_F\lambda = 1$ and for different values of the interaction strength, viz. (a) $K_c = .8$, (b) $K_c = .6$, (c) $K_c = .4$. From (a) to (c) the energy spacing between charge peaks, i.e. for the triangles and squares increase whereas the spin peaks (squares) remain at same positions.

disorder potential, λ, as it appears in Eq. 4.24 and iv) the cutoff parameter, α, for any momenta sum such as in Eq. 4.33. α^{-1}, being the cutoff momentum, is typically much larger than the momentum spacing of the bosonic spectrum, i.e. $\alpha^{-1} \gg \Delta k_n \sim L^{-1}$, but smaller than the Fermi momentum, $\alpha^{-1} < k_F$. Lastly, we choose the disorder correlation length, λ, to be of the order of k_F^{-1}.

A relevant point to consider while calculating $Z(E)$ is the degeneracy of higher energy excited states. Since a single particle bosonic mode can be multiply occupied and the energy of such excitation is integer multiples of $u_{c,\sigma}\pi/L$ [Eq. 4.22], the discrete excitation spectrum is in general degenerate. Hence, while calculating the peak strength at such a degenerate value of energy the contribution from all of those degenerate states have to be added in the sum for $Z(E)$ [Eq. 4.34].

In the parameter regime described above we vary the Fermi momentum, k_F, around $\lambda^{-1}$and for a fixed value of interaction strength and compare the resultant peak strengths.

4.4.1 Tuning the Fermi momentum

Choosing $L = 200\,\alpha$, $\lambda = 0.3\,\alpha$ and $K_c = 0.6$, we vary k_F to explore the regime when $k_F\lambda$ becomes larger than 1. The resultant peak strengths for $k_F\lambda = 2$, $k_F\lambda = 2.4$ and $k_F\lambda = 3.8$ are shown in Fig. 4.2 (a), (b) and (c) respectively. In each of these plots $Z_c(E)$, $Z_\sigma(E)$ and $Z_{\rm hyb}(E)$ are marked in units of $e^2 v_F/(\pi L)$ by blue triangles, red squares and red circles respectively. The energy axes are marked in units of $v_F/(\pi L)$. As can be seen in Figs. 4.2, with increasing value of k_F (from (a) to (c)), all the

peak strengths are generically reduced. This is expected as according to Eq. 4.24 $\tilde{g}_{\rm B}(k) \propto \exp[-(k\lambda)^2/8]$ with increasing value of k_F, the Gaussian weight at $k = \pm 2k_F$, $\tilde{g}_B(\pm 2k_F)$, reduces exponentially. Since the back-scattering terms are proportional to $e^{\pm i 2k_F x}$, the effective contribution of the back-scattering terms in $\delta\hat{H}_{\rm B}$ [Eq. 4.23] also falls off exponentially. More notably, the contributions from the states that include spin modes, i.e., Z_σ and $Z_{\rm hyb}$, are more drastically attenuated compared to the contributions from the charge modes, Z_c as λk_F goes becomes larger. This result indicates that in an experimental setup the spin peaks would be most prominent and about as strong as the charge peaks when k_F is tuned to have $\lambda k_F \lesssim 2$ which sets a suggested regime for probing the spin modes.

4.4.2 Tuning the Coulomb interaction strength

Next, choosing the fixed value for k_F such that $\lambda k_F = 2$ we vary the interaction strength as $K_c \in \{.4, .6, .8\}$ and study the evolution of the peaks on the energy axis. The resultant peak strengths are presented in Figs. 4.3 (a)-(c). With increasing interaction strength, i.e. decreasing value of K_c (from (a) to (c)), the energy spacing between consecutive peaks containing charge modes, i.e. for Z_c and $Z_{\rm hyb}$, increase as $u_c \propto v_F/\sqrt{K_c}$. However, since the spin velocity, u_σ is insensitive to the Coulomb interaction strength, the spacing between the spin peaks in Z_σ remains fixed. Thus, tuning the interaction strengths in an experiment can facilitate identification of the spin peak locations and their corresponding energy gap.

4.5 Summary and Conclusion

In summary, we have studied the effects of the impurity induced back-scattering process in the optical absorption spectrum. We find that the back-scattering induced spin charge coupling provides a way to probe the spin modes in an experimental system. As discussed since the spin modes are trapped inside the normal region within an S-LL-S setup, the conductivity spectrum for a clean system does not contain any information about the spin modes making them undetectable in a transport measurement. Introduction of back-scattering processes, however, couples the spin and charge modes and we find that the signatures of such spin-charge coupling appear as peaks in the conductivity spectrum at the excitation energies associated with the spin modes.

While treating the non-interacting problem in an S-LL-S setup we introduced a new approach of interpreting the ABS modes in terms of the chiral Fermions that can be represented in a loop-like manifold that spans twice the length of the system as described in Sec. 4.2.2 and schematically shown in Fig. 4.1. These chiral fermions also provide a natural way to derive the special boundary conditions that connect the particle and hole fields owing to the perfect Andreev reflections at the NS interfaces. After introduction of the interacting Hamiltonian in Sec. 4.2.3 we diagonalized it in terms of second quantized bosonic operators associated with the charge and spin density excitations. Following that we discussed how the back-scattering terms induced by impurity possesses products of those charge and spin modes (Sec.4.3.1) and showed that the corresponding coupling shows up in the absorptive part of the response function in leading order in the perturbative impurity potential (Sec. 4.3.2).

Considering the case of Coulomb repulsion we numerically evaluated the optical absorption amplitudes (Sec. 4.4) and showed that for a given disorder potential length-scale, λ, which is typically not a tunable parameter in a system, the density can be tuned to effectively reach a regime where the Fermi momentum, k_F, is of the order of λ^{-1} where the spin peak intensities in the absorption spectrum becomes comparable to the charge peak intensities. The Coulomb repulsion strength may be varied by gating such that the charge gap can be varied and the spin peaks, being fixed throughout the process, can be identified in the absorption spectrum.

Chapter 5

Non-equilibrium nature of non-linear optical response: Application to the bulk photo voltaic effect

5.1 Introduction

In this chapter we go beyond the regime of linear response as considered in the EM response of the S-LL-S setup in the previous chapter 4 and focus on non-linear responses. We study the non-equilibrium nature of second order response by considering the example of the bulk photovoltaic effect (BPVE) that occurs in a non-centrosymmetric material. The results presented are based on a published paper [16].

In Equilibrium many-body-physics the fluctuation-dissipation theorem connects the linear response of a system to an external perturbation with the fluctuations of the system. The linear response is proportional to the external field with a coefficient associated with Equilibrium two-point correlator often known as the response function that characterizes the system. Such two-point correlators can be represented using the well-known Feynman diagrams for the case of interacting system.

The scenario is different when one considers non-linear responses in general. The second-order response to an applied field is in general non-equilibrium in nature. Specifically, the response function associated with the non-linear response includes three-point correlator that are out-of-time ordered. In particular, the three time

indices that appear in the correlator (derived in details in Appendix B.1) are neither monotonically increasing nor decreasing. Because of their non-equilibrium nature manifested by out-of-time-ordered operators, the usual Feynman diagrammatic technique is not capable to represent such correlators for an interacting system. Instead, Keldysh diagrams are required to represent those correlators.

In this chapter we would focus on the non-equilibrium nature of the non-linear response using the bulk photovoltaic effect (BPVE) as the example of a non-linear phenomenon. The BPVE is a second-order optical response of a non-centrosymmetric semiconductor where a DC current is observed throughout the bulk when an external oscillating electric field is applied upon it. The frequency of the electric field drives inter-band transitions in the material generating electron-hole pairs. Due to the absence of inversion symmetry in the system the charge centers of electron and hole do not coincide providing a preferred direction for the electric polarization which gives rise to a DC current in a periodic system. We study this phenomenon systematically both in the semi classical and quantum limit for a minimally interacting system where the electrons are coupled to phonons. In the semi classical limit the electron-phonon coupling is much stronger than the stimulating electric field amplitude so that after each electron-phonon scattering the electrons lose coherence acquired in the quantum part of its dynamics. In the quantum limit we treat the effects of the electron-phonon coupling using the Floquet Master equation approach.

5.1.1 Brief discussion of non-linear optical phenomena

In past few decades there have been several discoveries of non-linear phenomena in solid state systems. Such phenomena can be used to characterize solid state materials. In addition, their potential applications also make them exciting. For instance, BPVE provides a way to couple irradiated light to generate electricity that is proportional to the bulk volume of the system. Contrary to the conventional solar-cell systems that rely on the junction interface area as the irradiation cross-section, BPVE in principle is a platform for converting light in a much more efficient way. Furthermore, it has been shown that hidden inversion symmetry breaking nematic phase can be detected using certain second harmonic generation coefficients [49]. Similarly, second harmonic generation has been associated with inversion symmetry breaking in certain topological materials with hexagonal warping term and a gap for quasiparticle excitations [50, 51]. In a Weyl material circularly polarized light can induce non-linear DC current response that is known as the circular photogalvanic effect (CPGE). Such response are quantized and such quantization has directly been associated to the topological monopole charge of Weyl materials [52].

5.1.2 The bulk photo-voltaic effect (BPVE)

The bulk photovoltaic effect (BPVE) was discovered experimentally where a large voltage was seen in optically illuminated semiconductors. The origin of such a voltage was attributed to a large number of potential sources such as inversion asymmetry in impurity scattering, phonon-scattering and electron-electron interactions [53, 54, 55,

56, 57, 58]. In bulk non-centrosymmetric materials the BVPE for linearly polarized light has been argued to be a result of shift current [59] where an optically generated electron-hole pair's charge centers are shifted with respect to each other giving rise to a steady rate of polarization that appears as current. In this case the shift current can be thought of as a sequential tunneling of electrons to a certain direction within the bulk material.

Theoretically, using a non-linear response formalism, the BPVE has been shown to arise intrinsically in single crystalline materials that break inversion symmetry [60]. The corresponding magnitude of the SC response is directly related to the Berry curvature over parts of Brillouin zone where the optical illumination is resonant [61, 60]. Aside from fundamental interest as a probe of Berry curvature, the BPVE naturally has potential applications in converting light to electricity in a similar spirit to solar cell devices but with possibly higher efficiency provided appropriate materials can be found [62, 63, 64, 65, 66, 67, 44, 68, 69, 70].

The connection of the non-linear optical responses to the symmetries of the systems and topology of certain materials are enlightening. However, the understanding of such responses such as BPVE is somewhat limited outside the purview of non-interacting systems. As discussed earlier the response function formalism dictates that non-linear optical response contains out-of-time-ordered correlator in their response function. Such out-of-time-ordered correlators have been shown to appear first in non-linear response of superconductors [17]. Such correlators can not be calculated using conventional Feynman diagram techniques and in this sense are truly non-equilibrium in nature.

To show the inadequacy of the Feynman technique, one might consider the process of annihilation of photon and its conversion to electrical energy. However, in the equilibrium diagram formalism, each power of the vector-potential $A(t)$ is associated with either the absorption or emission of a photon. In that case, the creation of a DC current at second order in a vector potential must be interpreted as the sequential absorption and emission of a photon. Within this picture, net generation of electrical energy that drives the current appears quite paradoxical. An electrical current can only generate electrical energy in the presence of a finite voltage that can arise in the presence of a scattering process, which is ignored in the non-linear response theory for shift currents [59, 60, 61]. While scattering processes play a crucial role in certain extrinsic mechanisms for the BPVE [54, 53], the non-linear response mechanism is typically considered to ignore such scattering processes [59, 60, 61]. Thus, it is desirable to extend the non-linear response formalism for the BVPE to include such scattering processes in a way that is completely consistent with energy conservation.

5.1.3 Brief outline of the chapter

We assume that the electron-phonon interaction is symmetric so as to not directly contribute to the shift current. In Sec. 5.2, we develop the response function formalism for the BPVE. From the derivation we point out the role of out of time-ordered correlators (OTOC) [17]. The OTOC relevant to this work,, however involves three operators and is not connected to the well known Lyapunov exponents as is the case with the OTOC in Ref. [17]. Nevertheless, the presence of such correlators invalidates

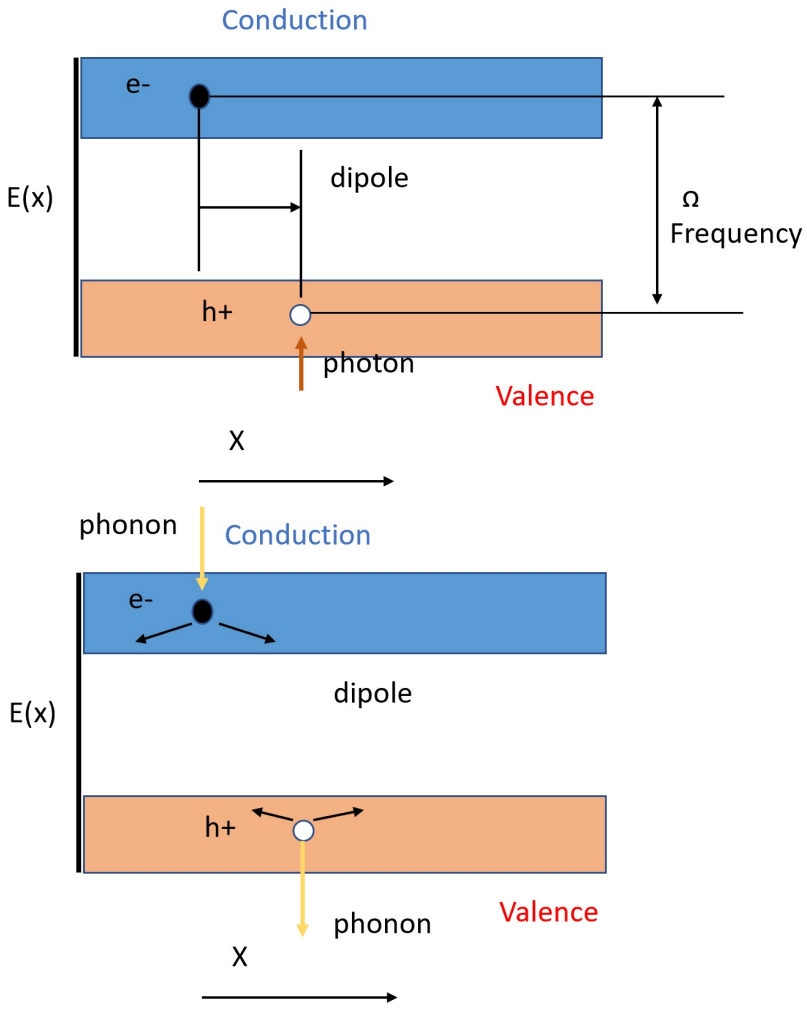

Figure 5.1: Two step process determining DC response: (a)Photon creates e-h pair density with their charge centers separated, generating dipole moment. (b)Scattering with phonons terminates charge shifting for that e-h pair.

the standard computation using equilibrium Feynman diagrams. In order to gain intuition for such non-equilibrium process, we first develop a semi classical picture of the BPVE (Sec. 5.3) based on the processes shown in Fig. 5.1. This picture is shown to lead to the conventional expression for the DC current in the case of homogeneous optical excitation. However, for a finite size system the application of inhomogeneous

excitation profiles are found to lead to results that can not be described by equilibrium response functions. The limitation of such semi classical treatment is that it is justified only when the electron-phonon scattering strength is much stronger than the optical excitation. We go beyond this limit in Sec. 5.4 using a Floquet Master equation approach. We find that this approach, in addition to reproducing the known small vector potential limit of the DC response also predicts a linearly scaling DC response in the quantum limit of small electron-phonon scattering strength. Finally, in Sec. 5.5, we study the cross-over between the small and large vector potential limit by computing the response numerically within the same formalism for a simple non-centrosymmetric Rice-Mele model [71].

5.2 Second order optical response

Let us start with the generic form of perturbative electromagnetic vector potential coupled to the system Hamiltonian by means of minimal coupling, given by: To build the response formalism let us consider a generic Hamiltonian describing a two band semiconductor that is coupled to electromagnetic (EM) field. Such a Hamiltonian is given by

$$\hat{H}(t) = \hat{H}_0 + \int dx\, A(r)\, \hat{J}(r) \tag{5.1}$$

where $\hat{H}_0$ is the system Hamiltonian and r is used to denote both the space-time co-ordinates, i.e., $r = (x, t)$. $\hat{J}(r)$ is the current operator which is the coupling to the monochromatic EM vector potential, $A(r)$. The vector potential has the form, $A(r) = A_0(x)\, e^{\eta t} \left(e^{\iota\Omega t} + e^{-\iota\Omega t}\right) \equiv A_0(x)\, e^{\eta t}\alpha(t)$, where $\eta = 0_+$ is the rate at which the

EM field is turned on.

In general one can expand $\hat{J}(r)$ in powers of A up to first order as: $\hat{J}(r) \approx \hat{J}_0(r) + A(r)\hat{J}_1(r)$. Using that expansion the response $\langle \hat{J}(r) \rangle$, up to second order in $A_0(x)$, can be written as (see Appendix B.1)

$$\begin{aligned}\langle \hat{J}(r) \rangle \approx \langle \hat{J}(r) \rangle_0 &+ \int_{-\infty}^{\infty} dx'\, A_0(x')\, \chi_{\text{lin}}(r, x') \\ &+ \int_{-\infty}^{\infty} dx'\, A_0^2(x')\, \chi_{n,2}(r, x') \\ &+ \int_{-\infty}^{\infty} dx_1 dx_2\, A_0(x_1) A_0(x_2)\, \chi_{n,3}(r, x_1, x_2) \\ &+ \int_{-\infty}^{\infty} dx_1\, dx_2\, A_0(x_1) A_0(x_2)\, \chi_{\text{otoc}}(r, x_1, x_2)\end{aligned} \tag{5.2}$$

where χ_{lin} is the linear response function given by

$$\chi_{\text{lin}}(r, x') = i \int_{-\infty}^{t} dt'\, e^{\eta t'} \alpha(t') \, \langle [\mathcal{J}_0(r'), \mathcal{J}_0(r)] \rangle_0 \tag{5.3}$$

In this equation the current operators are transformed to the interaction picture defined as $\mathcal{J}_{0,1}(r) \equiv e^{\iota \hat{H}_0 t} \hat{J}_{0,1}(r) e^{-\iota \hat{H}_0 t}$. There are three non-linear terms in the response. Among them $\chi_{n,2}$ can be viewed as a linear response of the current to a perturbation $A_0(r)\, \hat{J}_1(r)$ and is given by:

$$\chi_{n,2}(r, x') = i \int_{-\infty}^{t} dt'\, e^{2\eta t'} \alpha^2(t') \, \langle [\mathcal{J}_1(r'), \mathcal{J}_0(r)] \rangle_0 \tag{5.4}$$

The part of the non-linear response that contains $\chi_{n,3}$. $\chi_{n,3}$ is non-linear and involves three current operators. Its expression contains a time-ordered product and is given by

$$\begin{aligned}&\chi_{n,3}(r, x_1, x_2) \\ &= -\frac{1}{2} \int_{-\infty}^{t} dt_1\, dt_2 e^{\eta(t_1 + t_2)}\, \alpha(t_1)\alpha(t_2)\, \langle \{ \mathcal{T}\{\mathcal{J}_0(r_1)\mathcal{J}_0(r_2)\}, \mathcal{J}_0(r) \} \rangle_0\end{aligned} \tag{5.5}$$

Lastly, χ_{otoc} involves out of time ordered correlator of three current operators which is given by

$$\chi_{\text{otoc}}(r, x_1, x_2) = \int_{-\infty}^{t} dt_1\, dt_2\, e^{\eta(t_1+t_2)}\, \alpha(t_1)\alpha(t_2)\, \left\langle \tilde{\mathcal{J}}_0(r_1)\tilde{\mathcal{J}}_0(r)\tilde{\mathcal{J}}_0(r_2) \right\rangle_0 \tag{5.6}$$

In the integral expression of χ_{otoc}, the integral manifold contains region such that $t > t_1, t_2$ or $t_1, t_2 > t$. In a generic interacting system since the current operators at different times don't commute, calculating such correlators become non-trivial In these expressions, $\langle .. \rangle_0$ means expectation value w.r.t. the ground state of the system. As mentioned earlier, Feynman diagrams cannot be used to evaluate the correlators in χ_{otoc} and one requires the non-equilibrium generalization known as the Keldysh formalism [17].

Another way to see the problem with the equilibrium formalism is to quantize the EM field in terms of photons. Expanding $A(t) = a^\dagger e^{i\omega t} + h.c$ and substituting, A(t) into Eq. 5.2, it is easy to see that $\langle \hat{J}(r) \rangle_{\text{DC}} \propto \langle aa^\dagger \rangle$, which represents absorption followed by emission of a photon which suggests that no net energy is absorbed, even though the DC current in the presence of a voltage would do work. This would likely represent a non-equilibrium situation suggesting the need for a non-equilibrium theory. Consequences of this somewhat imprecise argument will become clear from the semi classical treatment of the DC current in the next section.

5.3 Semi classical description

In order to understand the absorption of energy more clearly, we consider a semiconducting two band Hamiltonian and include an explicit dissipation process

through phonon scattering within a semi classical approach. Along with the quantum mechanical evolution of the electronic state due to the applied EM field, the electron-phonon scatterings can be considered as probabilistic events in a semi classical approach.

A simple two band Hamiltonian for a semiconductor is given by

$$\hat{H}_0 = \sum_k \Delta_k \left(c_k^\dagger c_k - v_k^\dagger v_k \right) \tag{5.7}$$

where $c_k(v_k)$ is conduction (valence) band state operator and $2\Delta_k$ is the momentum dependent band gap. Now we describe the shift current generation process when the entire sample is illuminated.

5.3.1 Shift current in homogeneous excitation

The incident EM radiation creates electron-hole (e-h) pairs in the vicinity of the momentum space where the band gap is same as the incident frequency. The time dependent amplitude of such a pair can be extracted by treating the EM coupling in Eq. 5.1 perturbatively. The perturbation in the electronic wave function w.r.t. the ground state up to first order in A is given as

$$\begin{aligned} |\delta\Psi_k(t)\rangle_{\mathrm{I}} &\approx A_0 \left(J^x_{0,k} - iJ^y_{0,k}\right) \frac{\sin\left(\frac{\Omega}{2} - \Delta_k\right) t}{\left(\frac{\Omega}{2} - \Delta_k\right)} |e\bar{h}_k\rangle_I \\ &\equiv A_0 \left|J^\perp_{0,k}\right| e^{i\phi_k} \frac{\sin\left(\frac{\Omega}{2} - \Delta_k\right) t}{\left(\frac{\Omega}{2} - \Delta_k\right)} |e\bar{h}_k\rangle_I \end{aligned} \tag{5.8}$$

where $|0\rangle$ is the ground state of the system. $|e\bar{h}_k\rangle \equiv c_k^\dagger v_k |0\rangle$ is an e-h pair excitation with momentum k. $\vec{J}_0 \cdot \vec{\sigma} \equiv \hat{J}_0 = \partial_A \hat{H(t)}|_{A=0}$ such that $\vec{\sigma}$ is the vector of Pauli matrices in the band basis such that $\sigma^z|c_k\rangle = |c_k\rangle$, $\sigma^z|v_k\rangle = -|v_k\rangle$, $|J^\perp_{0,k}| \equiv \sqrt{(J^x_{0,k})^2 + (J^y_{0,k})^2}$.

In non-centrosymmetric materials, the charge centers of the excited e-h pair are located apart from each other generating a dipole moment. The time dependence of

such EM field generated dipole moment is given by:

$$\begin{aligned} P(t) &\equiv \sum_k \langle \delta\Psi_k(t)| \left(r_e - r_h\right) |\delta\Psi_k(t)\rangle \\ &= \sum_k \langle \delta\Psi_k(t)| \left(-i\partial_k\right) |\delta\Psi_k(t)\rangle \\ &= \frac{A_0^2}{2\pi} \int_{BZ} dk \, \frac{\sin^2\left(\frac{\Omega}{2} - \Delta_k\right) t}{\left(\frac{\Omega}{2} - \Delta_k\right)^2} \left(\vec{J}_{0,k} \times \vec{J}_{1,k}\right)_z \end{aligned} \tag{5.9}$$

where we have used the expression for $|\delta\Psi_k(t)\rangle$ from Eq. 5.8 to obtain the last line and defined $\vec{J}_{1,k} \equiv -\partial_k \vec{J}_{0,k}$.

This scenario described above applies to a purely non-interacting two band case. In presence of electron-phonon coupling the coherent evolution under the electric field is interrupted by phonon scatterings. In our semi classical approach such scatterings can be modeled as Poisson processes. The scattering event time t corresponding to the Poisson process is generically expressed by an exponential distribution function as

$$f(t) \equiv \eta \, e^{-\eta t} \tag{5.10}$$

where η is the total rate for electron and hole scatterings as detailed in the later part of this subsection.

In the weak electric field limit, once the scattering happens the e-h pair disperses equally in either direction and no further dipole moment is generated. In other words the coherence evolution that generates the e-h pair can be weighted by the probability distribution, $f(t)$ and the average polarization can be obtained. Thus, integrating the quantum dipole moment in Eq. 5.9 with $f(t)$ leads one has,

$$\langle P \rangle \equiv \int_0^\infty dt P(t) f(t) = \frac{A_0^2}{\pi} \int_{BZ} dk \, \frac{\left(\vec{J}_{0,k} \times \vec{J}_{1,k}\right)_z}{\eta^2 + \left(\Omega - 2\Delta_k\right)^2}. \tag{5.11}$$

The DC current can be determined by the average rate of dipole moment generation over the characteristic scattering time, $\tau \equiv \frac{1}{\eta}$. Using this relation we obtain the expression for the shift current to be

$$J^{\mathrm{DC}}_{\mathrm{shift}} = \frac{\langle P \rangle}{\tau} = \frac{A_0^2}{\pi} \int_{BZ} dk \, \frac{\eta}{(\Omega - 2\Delta_k)^2 + \eta^2} \left(\vec{J}_{0,k} \times \vec{J}_{1,k} \right)_z . \tag{5.12}$$

We note that η in our model is the electron-phonon scattering rate. In general for other kinds of interactions, η would equivalently be an energy scale associated with the decoherence mechanism of the e-h pairs. Considering the limit of $\lim_{\eta \to 0} \frac{\eta}{(\Omega - 2\Delta_k)^2 + \eta^2} = \pi \delta(\Omega - 2\Delta_k)$ in Eq. 5.12 we obtain

$$\lim_{\eta \to 0} J^{\mathrm{DC}}_{\mathrm{shift}} = A_0^2 \int_{BZ} dk \, \left(\vec{J}_{0,k} \times \vec{J}_{1,k} \right)_z \delta(\Omega - 2\Delta_k) \tag{5.13}$$

which is equivalent to the known expression for shift current given in [52] (see Appendix B.2).

The semi classical approach presented above, is valid in the limit of strong e-ph coupling or weak electric field ($A_0 |J^{\perp}_{0,k}| \ll \eta$) where the scattering processes are instantaneous events and can be modeled as rare Poisson processes with time scale, τ which is much smaller than the excitation rate, i.e., $\tau \ll \frac{1}{A_0 |J^{\perp}_{0,k}|}$. In Sec. 5.4 we will use a more quantum mechanical approach to study the case of longer scattering times τ.

The non-zero DC current in the mechanism of the BPVE described above relies on the lattice breaking inversion symmetry along the direction of current flow and consequently the excited e-h pairs carrying non-zero dipole moment. In centrosymmetric materials since there is no special direction for the dipole moment to build up due to the inversion symmetry of the lattice, optically excited e-h pairs cannot generate any DC

current. In conventional solar cells based on centrosymmetric materials such as silicon, the photo-excited electrons and holes are created in a thin region (depletion region) around the junction of two oppositely doped (p and n type) layers of semiconductor. The bias voltage at the depletion region drives the e-h pairs to generate a DC current across the junction. Thus, in this case, the generation of DC current happens only at the p-n junction due to presence of a bias voltage.

Let us now discuss the electron-phonon scattering processes that we consider here. Such scattering occurs following the generation of coherent exciton due to the applied EM field as discussed above. For simplicity we assume that the phonon scattering is momentum independent and hence the momenta and velocities of the electrons and holes are uncorrelated. Thus, the motion of the electrons and holes are diffusive starting from their average position. We consider the case where the electron and holes recombined and emit phonons such that the recombination takes place spatially locally. Such locality of the recombination process implies that the e-ph scattering doesn't generate any further dipole moment. Local recombination can happen when electron from an exciton-pair recombines with hole from another exciton-pair that was generated during excitation part of the process. As a result the dipole moments from those two pairs add up and effectively charge shifts along the same direction. This is the notion of a shift current. In general, however, non-local recombination would generate non-zero dipole moment which would either add up to or destroy some of the exciton generated dipole moment. Such contributions to the DC response have been addressed in Refs. [53, 54, 55]. For our discussions here, we ignore such contributions to the photocurrent. Thus, the shift current in our discussion is entirely due to an

average rate of dipole moment generation by the photo-excited e-h pairs.

As can be seen in Eq. 5.8 and Eq. 5.9, the dominant contribution to the dipole moment is from the momentum region of the two bands where the photo-excitation is resonant. Even in case of multiple bands, the dominant contribution to the DC current, up to second order in A_0, will be from the valence band and one excited band such that the corresponding gap matches the frequency of the applied EM field, Ω. Hence, as long as the electron hole recombination process via phonon scattering is spatially local, which is the case we consider here, the shift current generation mechanism is the same in presence of resonance between multiple bands. Off-resonant contributions, however, can be present and involve 3 band terms such as those considered in Ref. [72, 59] which we ignore here. Thus, our formalism makes it manifest that the DC part only depends on two bands even with electron-phonon interactions.

5.3.2 Diffusion current response for inhomogeneous excitations

Let us now consider a scenario where the illumination on the sample is inhomogeneous which would be the case in realistic setup or a finite size sample. The schematic is pictorially represented in Fig. 5.2 where we assume that the optical excitation intensity is non-zero only over a finite region R and vanishes outside.

For inhomogeneous excitation the second order shift current would also be spatially dependent, $J^{\rm DC}_{\rm shift} = \alpha A_0^2(x)$, where $A_0(x)$ varies in space. This combined with the conservation of charge leads to an inhomogeneous charge density. The gradient in charge leads to a diffusion current $J^d = -D\partial_x \rho$. The diffusivity of charge is given by

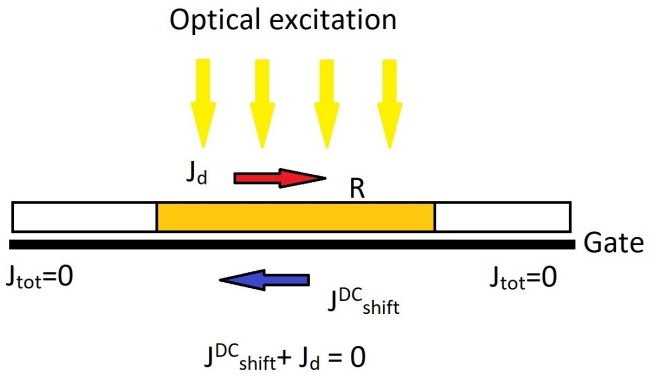

Figure 5.2: In the optically excited region, R, shift current, $J^{\mathrm{DC}}_{\mathrm{shift}}$, is countered by the diffusion current, J^d, so that the total current is divergence-less in the steady state. A gate in proximity can be used to measure the charge density profile capacitively and hence the shift current in steady state.

$D = \sigma/\chi$ where σ and χ are the conductivity and compressibility of the unperturbed carriers. The resultant density profile is determined from the continuity equation for the charge density given by

$$\partial_t \rho(x,t) = -\partial_x (J^d + J^{\mathrm{DC}}_{\mathrm{shift}}) \tag{5.14}$$

Substituting the form for the diffusion current transforms this equation into a diffusion equation with a source term given by

$$\partial_t \rho = D\partial_x^2 \rho + f(x) \tag{5.15}$$

where the source term, $f(x)$, is given by the gradient of shift current and has the form:

$$f(x) = -\partial_x J^{\mathrm{DC}}_{\mathrm{shift}} = 2\alpha A_0(x)\partial_x A_0(x) \tag{5.16}$$

Since there is no charge density initially (i.e. $\rho(x,0) = 0$), the solution of Eq. 5.15 is given by

$$\rho(x,t) = \int_{-\infty}^{\infty} dx'\, f(x') \int_0^t d\tau\, \frac{e^{-\frac{(x-x')^2}{4D\tau}}}{\sqrt{4\pi D\tau}} \tag{5.17}$$

The diffusion current can be obtained by differentiating the solution in Eq. 5.17 w.r.t. x to be

$$J^d(x) = \int_{-\infty}^{\infty} dx'\, f(x')\, \frac{(x-x')}{4\sqrt{\pi D}} \int_0^t d\tau\, \tau^{-\frac{3}{2}} e^{-\frac{(x-x')^2}{4D\tau}} \tag{5.18}$$

Performing a change of variable, $p = \frac{|x-x'|}{2\sqrt{D\tau}}$, the limits for p becomes ∞ and $\frac{|x-x'|}{2\sqrt{Dt}}$ respectively. In the long time limit set by the illumination length and diffusion coefficient($t \gg \frac{|x-x'|^2}{D}$), we can approximate the lower limit to be zero $\frac{|x-x'|}{2\sqrt{Dt}} \to 0$. In this long time limit, performing the Gaussian integral we obtain the expression for the diffusion current to be

$$J^d(x) = \frac{1}{2} \int_{-\infty}^{\infty} dx'\, f(x')\, sgn(x-x') \tag{5.19}$$

Substituting Eq. 5.16 in Eq. 5.19 and integrating by parts we obtain $J^d(x) = -J^{\text{DC}}_{\text{shift}}(x)$, i.e. the diffusion current cancels the shift current in steady state. The intuitive explanation for this mutual cancellation in the steady state is as follows. In case of inhomogeneous illumination since the shift current vanishes at the boundaries of the illuminated region, opposite charges pile up at the two edges. The gradient due to those piled up charge density generates a diffusion current which acts to homogenize the charge density. In the long time limit the magnitude of this diffusion current approaches the same for the shift current everywhere so that there is no net charge flow at any point reaching a steady state density profile. In case of homogeneous case

however, since the boundary condition is periodic, the charge density always remains homogeneous and diffusion current doesn't arise at all. A similar situation where the photocurrent is compensated by the ohmic current in an open circuit is discussed in Ref. [55]. The cancellation of the shift current by the diffusion current, in case of inhomogeneous excitation profile, relates the shift current to the density profile as:

$$J^{\mathrm{DC}}_{\mathrm{shift}} = -J^{d} = D\,\partial_x \rho \tag{5.20}$$

The charge density $\rho(x)$ can be measured capacitively using the gate shown in Fig. 5.2. This provides a way to measure the shift current without contacts [73].

Using $A_0(x') = \int dx''\, A_0(x'')\delta(x' - x'')$ we can rewrite the expression for the diffusion current (Eq. 5.19) as

$$J^{d}(x) = \alpha \int_{-\infty}^{\infty} dx'\, dx''\, A_0(x')A_0(x'')\, sgn(x - x')\, \partial_{x'}\delta(x' - x'') \tag{5.21}$$

From this expression, it is clear that the diffusion current in case of inhomogeneous excitation profile (i.e. $A_0(x)$ not constant in space) is non-local. This implies that the resultant DC current from the response, given by Eq. 5.2, must contain a spatially non-local contribution.

The non-local response is quite unexpected in the light of response function formalism that is discussed in Sec. 5.2. The time-ordered response functions $\chi_{n,2}$ and $\chi_{n,3}$ can be related by analytic continuation to imaginary time correlation functions, which in turn can be written as derivatives of an effective action [74]. This is similar to finite temperature correlation functions in classical statistical mechanics, where correlation functions decay on the scale of a correlation length [75]. One subtlety to keep in mind here is that $\chi_{n,2}$ and $\chi_{n,3}$ in Eqs. 5.4-5.5 also involve time. However,

analytic continuation from imaginary time suggests that the time-ordered correlations at frequencies larger than temperature are also expected to be local in space and time on a scale determined by correlation lengths and times [74]. Thus one does not expect $\chi_{n,2}$ or $\chi_{n,3}$ to contribute to the non-local response in Eq. 5.21.

Thus, the only term in Eq. 5.2 that can incorporate non-locality of J^d is the term involving OTOC, as appears in the expression of χ_{otoc} in Eq. 5.6. The total current is written as $\langle J \rangle_{\text{DC}} = J^{\text{DC}}_{\text{shift}} + J^d$. Since the shift current response $J^{\text{DC}}_{\text{shift}}$ is local, we can compare the non-local contribution contained in χ_{otoc} with the non-local diffusion response (Eq. 5.18) to write the non-local part of χ_{otoc} as

$$\chi_{\text{otoc}}(r, x_1, x_2) \approx \partial_{x_1} \delta(x_1 - x_2) \frac{(x - x_1)}{4\sqrt{\pi D}} \int_0^t d\tau\, \tau^{-\frac{3}{2}} e^{-\frac{(x-x_1)^2}{4D\tau}} \tag{5.22}$$

for $|x - x_1|, |x - x_2| \gg \xi_{th}$, where ξ_{th} is a thermal correlation length. Thus, the semi classical approach can be used to constrain the non-linear response correlator (Eq. 5.6), which cannot be computed from equilibrium field theory methods. In principle, this response can be computed from a Keldysh field theory approach [17], but it is clear that these correlators will be qualitatively more non-local compared to equilibrium correlators.

5.3.3 Finite voltage and size effect on BPVE

Finite voltage that may be generated in the presence of spatial variations can have an effect on the electron-hole gas as mentioned at the end of Sec. 5.3.1. The carrier density of this electron hole plasma, n, is limited since the rate of exciton generation, for zero temperature, is balanced by recombination rate. We emphasise here that the time

scale for recombination processes to lead to a steady state is inversely proportional to some power of EM amplitude ($\propto 1/A_0^\alpha,\ \alpha > 0$) till which the response function formalism is not applicable. We circumvented this problem in the last sub-section by working at finite temperature. The analysis of the balancing of the recombination process at zero temperature considered in this sub-section, assuming $\alpha = 1$ for free diffusion of carriers, leads to a steady state carrier density with $n^2 \propto A_0^2$. The shift current in the absence of a voltage can only be stable for perfect translation invariance with periodic boundary conditions. Any variations of parameters in the system that would change the shift current, leads to a finite voltage. Let us now consider boundary conditions different from periodic so that a finite voltage V can be generated over length L of the material. The voltage V will lead to a combination of drift and diffusion current among the carriers which is given by

$$J^d = \frac{ne^2\tau_d}{m}\frac{V}{L} \propto \frac{A_0 V}{L} \tag{5.23}$$

where τ_d is the scattering time for the charge carriers.

The combined system with a BPVE together with the drift current can be thought of as a current source J^d in parallel with a resistance $R \propto L/(\tau_d A_0)$. The maximum voltage generated by this process is $V_{\max} = J^{\rm DC}_{\rm shift} R \propto LA_0/\tau_d$. This voltage can become anomalously large in the limit of large L which is consistent with experimental measurements reported in Ref. [76] and the discussions in Ref. [55]. The large open-circuit voltage arises from the large length of the bulk sample. This still doesn't allow Zener tunneling since that is determined by the electric field, $\varepsilon_{\max} = V_{\max}/L \propto A_0/\tau_d$ which can still be kept much smaller than the characteristic electric field corresponding

to the minimum band gap. Specifically, the tunneling rate is given by [77] :

$$\Theta = \exp\left[-c\,\frac{\Delta_{\min}}{V}\frac{L}{\xi}\right] \tag{5.24}$$

where c is a dimensionless constant and $2\Delta_{\min}$ is the minimum band gap and ξ is the length-scale set by the Landau-Zener formula. Thus, the voltage, $V_{\max}$, can exceed the gap as long as $L \gg \xi$. The maximum power that can be extracted from this system is

$$P_{\max,\mathrm{BPVE}} = \left(J^{\mathrm{DC}}_{\mathrm{shift}}\right)^2 R \propto \frac{A_0^3 L}{\tau_d}. \tag{5.25}$$

Note that total incident power scales as $P_{\mathrm{inc}} \propto A_0^2 L$. Thus, despite the high open circuit voltage $V_{\max}$, the efficiency scales as $P_{\max,\mathrm{BPVE}}/P_{\mathrm{inc}} \propto A_0$ and thus is limited by the requirement of A_0 being small. Maximum value of A_0, within the range of validity of this semi classical theory, corresponds to the excitation rate being close to the scattering rate (i.e. $A_0|J^{\perp}_{0,k_D}| \approx \eta$ where k_D is the resonant point for optical transition). However, the shift current generation, being a bulk phenomenon, allows for power absorption throughout the length of the sample. Thus, the total power extracted through current can be enhanced by increasing the exposure length of the bulk sample to the optical excitation. The power conversion efficiency for BPVE also depends on the magnitude of shift current (as in Eq. 5.25) as, $P_{\max,\mathrm{BPVE}} = \alpha A_0^2$, where α is directly proportional to the inversion symmetry breaking factors in the lattice. Hence, materials with strong inversion symmetry breaking will increase power conversion efficiency [64].

5.4 Quantum approach

In this section we go beyond the limit of weak optical excitation by using a more quantum mechanical master equation based approach to calculate the photocurrent.

The problem of the semiconductor in EM field can be described by Eq. 5.1 where $\hat{H}_0$ is the Bloch Hamiltonian as in Eq. 5.7. The EM coupled Hamiltonian (Eq. 5.1) is time periodic with period $T \equiv \frac{1}{\Omega}$.

According to the Floquet theory such time periodic Hamiltonian in Eq. 5.1 can be expressed in Floquet basis as

$$\hat{H}_F = \sum_k \left(\epsilon_k^u \; f_k^{u\dagger} f_k^u + \epsilon_k^d \; f_k^{d\dagger} f_k^d \right) \tag{5.26}$$

where $\epsilon_k^{u,d} \in [0, \Omega]$ are the two quasi energies and $f_k^{u,d}$ correspond to Floquet state operators associated with the conduction and valence bands (see Appendix B.3 for derivation of Floquet spectrum). In Ref. [78], a similar two band system, driven by an external field, has been treated where the system is assumed to couple to a heat bath in a mean-field approach. Here, we include the electron-phonon coupling microscopically in the Hamiltonian and time evolve the system density operator to trace out the phonon modes at the end in order to retain only the electronic degrees of freedom. We compare our expression for the DC current with the same in Ref. [78] at the end of Sec. 5.4.2.

The Hamiltonian describing phonons is given by the corresponding dispersions,

$$\hat{H}_p = \sum_{q,s} \omega_q^s \; a_q^{s\dagger} a_q^s \tag{5.27}$$

where a_q^s is annihilation operator for phonon of mode s and momentum q. In absence of any e-ph coupling the evolution operator for combined e-ph system is given by

$$\hat{U}_0 \equiv \hat{U}_F \otimes \hat{U}_p = e^{-i\hat{H}_F t} \otimes e^{-i\hat{H}_p t}. \tag{5.28}$$

Now the Hamiltonian corresponding to the phonons coupling to the electrons

through the e-ph interaction can be written as

$$\hat{V} = \sum_{q=k-g}^{k,g,s} \left(V_1 \, c_k^\dagger c_g + V_2 \, v_k^\dagger v_g \right) \left(a_q^s + a_{-q}^{s\dagger} \right) \tag{5.29}$$

where $V_1(V_2)$ is the amplitude of intra band scatterings within conduction (valence) band.

The equation of motion for e-ph combined density operator $\hat{\rho}_I(t)$, in the interaction picture basis, that time-evolves according to Eq. 5.28, is given by

$$\partial_t \hat{\rho}_I = -i \Big[\hat{V}_I, \hat{\rho}_I \Big]. \tag{5.30}$$

Note that $\hat{V}_I$ is obtained from Eq. 5.29 by transforming the field operators c_k, v_k and a_q^s to the interaction picture basis. In a standard procedure (outlined in Appendix B.4) to obtain the dynamical equation for the reduced electronic density operator, $\hat{\rho}_I^e$, Eq. 5.30 is solved up to second order in $|V_{1,2}|$ following which the phonon operators are traced out under the Markovian approximation. The resultant equation of motion for $\hat{\rho}_I^e$ becomes

$$\partial_t \hat{\rho}_I^e = -Tr \left\{ \left[\hat{V}_I(t), \int_{-\infty}^{t} dt' \Big[\hat{V}_I(t'), \hat{\rho}_I(t) \Big] \right] \right\}_p . \tag{5.31}$$

$\hat{\rho}_I^e$ can be represented more concretely in terms of its matrix elements in Floquet basis:

$$\Pi_k^{ab}(t) \equiv Tr \left\{ \hat{\rho}_S^e(t) \; f_k^{a\dagger} f_k^b \right\}_e \equiv Tr \left\{ \hat{\rho}_I^e(t) U_F^\dagger \hat{\Theta}_k^{ab} U_F \right\}_e \tag{5.32}$$

where in the last line we have used the cyclic property of trace.

5.4.1 Equation for equilibrium distribution

To obtain an equation of motion for Π_k^{ab} we differentiate Eq. 5.32 and use Eq. 5.31 in the similar way described in [79]. In the process we assume zero temperature for

the phonon bath and translational invariance for the electronic system (see Appendix B.4) to obtain the final form of the equation of motion for Π_k^{ab} to be

$$\partial_t \Pi_k = -i[\Pi_k, F_k] - \Pi_k A_k - A_k^\dagger \Pi_k + (\hat{I} - \Pi_k) D_k + D_k^\dagger (\hat{I} - \Pi_k) \tag{5.33}$$

where F_k can be thought of re-normalized Hamiltonian (local in k) and is given by,

$$F_k^{ab} = \frac{\epsilon_k^u - \epsilon_k^d}{2} \delta^{ab} + i\, V_{kk}^{ba} \sum_g^{\beta\rho} \left[\tilde{V}_{gg}^{\rho\beta} - (\tilde{V}_{gg}^{\beta\rho})^* \right] \Pi_g^{\rho\beta} \tag{5.34}$$

Here the Fourier components of the matrix elements of V and $\tilde{V}$ are given by,

$$\begin{aligned} V_{kg}^{\alpha\beta}(n) &= \sum_m \langle \psi_k^\alpha(m+n) | \hat{V}^S | \psi_g^\beta(m) \rangle, \\ \tilde{V}_{kg}^{\alpha\beta}(n) &= G V_{kg}^{\alpha\beta}(n)\, \Theta\left(\epsilon_k^\alpha - \epsilon_g^\beta + n\Omega\right). \end{aligned} \tag{5.35}$$

where $|\psi_k^\alpha(n)\rangle$ is the nth frequency component of the Floquet state $|\psi_k^\alpha(t)\rangle$ and $\hat{V}^S = \sum_{p,p'} \left(V_1\, c_p^\dagger c_{p'} + V_2\, v_p^\dagger v_{p'} \right)$. G is the constant density of states for the phonon bath and $\Theta(x)$ is the Heaviside step function.

The structure of the tensor D_k,

$$D_k^{ab} \equiv \sum_g^{\beta\rho} V_{kg}^{b\beta} \tilde{V}_{gk}^{\rho a}\, \Pi_g^{\rho\beta} \tag{5.36}$$

in Eq. 5.33, can be understood by considering the diagonal limit of Π_k. In this limit the product $\Pi_g^{\beta\beta}(1 - \Pi_k^{\alpha\alpha})$ along with the corresponding matrix elements represent the probability of scattering from $|\psi_g^\beta\rangle$ to $|\psi_k^\alpha\rangle$ state. The Θ function ensures the initial state has higher quasi energy than the final state which effectively ensures that only the processes dissipating energy to the phonon bath are allowed. Similarly the tensor A_k is involved in reverse scattering processes (for instance from $|\psi_k^\alpha\rangle$ to $|\psi_g^\beta\rangle$ scatterings) and is given by,

$$A_k^{ab} \equiv \sum_g^{\beta\rho} V_{kg}^{b\beta} (\tilde{V}_{kg}^{a\rho})^* \, (\delta^{\beta\rho} - \Pi_g^{\rho\beta}). \tag{5.37}$$

The steady state version of Eq. 5.33 can be obtained by setting $\partial_t \Pi_k^{ab} = 0$. The result is a set of non linear algebraic equations involving $\Pi_k^{\alpha\beta}\Pi_g^{\gamma\delta}$ terms and thus finding exact, simultaneous solutions for $\left\{\Pi_k^{\alpha\beta}\right\}$ is numerically intensive.

We note since the EM amplitude is much smaller than the bandwidth of the electronic energy spectrum ($A_0|J_{0,k}^{\perp}| \ll |\Delta(0) - \Delta(\pi)|$), $\Pi_k^{\alpha\beta}$ differs from its ground state value only in a small region (degeneracy region) of $O[A_0]$ in Brillouin zone. Hence scattering contributions between two degeneracy regions (being smaller by order of A_0) can be ignored.

Since $\Pi_k^{\alpha\beta}$ is close to its ground state value for almost all of the Brillouin zone, we can use the ground state values for the terms $\Pi_g^{\alpha\beta}$ in the tensors $A_k^{\alpha\beta}, D_k^{\alpha\beta}, F_k^{\alpha\beta}$ to linearize the steady state equation of motion which can be readily solved analytically. The linearized equation of motion, for the k points inside the degeneracy region, is obtained to be (see Appendix B.5 for details)

$$i[\tilde{\epsilon}_k, \Pi_k] = -\{M_k, \Pi_k\} + \Lambda_k \tag{5.38}$$

where $\tilde{\epsilon}_k^{ab} = \frac{1}{2}(\epsilon_k^a - \epsilon_k^b)\delta^{ab}$ is the Hamiltonian in Floquet basis. M_k and Λ_k can be deduced from A_k and D_k as defined in Eq. 5.36-5.37, to be

$$\begin{aligned} M_k^{\alpha\beta} &\approx q \sum_{n<0} \langle \psi_k^{\alpha}(n)|\hat{S}_v|\psi_k^{\beta}(n)\rangle + p \sum_{n\geq 0} \langle \psi_k^{\alpha}(n)|\hat{S}_c|\psi_k^{\beta}(n)\rangle, \\ \Lambda_k^{\alpha\beta} &\approx 2q \sum_{n<0} \langle \psi_k^{\alpha}(n)|\hat{S}_v|\psi_k^{\beta}(n)\rangle. \end{aligned} \tag{5.39}$$

Here p and q are effective scattering rates for electrons and holes defined as:

$$p \equiv f_> |V_1|^2 G \;\text{ and }\; q \equiv f_> |V_2|^2 G \tag{5.40}$$

where $f_>$ is the fraction of the Brillouin zone such that $\Omega > 2\Delta_k$. $\hat{S}_v$ and $\hat{S}_c$ are the

projector operators on the valence and conduction band sub spaces respectively defined as

$$\hat{S}_c \equiv \sum_k c_k^\dagger c_k, \quad \hat{S}_v \equiv \sum_k v_k^\dagger v_k. \tag{5.41}$$

The solutions of Eq. 5.38 can be used to calculate current responses.

5.4.2 Expression for the current response

The matrix elements of current operator in the basis of Floquet states are

$$C_k^{\alpha\beta} \equiv \langle \psi_k^\alpha | \hat{J}(t) | \psi_k^\beta \rangle. \tag{5.42}$$

Solving the linear equations in Eq. 5.38 and calculating $C_k^{\alpha\beta}$ according to Eq. 5.42 (Appendix B.6 contains expressions for the steady state matrix elements, $\Pi_k^{\alpha\beta}$ and $C_k^{\alpha\beta}$), we obtain expression for the current response. The AC current can be obtained by computing the $\pm\Omega$ frequency components of $C_k^{\alpha\beta}$ and combining with the steady state solution for $\Pi_k^{\alpha\beta}$ (see Appendix B.6). The resultant response for the AC current up to leading order in electric field amplitude is

$$\begin{aligned} J_k^{\mathrm{AC}}(\Omega) &= A_0 |J_{0,k}^\perp|^2 L_k \left[1 - i + \frac{p+q}{\epsilon_k} + \frac{J_{1,k}^z(\Omega - 2\Delta_k)}{|J_{0,k}^\perp|^2} \right] \\ \text{with} \quad L_k &\equiv \frac{\left(\frac{\Omega}{2} - \Delta_k\right)}{2\epsilon_k} \frac{2q + t_k(p-q)}{(p+q)^2 + (2\epsilon_k)^2} \end{aligned} \tag{5.43}$$

where t_k is given by

$$t_k \equiv Tr\{\Pi_k\} = \frac{1 - \frac{2(p-q)}{p} \frac{A_0^2 |J_{0,k}^\perp|^2}{(p+q)^2 + (2\epsilon_k)^2}}{1 + \frac{(p-q)^2}{pq} \frac{A_0^2 |J_{0,k}^\perp|^2}{(p+q)^2 + (2\epsilon_k)^2}}. \tag{5.44}$$

Similarly, computing the zero frequency component of $C_k^{\alpha\beta}$, we find the DC current up to second order in electric field magnitude to be

$$J_{\mathrm{shift}}^{\mathrm{DC}}(k) = Tr\{\Pi_k C_k\}_e = 2A_0^2 \left(\vec{J}_{0,k} \times \vec{J}_{1,k} \right)_z \frac{2q + t_k(p-q)}{(p+q)^2 + (2\epsilon_k)^2}. \tag{5.45}$$

The total DC current is obtained integrating Eq. 5.45 over Brillouin zone as

$$J^{\rm DC}_{\rm shift} = \frac{1}{2\pi}\int_{BZ} dk\, J^{\rm DC}_{\rm shift}(k). \tag{5.46}$$

If the EM perturbation is the smallest parameter (i.e. $A_0|J^{\perp}_{0,k}| \ll p+q$), from Eq. 5.44 $t_k \approx 1$ which implies

$$\lim_{A_0 \ll (p+q)} J^{\rm DC}_{\rm shift}(k) = 2A_0^2 \left(\vec{J}_{0,k} \times \vec{J}_{1,k}\right)_z \frac{p+q}{(p+q)^2 + (2\epsilon_k)^2}. \tag{5.47}$$

Recognizing the total scattering rate as $\eta = p + q$ and using the limit, $\lim_{A_0 \to 0} \epsilon_k = \frac{\Omega}{2} - \Delta_k$, we recover the semi classical result obtained in Eq. 5.13.

$J^{\rm DC}_{\rm shift}(k)$ can also be evaluated in the opposite limit of weak scattering (i.e. $p, q \ll A_0|J^{\perp}_{0,k}|$) to obtain

$$\lim_{A_0|J^{\perp}_{0,k}| \to 0} \lim_{p,q \ll A_0|J^{\perp}_{0,k}|} J^{\rm DC}_{\rm shift}(k) = \frac{A_0 \left(\vec{J}_{0,k} \times \vec{J}_{1,k}\right)_z}{2|J^{\perp}_{0,k}|} \left[2q + t_k(p-q)\right] \delta(\Omega/2 - \Delta_k). \tag{5.48}$$

Putting this expression into Eq. 5.46 it is easy to see that the resultant DC current scales linearly with the electric field in this limit, i.e. $J^{\rm DC}_{\rm shift} \propto A_0$. This result contradicts the one obtained using the Kubo formula by producing a linear scaling with the external oscillating EM field for the DC current. According to the analytic results in Eq. 5.47 and Eq. 5.48, the DC current response scales quadratically at small A_0 and linearly at large A_0 (smaller and larger than e-ph scattering strengths). On the other hand, the AC response doesn't show any such scaling shift and is always linear in A_0 in the entire perturbative range of A_0. Thus, the linear response is related to equilibrium correlation functions that do not depend critically on the relaxation mechanism. For the DC current, a similar shift of scaling from non-linear to linear, by increasing the

EM field amplitude, is discussed in Ref. [78] where a two band system is coupled to a heat bath. The result obtained in Ref. [78] can be compared to Eq. 5.45 in the case of the effective intra band scattering rates via phonons within the valence and conduction bands being equal, i.e. putting $p = q$ in Eq. 5.44 and Eq. 5.45.

5.5 Numerical evaluation of the weak damping limit

To study how the crossover in scaling occurs between the two regimes for the DC current, we perform the integral in Eq. 5.46 using the expression for $J^{\mathrm{DC}}_{\mathrm{shift}}(k)$ given by Eq. 5.45 for the Rice-Mele model [71]. We also numerically study the scaling property of AC current magnitude for the same model. The Rice-Mele model is described by the following tight binding Hamiltonian [71]

$$\begin{aligned}\hat{H}_0 &= \sum_n \left(h\, a_n^\dagger b_n + h'\, a_n^\dagger b_{n-1} + h.c.\right) + d\left(a_n^\dagger a_n - b_n^\dagger b_n\right) \\ &= \sum_k \Delta_k \left(c_k^\dagger c_k - v_k^\dagger v_k\right) \\ &\text{with} \quad \Delta_k \equiv \sqrt{h^2 + h'^2 + 2hh'\cos(k) + d^2}.\end{aligned} \tag{5.49}$$

The EM vector potential $A(t)$ introduces phases to the hoping terms according to Peierls substitution as

$$a_n^\dagger b_n \to e^{-iA(t)/2}\, a_n^\dagger b_n, \quad a_n^\dagger b_{n-1} \to e^{-iA(t)/2}\, a_n^\dagger b_{n-1}. \tag{5.50}$$

Transforming to Fourier space, the perturbed Hamiltonian, in the atomic (a_k, b_k) basis, becomes

$$\hat{H} = \sum_k \begin{pmatrix} a_k^\dagger & b_k^\dagger \end{pmatrix} \vec{H}_k \cdot \vec{\sigma} \begin{pmatrix} a_k \\ b_k \end{pmatrix} \tag{5.51}$$

with

$$\vec{H}_k = -\left[(h+h')\cos\frac{k-A}{2}, (-h+h')\sin\frac{k-A}{2}, -d\right].$$

In terms of the parameters, $\left(\vec{J}_{0,k} \times \vec{J}_{1,k}\right)_z = -\frac{d}{8\Delta_k}\left(h'^2 - h^2\right)$ where $\vec{J}_{0,k} \equiv \partial_A \vec{H}_k(A)|_{A=0}$ and $\vec{J}_{1,k} \equiv \partial_A^2 \vec{H}_k(A)|_{A=0}$.

The AC current for this Rice-Mele model is obtained by numerical integration of the expression given by Eq. 5.43 over the Brillouin zone with fixed values for p, q. The resulting values for $|J^{\rm AC}|/|J^{\perp}_{0,k_D}|$ are plotted as a function of $2A_0|J^{\perp}_{0,k_D}|/(p+q)$ on a log scale in Fig. 5.3 where k_D is the momentum of the degeneracy point (with the property, $2\Delta_{k_D} = \Omega$). The points on the plot fit to a straight line with slope 1. Thus, the AC current response scales linearly in a range of values from $A_0|J^{\perp}_{0,k_D}| \ll (p+q)$ to $A_0|J^{\perp}_{0,k_D}| \gg p+q$. This scaling is as expected from conventional linear response theory. On the other hand same plot for the shift current, $|J^{\rm DC}_{\rm shift}|/|J^{\perp}_{0,k_D}|$, shows a crossover of scaling with A_0 as shown in Fig. 5.4. In the limit of weak electric field, $\left(\ln\left|2A_0\, J^{\perp}_{0,k_D}/(p+q)\right| < -1\right)$, the points fit to a straight line of slope 2 whereas in the limit of weak scattering $\left(\ln\left|2A_0\, J^{\perp}_{0,k_D}/(p+q)\right| > 1\right)$, the corresponding fit line has slope 1. Therefore, the DC current response indeed shifts scaling from quadratic to linear through a region where the electric field and the scattering strengths are comparable $\left(\ln\left|2A_0\, J^{\perp}_{0,k_D}/(p+q)\right| \sim 0\right)$. Thus the e-ph coupling strength sets an energy scale for

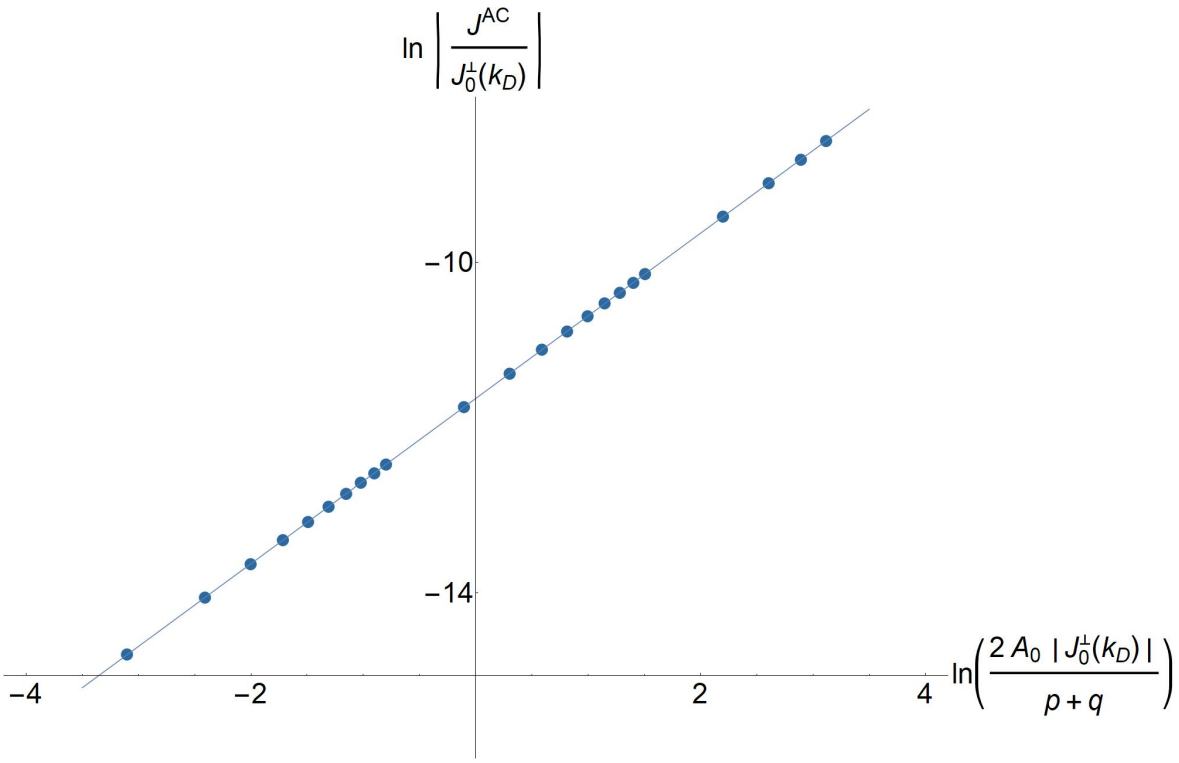

Figure 5.3: $\ln\left|J^{\mathrm{AC}}/|J^{\perp}_{0,k_D}|\right|$ vs $\ln\left|2A_0|J^{\perp}_{0,k_D}|/(p+q)\right|$ plot depicts the scaling dependence of AC current response, J^{AC}, on the EM field amplitude A_0 where J^{AC} is normalized by $|J^{\perp}_{0,k_D}|$, the amplitude of the zeroth order current operator matrix element between conduction and valence band states at the degeneracy point $k = k_D$. p and q are the intraband scattering amplitudes for valence and conduction bands as in Eq. 5.40. The equation for the linear fit is $y = -11.65 + x$.

the EM field strength for a non-linear to linear crossover of the shift current response.

5.6 Conclusion

We have studied an example of a non-linear response i.e. the BPVE in a system with electron-phonon interactions. Since the response is dominated by resonant transitions,

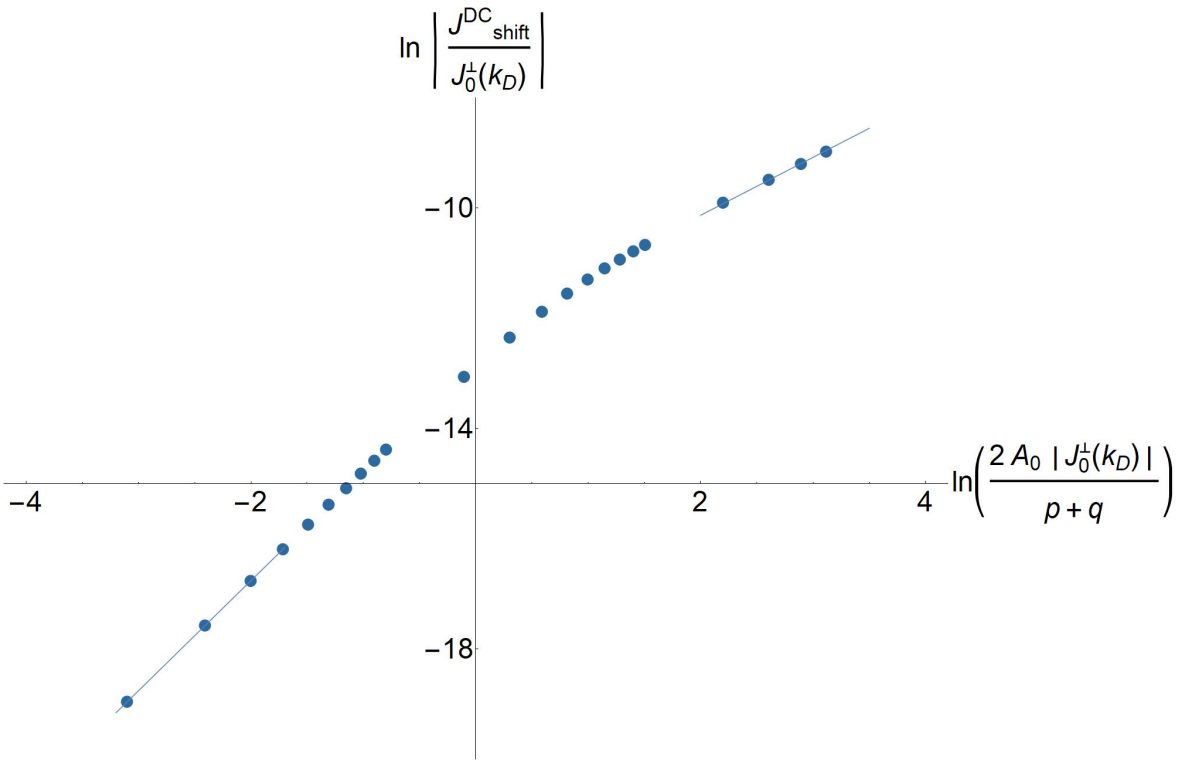

Figure 5.4: $\ln\left|J^{\rm DC}_{\rm shift}/J^{\perp}_{0,k_D}\right|$ vs $\ln\left|2A_0|J^{\perp}_{0,k_D}|/(p+q)\right|$ plot depicts the scaling dependence of the DC current response on the applied EM amplitude. Linear fits in regimes $A_0|J^{\perp}_{0,k_D}| \ll p,q$ and $A_0|J^{\perp}_{0,k_D}| \gg p,q$ show a switch in slope from 2 to 1 as A_0 is increased across the e-ph coupling strength. The linear fit equations are $y=-13.3+2x$ and $y=-12.8+1.05x$ respectively.

we have limited our treatment to a two band model. As we found in Sec. 5.2, the BPVE contains OTOC terms that cannot be computed by simple diagrams. However, in Sec. 5.3, we find that the BPVE can be understood semi classically from the dipole moment of generated excitons. The semi classical limit assumes that the scattering rate is large compared to the driving force. We remedy this in Sec. 5.4 using a master equation approach. From this we find that in the small scattering rate limit the DC current

scales linearly with the vector potential instead of quadratically. This signals that this result is beyond the response function formalism in Sec. 5.2. The AC current doesn't show any such anomalous scaling behavior.

The DC current we obtain in the small A_0 limit is consistent with the non-interacting result for BPVE obtained previously. The breakdown seen in Sec. 5.4 at larger A_0 shows that electron-phonon interaction affects the result in an implicit way. However, what is interesting from comparing to the general response in Sec. 5.2 is that only the $\chi_{n,2}$ term contribute to the shift current in configurations with homogeneous excitation profiles. This term is really conventional linear response of $\hat{J}_0$ to $\hat{J}_1$ contributions in the BPVE and can be computed from equilibrium field theory. However, as shown in Sec. 5.3.2, the situation is quite different for inhomogeneous excitation profiles. In this case, owing to inhomogeneous carrier density generated by the incident light an additional diffusion current response is generated. This modulation of the density profile provides an alternative way to measure the shift current capacitively without the use of contact leads. The diffusion current contribution is not captured by the simple shift current that can be computed from $\chi_{n,2}$ and requires the computation of χ_{otoc}. As discussed in Sec. 5.2, since χ_{otoc} is not a time-ordered correlator, it cannot be computed from conventional equilibrium field theory but rather requires a Keldysh technique. In this work, we have circumvented this using a semi classical approach that is of limited validity in the context of weak interactions to place a constraint on the long ranged part of χ_{otoc} (Eq. 5.22). The full quantum mechanical computation of χ_{otoc} using Keldysh field theory for strongly interacting systems where the semi classical estimate would break down, would be an interesting future direction.

Appendix A

Appendix to Chapter 4

A.1 Comparing the bosonization schemes for the chiral and the physical fermions

In this Appendix we relate the Klein factors, number operators and the bosonic fields that appear in the bosonized expressions for the chiral fermions [Eq. (4.15)] with the same for the physical fermions [Eq. (4.14)]. For this purpose we utilize the relations between the chiral and physical fermions given by Eq. (4.10).

First, let us consider the relation $\psi_{R\uparrow}(x) = \gamma_+(x)$ [Eq. (4.10)]. Substituting the bosonized form for either side of the relation we have,

$$\frac{U_{R\uparrow}}{\sqrt{2\pi\alpha}}\, e^{iN_{R\uparrow}\pi x/L}\, e^{-\frac{i}{\sqrt{2}}(\phi_c-\theta_c+\phi_\sigma-\theta_\sigma)} = \frac{U_+}{\sqrt{2\pi\alpha}}\, e^{iN_+\pi x/L}\, e^{i(\pi+\varphi)x/(2L)}\, e^{-i\phi_+(x)} \tag{A.1}$$

From this equation we can find relations between the Klein factor, number operator and bosonic field. Absorbing the extra phase-factor, $e^{i(\pi+\varphi)x/(2L)}$, on the RHS in the Klein factor we have, $U_{R\uparrow} = e^{i(\pi+\varphi)x/(2L)}\, U_+$, for the number operator $N_{R\uparrow} = N_+$ and lastly for the bosonic field $\phi_+(x) = 1/\sqrt{2}\,(\phi_c - \theta_c + \phi_\sigma - \theta_\sigma)$.

Now we consider the corresponding relation on the other half of the extended manifold, i.e., $x \in [0, -L]$ for γ_+, which reads $\psi_{L\downarrow}(x) = -ie^{i\varphi_0}\, \gamma_+^\dagger(-x)$. Again writing

the bosonized expressions we have

$$\frac{U_{L\downarrow}}{\sqrt{2\pi\alpha}}e^{-iN_{L\downarrow}\pi x/L}\,e^{\frac{i}{\sqrt{2}}(\phi_c+\theta_c-\phi_\sigma-\theta_\sigma)} = -\frac{i}{\sqrt{2\pi\alpha}}e^{i\varphi_0}\,e^{iN_+\pi x/L}U_+^\dagger\,e^{i(\pi+\varphi)x/(2L)}e^{i\phi_+(-x)} \quad \text{(A.2)}$$

In order to perform the same comparison from this expression, the RHS needs to be rearranged such that the Klein factor, $U_+^\dagger$, appears to the left of the exponential number operator, $e^{iN_+\pi x/L}$. Since $U_+^\dagger$ increases N_+ by 1 we have $e^{iN_+\pi x/L}U_+^\dagger = U_+^\dagger e^{i(N_++1)\pi x/L}$. After this re-arrangement we can again relate the variables of the LHS and RHS as here $U_{L\downarrow} = -ie^{i\varphi_0+i(3\pi+\varphi)x/(2L)}\,U_+^\dagger$, $N_{L\downarrow} = -N_+$ and $\phi_+(-x) = 1/\sqrt{2}\,(\phi_c+\theta_c-\phi_\sigma-\theta_\sigma)$.

The exact same arguments can be applied for the relations involving $\gamma_-(x)$, i.e., $\psi_{L\uparrow} = \gamma_-(x)$ and $\psi_{R\downarrow}^\dagger = ie^{i\varphi_0}\,\gamma_-^\dagger(-x)$. Applying the same analysis on these two relations we have $U_{L\uparrow} = e^{i(\pi+\varphi)x/(2L)}\,U_-$, $N_{L\uparrow} = N_-$, $\phi_-(x) = -1/\sqrt{2}\,(\phi_c+\theta_c+\phi_\sigma+\theta_\sigma)$ and $U_{R\downarrow} = ie^{i\varphi_0+i(3\pi+\varphi)x/(2L)}\,U_-^\dagger$, $N_{R\downarrow} = -N_-$, $\phi_-(-x) = -1/\sqrt{2}\,(\phi_c-\theta_c-\phi_\sigma+\theta_\sigma)$. The relations derived in this Appendix is listed in the main text in Eq. (4.16) and Eq. (4.17).

From the relations between the chiral bosons and the spin-charge bosons [Eq. (4.17)] we can now derive the boundary constraints invoking the continuity of $\phi_\pm(x)$ at $x = 0$ and its periodicity at $x = -L, L$. The continuity of $\phi_\pm(x)$ at $x = 0$ implies

$$\begin{aligned}
&\phi_\pm(0^+) = \phi_\pm(0^-) \\
\implies &\pm\left[\phi_c \mp \theta_c + \phi_\sigma \mp \theta_\sigma\right](0) = \pm[\phi_c \pm \theta_c - \phi_\sigma \mp \theta_\sigma](0) \\
\implies &[\theta_c \mp \phi_\sigma](0) = 0 \\
\implies &\theta_c(0) = 0 \quad \phi_\sigma(0) = 0
\end{aligned} \quad \text{(A.3)}$$

Similarly the periodicity condition for the chiral bosons, i.e., $\phi_\pm(L) = \phi_\pm(-L)$, implies

$$\begin{aligned} &\phi_\pm(L) = \phi_\pm(-L) \\ \implies &\pm\left[\phi_c \mp \theta_c + \phi_\sigma \mp \theta_\sigma\right](L) = \pm\left[\phi_c \pm \theta_c - \phi_\sigma \mp \theta_\sigma\right](L) \\ \implies &\left[\theta_c \mp \phi_\sigma\right](L) = 0 \\ \implies &\theta_c(L) = 0 \quad \phi_\sigma(L) = 0 \end{aligned} \tag{A.4}$$

The boundary constraints thus obtained for the spin-charge bosons are listed in the main text in Eq. (4.18).

A.2 Diagonalization of the interacting Hamiltonian

In this Appendix we derive the diagonal second quantized basis for the interacting Hamiltonian given by Eq. (4.20) starting from the expressions for the bosonic fields [Eq. (A.7)]. Using the second quantized expressions we calculate $(\partial_x \phi_{c,\sigma})^2$ and $(\partial_x \theta_{c,\sigma})^2$ and integrating over the length of the system, $\int_0^L dx \ldots$, we obtain the following expressions:

$$\begin{aligned} \int_0^L dx\ (\partial_x \phi_{c,\sigma})^2 &= \pm\frac{\pi}{4}\sum_{n>0} k_n \left[b_n \mp b_{-n} \pm b_n^\dagger - b_{-n}^\dagger\right]^2 \\ \int_0^L dx\ (\partial_x \theta_{c,\sigma})^2 &= \mp\frac{\pi}{4}\sum_{n>0} k_n \left[b_n \mp b_{-n} \mp b_n^\dagger + b_{-n}^\dagger\right]^2 \end{aligned} \tag{A.5}$$

In order to diagonalize we first need to define two sets of bosonic fields as, $c_n \equiv \frac{1}{\sqrt{2}}(b_n - b_{-n})$ and $d_n \equiv \frac{1}{\sqrt{2}}(b_n + b_{-n})$, following which the same terms can be re-written as,

$$\begin{aligned} \int_0^L dx\ (\partial_x \phi_c)^2 &= \frac{\pi}{2}\sum_{n>0} k_n \left[c_n + c_n^\dagger\right]^2 \qquad \int_0^L dx\ (\partial_x \theta_c)^2 = -\frac{\pi}{2}\sum_{n>0} k_n \left[c_n - c_n^\dagger\right]^2 \\ \int_0^L dx\ (\partial_x \phi_\sigma)^2 &= -\frac{\pi}{2}\sum_{n>0} k_n \left[d_n - d_n^\dagger\right]^2 \qquad \int_0^L dx\ (\partial_x \theta_\sigma c)^2 = \frac{\pi}{2}\sum_{n>0} k_n \left[d_n + d_n^\dagger\right]^2 \end{aligned} \tag{A.6}$$

Now expanding the squares in these expressions one can see that it contains $c_n c_n$ ($d_n d_n$) and $c_n^\dagger c_n^\dagger$ ($d_n^\dagger d_n^\dagger$) terms along with the desired diagonal terms. To omit those terms a Bogoliubov transformation is performed which is defined by, $c_n = \cosh\lambda_c\,\gamma_{c,n} + \sinh\lambda_c\,\gamma_{c,n}^\dagger$ and $d_n = \cosh\lambda_\sigma\,\gamma_{\sigma,n} + \sinh\lambda_\sigma\,\gamma_{\sigma,n}^\dagger$ where $e^{\lambda_c} = \sqrt{K_c}$ and $e^{\lambda_\sigma} = 1/\sqrt{K_\sigma}$. Substituting c_n, $c_n^\dagger$ and d_n, $d_n^\dagger$ in terms of $\gamma_{c,n}$, $\gamma_{c,n}^\dagger$and $\gamma_{\sigma,n}$, $\gamma_{\sigma,n}^\dagger$ the diagonal form can be obtained following some algebra as it appears in Eq. (4.22).

Next we express the bosonic fields in terms of the diagonal basis which would be useful to calculate any correlators. The spin-charge bosonic fields have the following expressions in terms of the diagonal basis:

$$\phi_c = \sqrt{\frac{\pi K_c}{L}}\sum_{n>0}\frac{\cos(k_n x)}{\sqrt{k_n}}\left[\gamma_{c,n} + \gamma_{c,n}^\dagger\right] \qquad \theta_c = i\sqrt{\frac{\pi}{K_c L}}\sum_{n>0}\frac{\sin(k_n x)}{\sqrt{k_n}}\left[\gamma_{c,n}^\dagger - \gamma_{c,n}\right]$$
$$\phi_\sigma = i\sqrt{\frac{\pi K_\sigma}{L}}\sum_{n>0}\frac{\sin(k_n x)}{\sqrt{k_n}}\left[\gamma_{\sigma,n}^\dagger - \gamma_{\sigma,n}\right] \qquad \theta_\sigma = \sqrt{\frac{\pi}{K_\sigma L}}\sum_{n>0}\frac{\cos(k_n x)}{\sqrt{k_n}}\left[\gamma_{\sigma,n} + \gamma_{\sigma,n}^\dagger\right] \tag{A.7}$$

These expressions are used in the expressions for the back-scattering terms in order to calculate the matrix elements in Eq. (4.31).

A.3 The linear response function perturbative in impurity potential

In this Appendix we derive the linear response function [Eq. (4.27)] perturbatively up to second order in the impurity Hamiltonian, $\delta\hat{H}_{\rm B}$. We achieve this by finding the dressing of the current operators up to first order and the perturbation of the ground state up to first order in $\delta\hat{H}_B$ and then calculating the correlator in Eq. (4.27).

In the Heisenberg picture the time-dependent current operator is given by

$$\hat{J}_c(t) = U^\dagger(t)\, \hat{J}_c\, U(t) \tag{A.8}$$

where in presence of impurity the time evolution operator $U(t)$ is governed by the entire Hamiltonian of the system,

$$i\partial_t U = \hat{H}_{\rm int} + \delta\hat{H}_{\rm B} \tag{A.9}$$

Defining $U(t) \equiv e^{-i\hat{H}_{\rm int}t}\, \bar{U}\, e^{i\hat{H}_{\rm int}t}$ and substituting in the equation of motion we have,

$$i\partial_t \bar{U} = \delta\bar{H}_{\rm B} \tag{A.10}$$

where $\delta\bar{H}_{\rm B} \equiv e^{i\hat{H}_{\rm int}t}\, \delta\hat{H}_{\rm B}\, e^{-i\hat{H}_{\rm int}t}$. This unitary transformation readily enables us to evaluate $\bar{U}(t)$ up to first order in $\delta\bar{H}_{\rm B}$ as

$$\bar{U}(t) \approx 1 - i\int_0^t dt_1\, \delta\bar{H}_{\rm B}(t_1) \tag{A.11}$$

Putting this form of $\bar{U}(t)$ and using the fact that $\left[\hat{H}_{\rm int}, \hat{J}_c\right] = 0$, we have the following expression for the time-dependent current operator up to linear order:

$$\hat{J}_c(t) = e^{-i\hat{H}_{\rm int}t}\, \bar{U}^\dagger \hat{J}_c \bar{U}\, e^{i\hat{H}_{\rm int}t} = \left[\hat{J}_c - ie^{-i\hat{H}_{\rm int}t} \int^t dt_1 \left[\hat{J}_c, \delta\bar{H}_{\rm B}(t_1)\right] e^{i\hat{H}_{\rm int}t}\right] \tag{A.12}$$

Now we derive the perturbed ground state up to first order in $\delta\hat{H}_B$. The first order perturbation to the ground state, $|\bar{GS}\rangle \equiv |GS\rangle + |\delta G\rangle$, is given by,

$$|\delta G\rangle \approx -\sum_{m\neq GS} \frac{\langle m|\delta\hat{H}_{\rm B}|GS\rangle}{E_m}|m\rangle \tag{A.13}$$

where $|GS\rangle$ is the unperturbed ground state and $\{|m\rangle\}$ are the set of unperturbed excited states. We have assumed the ground state energy to be at zero energy $E_{GS} \equiv 0$.

Using this perturbed ground state and perturbed current operator we now calculate $\langle \hat{J}_c(t)\hat{J}_c(t')\rangle$. We note at this point that $\hat{J}_c|GS\rangle = 0$ and $\langle m|\hat{J}_c|n\rangle = \delta_{mn}\langle m|\hat{J}_c|m\rangle \equiv \delta_{mn}J_c(m)$. Using these and filtering the non-zero contributions up to second order in $\delta\hat{H}_{\rm B}$, we obtain:

$$\langle \bar{GS}|\hat{J}_c(t)\hat{J}_c(t')|\bar{GS}\rangle \approx \sum_m J_c^2(m)\frac{|\langle m|\delta\hat{H}_B|GS\rangle|^2}{E_m^2} + i\int_0^t dt_1\langle GS|\delta\bar{H}_{\rm B}(t_1)\hat{J}_c^2|\delta G\rangle$$
$$- i\int_0^{t'} dt_1\langle \delta G|\hat{J}_c^2\delta\bar{H}_{\rm B}(t_1)|GS\rangle + \int_0^t dt_1\int_0^{t'} dt_2\,\langle GS|\delta\bar{H}_{\rm B}(t_1)\hat{J}_c^2\delta\bar{H}_{\rm B}(t_2)|GS\rangle \tag{A.14}$$

Now substituting $\delta\bar{H}_{\rm B} = e^{i\hat{H}_{\rm int}t}\,\delta\hat{H}_{\rm B}\,e^{-i\hat{H}_{\rm int}t}$ and inserting identities, $\hat{I} \equiv \sum_n |n\rangle\langle n|$, on both sides of the $\hat{J}_c^2$ operator we obtain for the expectation value of the commutator:

$$\langle \bar{GS}|\Big[\hat{J}_c(t),\hat{J}_c(t')\Big]|\bar{GS}\rangle \approx -2i\sum_{m\neq GS} J_c^2(m)\frac{|\langle m|\delta\hat{H}_{\rm B}|GS\rangle|^2}{E_m^2}\,\sin\left[E_m(t-t')\right] \tag{A.15}$$

Since the response function is only a function of the difference between the two times, defining $\tau \equiv t - t'$, we can obtain the Fourier transform in frequency space as:

$$\begin{aligned}\chi(\omega+i\eta) &= \int_{-\infty}^{\infty} d\tau\,\Theta(\tau)\chi(\tau)\\ &\approx -2\sum_m J_c^2(m)\frac{|\langle m|\delta\hat{H}|GS\rangle|^2}{E_m}\,\frac{(E_m^2-\omega^2+\eta^2)+2i\omega\eta}{(E_m^2-\omega^2+\eta^2)^2+4\eta^2\omega^2}\end{aligned} \tag{A.16}$$

In the vanishingly small limit of η, the imaginary part of $\chi(\omega+i\eta)/\omega$ obtains the form given in Eq. (4.31).

A.4 Normal ordering of the exponential operators

In this Appendix we discuss the steps leading to the normal ordered form of the exponential operators, $e^{\pm i(\phi_{c,\sigma}-\theta_{c,\sigma})}\,e^{i(\phi_{c,\sigma}+\theta_{c,\sigma})}$ as they appear in the expressions for

the back-scattering terms in $\delta\hat{H}_{\rm B}$. Since the operators $\phi_{c,\sigma}$, $\theta_{c,\sigma}$ are Hermitian each of the exponent is anti-Hermitian and for an exponential of the form e^A, the anti-Hermitian operator, A can be expressed as $A = \sum_n (a_n\gamma_n^\dagger - a_n^*\gamma_n)$ where γ_n, $\gamma_n^\dagger$ are bosonic annihilation and creation operators. We normal order products of two such non-commuting exponentials, $e^A e^B$. Using Baker-Campbell-Hausdorff (BCH) formula, we obtain the normal ordered form for such a product of operators as follows:

$$\begin{aligned} & e^{\sum_n (a_n\gamma_n^\dagger - a_n^*\gamma_n)} = \prod_n \left[e^{-|a_n|^2/2}\, e^{a_n\gamma_n^\dagger}\, e^{-a_n^*\gamma_n} \right] \\ \implies\ & e^{\sum_n (a_n\gamma_n^\dagger - a_n^*\gamma_n)}\, e^{\sum_n (b_n\gamma_n^\dagger - b_n^*\gamma_n)} = \prod_n e^{-(|a_n|^2+|b_n|^2+2a_n^*b_n)/2}\, e^{(a_n+b_n)\gamma_n^\dagger}\, e^{-(a_n^*+b_n^*)\gamma_n} \end{aligned} \tag{A.17}$$

Now for the case of the charge modes $\gamma_n \equiv \gamma_{c,n}$ whereas for the spin modes $\gamma_n \equiv \gamma_{\sigma,n}$. From Eq. (A.7) we can read off the corresponding coefficients associated with the charge modes to be

$$\begin{aligned} a_{c,n} &= \sqrt{\pi K_c/(2k_nL)}\,[i\cos(k_nx) + \sin(k_nx)/K_c] \\ b_{c,n} &= \sqrt{\pi K_c/(2k_nL)}\,[i\cos(k_nx) - \sin(k_nx)/K_c] \end{aligned} \tag{A.18}$$

and for the spin modes,

$$\begin{aligned} a_{\sigma,n} &= -\sqrt{\pi K_\sigma/(2k_nL)}\ [\sin(k_nx) + i\cos(k_nx)/K_\sigma] \\ b_{\sigma,n} &= -\sqrt{\pi K_\sigma/(2k_nL)}\ [\sin(k_nx) - i\cos(k_nx)/K_\sigma] \end{aligned} \tag{A.19}$$

Now using Eq. (4.26) the normal ordered form of the back-scattering terms are obtained:

$$\begin{aligned} \psi^\dagger_{R\uparrow,\downarrow}\psi_{L\uparrow,\downarrow} = \frac{U_+^\dagger U_-}{2\pi\alpha}\, e^{\mp i(N_+ + N_- + 1)\pi x/L}\, F(x) \\ \prod_n \exp\left[i\sqrt{2\pi K_c/n}\cos(k_nx)\,\gamma_{c,n}^\dagger \mp \sqrt{2\pi K_\sigma/n}\sin(k_nx)\,\gamma_{\sigma,n}^\dagger \right] \\ \exp\left[i\sqrt{2\pi K_c/n}\cos(k_nx)\,\gamma_{c,n} \pm \sqrt{2\pi K_\sigma/n}\sin(k_nx)\,\gamma_{\sigma,n} \right] \end{aligned} \tag{A.20}$$

where $F(x)$ is given by Eq. (4.33) and the expressions for the remaining terms $\psi^{\dagger}_{L\uparrow,\downarrow}\psi_{R\uparrow,\downarrow}$ can be obtained by taking the Hermitian conjugate.

While calculating matrix element of the form $\langle m|\sum_s \psi^{\dagger}_{Rs}\psi_{Ls}|GS\rangle$ using the normal ordered form, the exponential of annihilation operators acting on the ground state becomes unity. Now for a set of occupancies of the bosonic modes in $|m\rangle = |p^c_n, p^\sigma_n\rangle$, from the expansion of exponential of the creation operators, only the term proportional to $\left(\gamma^{\dagger}_{c,n}\right)^{p^c_n}\ \left(\gamma^{\dagger}_{\sigma,n}\right)^{p^\sigma_n}$ contributes. Considering the corresponding pre-factor of that term one can easily obtain the expressions in Eq. (4.32).

Appendix B

Appendix to Chapter 5

B.1 Derivation of second order response

Here we describe the mathematical analysis associated with the derivation of the non-linear response up to second order in the applied EM vector potential. The corresponding perturbation from the minimal coupling is given by $\int dr A(r)\hat{J}(r)$. The space-time notation is condensed in r as $r \equiv (x,t)$.

The response $\langle \hat{J}(r) \rangle$ which is what we are interested in can be written in terms of the trace of the product of the density matrix and the current operator as

$$\langle \hat{J}(r) \rangle = Tr\left\{\tilde{\rho}(t)\mathcal{J}(r)\right\} \tag{B.1}$$

where $\tilde{\rho}(t)$ and $\mathcal{J}(r)$ are the density operator and the current operator respectively in the interaction picture. Using the interaction picture we compute the response up to second order in the applied EM field, $A_0(x)$. We assume that the EM field is turned on from $t = -\infty$ slowly at a rate $\eta \to 0+$ and so for its time-dependence we have $A(r) = A_0(x)\, e^{\eta t}\left(e^{i\Omega t} + e^{-i\Omega t}\right) \equiv A_0(x)\, e^{\eta t}\alpha(t)$.

In the interaction picture the operators are evolved by the unperturbed Hamiltonian for the system, $\hat{H}_0$, as in Eq. 5.1. The evolution of $\tilde{\rho}(t)$ is thus given by:

$$\tilde{\rho}(t) = \tilde{U}(t)\,\tilde{\rho}_{-\infty}\,\tilde{U}^{\dagger}(t) \tag{B.2}$$

where $\tilde{\rho}_{-\infty}$ is initial equilibrium density matrix for the system, before the EM field

was turned on, and $\tilde{U}(t)$ is the interaction picture time evolution operator. The time-evolution operator can be expanded in terms of the applied EM field up to second order:

$$\begin{aligned}\tilde{U}(t) &= \mathcal{T}\left\{e^{-i\int_{r'} A(r')\mathcal{J}(r')}\right\} \\ &\approx 1 - i\int_{-\infty}^{t} dt' \int dx' \left[A(r')\mathcal{J}_0(r') + A^2(r')\mathcal{J}_1(r')\right] \\ &- \frac{1}{2}\int_{-\infty}^{t} dt_1\, dt_2 \int dx_1\, dx_2 A(r_1)A(r_2)\mathcal{T}\left\{\mathcal{J}_0(r_1)\mathcal{J}_0(r_2)\right\}\end{aligned} \tag{B.3}$$

This expansion of $\tilde{U}(t)$ is substituted to the density operator expression and then combining with the current operator the response $\langle\hat{J}(r)\rangle$ can be expressed as powers of the applied EM field, $A(x)$. It turns out in addition to the conventional linear response term, the second-order response, in general, can be split into three terms depending on the space and time dependence of the two powers of the EM field. For the purpose of brevity of the equations we first concisely write the response up to second order with three coefficients which are the associated response functions and then define the response functions later in separate equations.

Thus, the current response has the form:

$$\begin{aligned}\langle\hat{J}(r)\rangle &\approx \langle\hat{J}(r)\rangle_0 + \int_{-\infty}^{\infty} dx'\, A_0(x')\,\chi_{\text{lin}}(r,x') + \int_{-\infty}^{\infty} dx'\, A_0^2(x')\,\chi_{n,2}(r,x') \\ &+ \int_{-\infty}^{\infty} dx_1 dx_2\, A_0(x_1)A_0(x_2)\,\chi_{n,3}(r,x_1,x_2) + \int_{-\infty}^{\infty} dx_1\, dx_2\, A_0(x_1)A_0(x_2)\,\chi_{\text{otoc}}(r,x_1,x_2)\end{aligned} \tag{B.4}$$

where the linear response function, χ_{lin} is given by

$$\chi_{\text{lin}}(r,x') = i\int_{-\infty}^{t} dt'\, e^{\eta t'}\alpha(t')\,\langle[\mathcal{J}_0(r'),\mathcal{J}_0(r)]\rangle_0 \tag{B.5}$$

The non-linear response is split into three terms. The simplest one, denoting by $\chi_{n,2}$,

is given by

$$\chi_{n,2}(r,x') = i\int_{-\infty}^{t} dt'\, e^{2\eta t'}\alpha^2(t')\,\langle[\mathcal{J}_1(r'),\mathcal{J}_0(r)]\rangle_0 \tag{B.6}$$

The $\chi_{n,3}$ response function contains equilibrium time-ordered correlators of three current operators and is given by

$$\chi_{n,3}(r,x_1,x_2) = -\frac{1}{2}\int_{-\infty}^{t} dt_1\, dt_2\, e^{\eta(t_1+t_2)}\alpha(t_1)\alpha(t_2)\,\langle\{\mathcal{T}\{\mathcal{J}_0(r_1)\mathcal{J}_0(r_2)\},\mathcal{J}_0(r)\}\rangle_0 \tag{B.7}$$

Lastly, and most interestingly, $\chi_{\rm otoc}$ contains out of time ordered correlator in its expression

$$\chi_{\rm otoc}(r,x_1,x_2) = \int_{-\infty}^{t} dt_1\, dt_2\, e^{\eta(t_1+t_2)}\alpha(t_1)\alpha(t_2)\,\langle\mathcal{J}_0(r_1)\mathcal{J}_0(r)\mathcal{J}_0(r_2)\rangle_0 \tag{B.8}$$

In all these expressions $\langle..\rangle_0 = Tr\,\{\tilde{\rho}_{-\infty}..\}$ refers to the ground state expectation value. Since there's no current in equilibrium, the first term vanishes (i.e. no current response in absence of any excitation) and one obtains Eq. 5.2. The terms involving $\chi_{\rm otoc}$ adds to the generic non-equilibrium nature of the non-linear response as discussed in the main text.

B.2 Derivation of the shift vector

In this appendix we establish the agreement of DC response for our for the two band case that we have considered in the main text in Eq. 5.13 to the conventional form of the same as obtained before in [59, 60, 61]. The conventional expression for the shift current is given by the following formula:

$$J^{\rm DC}_{\rm shift} = A_0^2\int_{BZ} dk\,|u_k^{cv}|^2\,(\partial_k\phi_k + \alpha_k^{cc} - \alpha_k^{vv}) \tag{B.9}$$

where $u_k^{cv} = \langle c|\hat{u}_k|v\rangle$ and $\hat{u}_k$ is the velocity operator defined as, $\hat{u}_k = \partial_k \hat{H}_{0,k}$. α_k^{cc} (α_k^{vv}) is the Berry connection for the $|c_k\rangle$ ($|v_k\rangle$) state and $\phi_k = -\mathrm{Im}[\ln u_k^{cv}]$. Recalling our result, Eq. 5.13:

$$\lim_{\eta\to 0} J_{\text{shift}}^{\text{DC}} = A_0^2 \int_{BZ} dk\, (\vec{J}_{0,k} \times \vec{J}_{1,k})_z \delta(\Omega - 2\Delta_k),$$

we recognize that we need to show

$$\left(\vec{J}_{0,k} \times \vec{J}_{1,k}\right)_z = |u_k^{cv}|^2 \left(\partial_k \phi_k + \alpha_k^{cc} - \alpha_k^{vv}\right) \tag{B.10}$$

First we observe that

$$\left(\vec{J}_{0,k} \times \vec{J}_{1,k}\right)_z = \mathrm{Im}\left[J_{0,k}^{cv}\, J_{1,k}^{vc}\right] = \mathrm{Im}\left[u_k^{vc}\, (\partial_k \hat{u}_k)^{cv}\right] \tag{B.11}$$

where from the definition of current operators, we have used $\hat{J}_{0,k} = -\hat{u}_k$ and $\hat{J}_{1,k} = \partial_k \hat{u}_k$. Using chain rule for derivatives, we expand the off-diagonal matrix element of $\partial_k \hat{u}_k$ as:

$$(\partial_k \hat{u}_k)^{cv} = \langle c|\partial_k \hat{u}_k|v\rangle = \partial_k u_k^{cv} - \langle \partial_k c|\hat{u}_k|v\rangle - \langle c|\hat{u}_k|\partial_k v\rangle \tag{B.12}$$

$\langle \partial_k c|\hat{u}_k|v\rangle$ can be expanded as:

$$\langle \partial_k c|\hat{u}_k|v\rangle = \langle \partial_k c|\left[\partial_k\left(\hat{H}_{0,k}|v\rangle\right) - \hat{H}_{0,k}|\partial_k v\rangle\right] = \partial_k \epsilon_k^v \langle \partial_k c|v\rangle + \epsilon_k^v \langle \partial_k c|\partial_k v\rangle - \langle \partial_k c|\hat{H}_{0,k}|\partial_k v\rangle \tag{B.13}$$

Now inserting Identity operator, $\hat{I} = |c\rangle\langle c| + |v\rangle\langle v|$ in between for the second and third terms in Eq. B.13 we obtain

$$\langle \partial_k c|\hat{u}_k|v\rangle = -a_k^{cv}\left(u_k^{vv} - a_k^{cc}(\epsilon_k^c - \epsilon_k^v)\right) \tag{B.14}$$

where $a_k^{\alpha\beta} = \langle\alpha|\partial_k\beta\rangle$, $u_k^{vv} = \partial_k\epsilon_k^v$. Interchanging c and v in Eq. B.14 we obtain

$$\langle\partial_k v|\hat{u}_k|c\rangle = -a_k^{vc}\left(u_k^{cc} - a_k^{vv}(\epsilon_k^v - \epsilon_k^c)\right) \tag{B.15}$$

We observe that the Berry phases are related to the $a_k^{\alpha\beta}$ as $\alpha_k^{\alpha\beta} = -ia_k^{\alpha\beta}$. The off-diagonal term a_k^{cv} can be related to the velocity matrix element as

$$a_k^{cv} = \langle c|\partial_k\left(\frac{\hat{H}_{0,k}}{\epsilon_k^v}|v\rangle\right) = -\frac{u_k^{cv}}{\epsilon_k^c - \epsilon_k^v} \tag{B.16}$$

Using complex conjugate of Eq. B.15in Eq. B.12 we obtain:

$$(\partial_k\hat{u})_k^{cv} = \partial_k u_k^{cv} + u_k^{cv}\left[\frac{u_k^{cc} - u_k^{vv}}{\epsilon_k^c - \epsilon_k^v} + a_k^{cc} - a_k^{vv}\right] \tag{B.17}$$

Writing $u_k^{cv} = |u_k^{cv}|e^{-\iota\phi_k}$ we obtain for the imaginary part, $\mathrm{Im}\left[u_k^{vc}\left(\partial_k\hat{u}_k\right)^{cv}\right]$:

$$\mathrm{Im}\left[u_k^{vc}\left(\partial_k\hat{u}_k\right)^{cv}\right] = |u_k^{cv}|^2\left(\partial_k\phi_k + \alpha_k^{cc} - \alpha_k^{vv}\right) = |u_k^{cv}|^2 R_k^{cv} \tag{B.18}$$

where the last equality is the connection of the shift vector to the berry connection as defined in previous literature [59, 60, 61].

B.3 Floquet Theory for two band system

The Floquet theory treats system that are driven with a single frequency time - periodic driving. This is a time domain analogue of the well-known Bloch theorem which treats system with periodicity in real space. According to the Floquet theorem for a system represented by a single frequency time dependent Hamiltonian the solutions for the time dependent Schrodinger equation (TDSE) have the following form

$$|\psi_k^\alpha(t)\rangle = e^{-i\epsilon_k^\alpha t}|\phi_k^\alpha(t)\rangle = e^{-i\epsilon_k^\alpha t}\sum_n |\psi_k^\alpha(n)\rangle e^{\iota n\Omega t}. \tag{B.19}$$

where Ω is the driving frequency and the quasi energy ϵ_k^α can be chosen to belong in a $[0, \Omega]$ interval and $|\phi_k^\alpha(t)\rangle$ is time periodic with period $\frac{2\pi}{\Omega}$.

Substituting the form of Eq. B.19 in TDSE, one obtains the Floquet equations in frequency space as

$$\sum_n (\epsilon_k^\alpha - n\Omega)\,|\psi_k^\alpha(n)\rangle = \sum_m \hat{H}_k(m-n)|\psi_k^\alpha(m)\rangle \tag{B.20}$$

where $\hat{H}^k_{m-n}$ corresponds to the $(m-n)\Omega$ frequency component of the Hamiltonian, $\hat{H}_k$. The eigenvalue solutions for Eq. B.20 produce ϵ_k^α and $|\psi_k^\alpha(n)\rangle$ much like the Bloch's theorem.

For the two band case discussed in the main text, the EM perturbation in frequency space can be written as

$$\hat{H}_p = A_0 \sum_n J^z_{0,k}(c^\dagger_{k,n}c_{k,n\pm1} - v^\dagger_{k,n}v_{k,n\pm1}) + A_0\left[(J^x_{0,k} - \iota J^y_{0,k})c^\dagger_{k,n}v_{k,n\pm1} + h.c.\right] \tag{B.21}$$

where the subscript n correspond to $n\Omega$ frequency component for the c_k, v_k operators

.

For the unperturbed Hamiltonian (Eq. 5.7) the quasi energies are simply

$$\epsilon_k^{u(0)} = \frac{\Omega}{2} + \left|\frac{\Omega}{2} - \Delta_k\right| \quad \text{and} \quad \epsilon_k^{d(0)} = \frac{\Omega}{2} - \left|\frac{\Omega}{2} - \Delta_k\right| \tag{B.22}$$

with the corresponding states as

$$\begin{aligned} |\psi_k^{u(0)}\rangle &= \Theta(\Omega - 2\Delta_k)|c_k(0)\rangle + \Theta(2\Delta_k - \Omega)|v_k(-1)\rangle, \\ |\psi_k^{d(0)}\rangle &= \Theta(\Omega - 2\Delta_k)|v_k(-1)\rangle + \Theta(2\Delta_k - \Omega)|c_k(0)\rangle. \end{aligned} \tag{B.23}$$

If $\Omega = 2\Delta_k$, the quasi energies are degenerate and hence to obtain the effect of perturbation (Eq. B.21) an exact diagonalisation needs to be performed in the vicinity of those degeneracy points.

Up to leading order in A_0, the energy shifts can be obtained by diagonalizing the following matrix given by

$$\tilde{H}_k = \begin{pmatrix} \Delta_k & A_0(J^x_{0,k} - iJ^y_{0,k}) \\ A_0(J^x_{0,k} + iJ^y_{0,k}) & \Omega - \Delta_k \end{pmatrix} \tag{B.24}$$

The corresponding eigenvectors can be used to obtain the Floquet state solutions in time domain as

$$\begin{aligned} |\psi^u_k(t)\rangle &= \frac{e^{-i\epsilon^u_k t}}{\sqrt{1+|x_k|^2}} \left(|c_k\rangle + x_k\, e^{-i\Omega t}|v_k\rangle\right), \\ |\psi^d_k(t)\rangle &= \frac{e^{-i\epsilon^d_k t}}{\sqrt{1+|x_k|^2}} \left(x^*_k\,|c_k\rangle - e^{-i\Omega t}|v_k\rangle\right) \\ \text{with}\quad x_k &= \frac{\frac{\Omega}{2} - \Delta_k + \epsilon_k}{A_0|J^\perp_{0,k}|} \frac{J^x_{0,k} + iJ^y_{0,k}}{|J^\perp_{0,k}|} \\ \text{and}\quad \epsilon^{u,d}_k &= \frac{\Omega}{2} \pm \epsilon_k \quad \text{with}\quad \epsilon_k \equiv \sqrt{\left(\frac{\Omega}{2} - \Delta_k\right)^2 + A_0^2|J^\perp_{0,k}|^2}. \end{aligned} \tag{B.25}$$

This concludes our short description of the application of the Floquet theorem for our simple model of a two band semiconductor that is discussed in the main text.

B.4 Derivation of equation of motion for Π^{ab}_k

Expanding the solution of Eq. 5.30 up to second order in $|V_{1,2}|$ we obtain:

$$\hat{\rho}_I(t) = -i\int_{-\infty}^{t} dt' \left[\hat{V}_I(t'), \hat{\rho}_I(-\infty)\right] - \int_{-\infty}^{t} dt' \left[\hat{V}_I(t'), \int_{-\infty}^{t'} dt'' \left[\hat{V}_I(t''), \hat{\rho}_I(t'')\right]\right] \tag{B.26}$$

Since, the first term contains single power of bath operators, its trace can be dropped. In that case we note, $|\hat{\rho}_I(t'') - \hat{\rho}_I(t')| \approx O[|V_{1,2}|^2]$ and so up to second order in $|V_{1,2}|$, we can replace $\hat{\rho}_I(t'')$ by $\hat{\rho}_I(t')$ in Eq. B.26 to obtain a second order perturbative result

for $\hat{\rho}_I^e(t)$ as

$$\hat{\rho}_I^e(t) \equiv Tr\left\{\hat{\rho}_I^{ep}(t)\right\}_p \approx -Tr\left\{\int_{-\infty}^{t} dt' \left[\hat{V}_I(t'), \int_{-\infty}^{t'} dt'' \left[\hat{V}_I(t''), \hat{\rho}_I^{ep}(t')\right]\right]\right\}_p . \quad \text{(B.27)}$$

Differentiating Eq. B.27 w.r.t. time one obtains Eq. 5.31.

Using cyclic property of trace, from Eq. 5.32, $\partial_t \Pi_k^{ab}$ produces

$$\begin{aligned} \partial_t \Pi_k^{ab} &= -iTr\left\{\left[\hat{\Theta}_k^{ab}, \hat{H}_F\right]\hat{\rho}_S^e(t)\right\}_e \\ &- Tr\left\{\left[\left[\hat{\Theta}_k^{ab}, \hat{U}_0\hat{V}_I(t)\hat{U}_0^\dagger\right], \hat{U}_0\left(\int_{-\infty}^{t} dt'\, \hat{V}_I(t')\right)\hat{U}_0^\dagger\right]\hat{\rho}_S^{ep}(t)\right\}_{ep} . \end{aligned} \quad \text{(B.28)}$$

Noting that $U_F(t)\ f_k^{\alpha\dagger} f_g^\beta\ U_F^\dagger(t) = e^{i(\epsilon_k^\alpha - \epsilon_g^\beta)t}\ f_k^{\alpha\dagger} f_g^\beta$ and $U_p(t)\ a_q^s\ U_p^\dagger(t) = a_q^s\ e^{i\omega_q^s t}$, we obtain

$$U_0\,\hat{V}_I(t)\,U_0^\dagger = \sum_{kg}^{\alpha\beta,s} V_{kg}^{\alpha\beta}(t)\, f_k^{\alpha\dagger} f_g^\beta \left(a_q^s + a_{-q}^{s\dagger}\right) \quad \text{(B.29)}$$

where the interaction matrix elements $V_{kg}^{\alpha\beta}$ between the Floquet states have the form:

$$V_{kg}^{\alpha\beta}(t) = \sum_n \left[\sum_m \langle\Psi_k^\alpha(m+n)|\hat{V}^S|\Psi_g^\beta(m)\rangle\right] e^{in\Omega t} \equiv \sum_n V_{kg}^{\alpha\beta}(n) e^{in\Omega t} \quad \text{(B.30)}$$

And the integral over time for the interaction gives

$$\begin{aligned} \int_{-\infty}^{t} dt'\, \hat{V}_I(t') &= \sum_{p,p'}^{\rho,\sigma,s'} f_p^{\rho\dagger} f_{p'}^\sigma\, V_{pp'}^{\rho\sigma}(n) \frac{a_{q'}^{s'}\, e^{i(\epsilon_{p'p}^{\sigma\rho} + \omega_{q'}^{s'} - n\Omega)t}}{i(\epsilon_{p'p}^{\sigma\rho} + \omega_{q'}^{s'} - n\Omega + i\eta)} \\ &+ \sum_{p,p'}^{\rho,\sigma,s'} f_p^{\rho\dagger} f_{p'}^\sigma\, V_{pp'}^{\rho\sigma}(n) \frac{a_{-q'}^{s'\dagger}\, e^{i(\epsilon_{p'p}^{\sigma\rho} - \omega_{-q'}^{s'} - n\Omega)t}}{i(\epsilon_{p'p}^{\sigma\rho} - \omega_{-q'}^{s'} - n\Omega + i\eta)} \end{aligned} \quad \text{(B.31)}$$

where η is an arbitrarily small imaginary number introduced to regularize the integrals. Considering only the Cauchy principal value one obtains energy conserving delta functions

as follows

$$U_0\left(\int_{-\infty}^{t} dt'\,\hat{V}_I(t')\right)U_0^\dagger$$
$$=\sum_{p,p'}^{\rho,\sigma,s'} f_p^{\rho\dagger} f_{p'}^{\sigma}\, V_{pp'}^{\rho\sigma}(n)\, e^{in\Omega t}\left\{a_{q'}^{s'}\,\delta\left(\epsilon_{p'p}^{\sigma\rho}+\omega_{q'}^{s'}-n\Omega\right)+a_{-q'}^{s'\dagger}\;\delta\left(\epsilon_{p'p}^{\sigma\rho}-\omega_{-q'}^{s'}-n\Omega\right)\right\}. \tag{B.32}$$

Going back to Eq. B.28, the first commutator in the second term gives

$$\begin{aligned}\left[\Theta_k^{ab},\hat{V}_I(t)\right]&=\sum_{g,g'}^{\alpha,\beta,s} V_{gg'}^{\alpha\beta}(t)\,\left(a_q^s+a_{-q}^{s\dagger}\right)\left[f_k^{a\dagger}f_k^b, f_g^{\alpha\dagger}f_{g'}^{\beta}\right]\\&=\sum_{k,g}^{\beta,s} V_{kg}^{b\beta}(t) f_k^{a\dagger}f_g^{\beta}\left(a_q^s+a_{-q}^{s\dagger}\right)-\sum_{k,g}^{\alpha,s} V_{gk}^{\alpha a}(t) f_g^{\alpha\dagger}f_k^b\left(a_q^s+a_{-q}^{s\dagger}\right).\end{aligned} \tag{B.33}$$

In order to calculate the second commutator we need to trace out the bath operators from the product of $\left[\Theta_k^{ab},\hat{V}_I(t)\right]\int_{-\infty}^{t} dt'\,\hat{V}_I(t')$. We use Markovian approximation which assumes that the bath's response time (τ_p) is much shorter than the dynamical time scale due to interaction Hamiltonian, $\tau_p \ll \frac{1}{|V|}$. Consequently, the phonon density matrix remains effectively constant and can be decoupled from the combined density operator as

$$\hat{\rho}_I(t)\approx\hat{\rho}_I^e(t)\otimes\hat{\sigma}_I^p. \tag{B.34}$$

The decoupling implies $\langle aa^\dagger f^\dagger f f^\dagger f\rangle \approx \langle aa^\dagger\rangle\langle f^\dagger f f^\dagger f\rangle$.

Now for the bath using zero temperature expectation values, i.e. $\langle a_q^s a_{q'}^{s'\dagger}\rangle=\delta_{qq'}^{ss'}$ and assuming continuum energy spectrum with a constant density of states, G, for each momentum, i.e. $\sum^s = G\int_0^\infty d\omega_q$, we obtain for the trace of $\left[\Theta_k^{ab},\hat{V}_I(t)\right]\int_{-\infty}^{t} dt'\,\hat{V}_I(t')$,

$$
\begin{aligned}
&Tr\left\{\left[\Theta_k^{ab}, U_0\hat{V}_I(t)U_0^\dagger\right]U_0\left(\int_{-\infty}^{t} dt'\,\hat{V}_I(t')\right)U_0^\dagger\hat{\rho}_S\right\}_{ep}\\
&= G\sum_{k,g,p,p'}^{\rho\sigma\beta} V_{pp'}^{\rho\sigma}(t)\,V_{kg}^{b\beta}(t)\,Tr\left\{f_k^{a\dagger}f_g^{\beta}f_p^{\rho\dagger}f_{p'}^{\sigma}\,\hat{\rho}_S\right\}_e\,\Theta\left(\epsilon_{p'p}^{\sigma\rho}-\omega_q^s-n\Omega\right)\\
&- G\sum_{k,g,p,p'}^{\rho\sigma\beta} V_{pp'}^{\rho\sigma}(t)\,V_{gk}^{\alpha a}(t)\,\langle f_g^{\alpha\dagger}f_k^{b}f_p^{\rho\dagger}f_{p'}^{\sigma}\rangle\,\Theta\left(\epsilon_{p'p}^{\sigma\rho}-\omega_q^s-n\Omega\right)
\end{aligned}
\tag{B.35}
$$

Similar expression can be obtained for the term, $Tr\left\{U_0\left(\int_{-\infty}^{t} dt'\,\hat{V}_I(t')\right)\left[\Theta_k^{ab}, U_0\hat{V}_I(t)U_0^\dagger\right]\right\}_p$.

While tracing out the electrons we assume the electronic system is non interacting and it has translational invariance so that

$$
\begin{aligned}
&\text{(i)}\;\; \langle f_k^{a\dagger}f_g^{\beta}f_p^{\gamma\dagger}f_{p'}^{\delta}\rangle = \delta_{gp}^{\beta\gamma}\langle f_k^{a\dagger}f_{p'}^{\delta}\rangle - \langle f_k^{a\dagger}f_{p'}^{\delta}\rangle\langle f_p^{\gamma\dagger}f_g^{\beta}\rangle + \langle f_k^{a\dagger}f_g^{\beta}\rangle\langle f_p^{\gamma\dagger}f_{p'}^{\delta}\rangle\\
&\text{(ii)}\;\; \langle f_k^{\alpha\dagger}f_g^{\beta}\rangle = \delta_{kg}\langle f_k^{\alpha\dagger}f_k^{\beta}\rangle
\end{aligned}
\tag{B.36}
$$

Using these expressions in Eq. B.35 and putting back to Eq. B.28 we obtain the rate equation as in Eq. 5.33.

B.5 Linearization of master equation

As argued in the main text, away from the degeneracy region only the valence bands are completely occupied which implies

$$\begin{aligned}
&\text{For } g \text{ such that } \Omega > 2\Delta_g \\
&|\psi_g^u\rangle = |v_g(-1)\rangle, \quad |\psi_g^d\rangle = |c_g(0)\rangle; \\
&\Pi_g^{uu} = 1, \quad \Pi_g^{dd} = 0, \quad \Pi_g^{ud} = 0;
\end{aligned} \tag{B.37}$$

$$\begin{aligned}
&\text{For } g \text{ such that } \Omega < 2\Delta_g\text{:} \\
&|\psi_g^u\rangle = |c_g(0)\rangle, \quad |\psi_g^d\rangle = |v_g(-1)\rangle; \\
&\Pi_g^{uu} = 0, \quad \Pi_g^{dd} = 1, \quad \Pi_g^{ud} = 0.
\end{aligned}$$

where the states are written in frequency representation.

Putting $\Pi_g^{\alpha\beta}$ values as input, Eq. 5.33 becomes linear in $\Pi_k^{\alpha\beta}$ since we can ignore scatterings in between two degeneracy regions as its contribution is order of magnitude smaller.

Furthermore, using the state expressions we obtain for the interaction matrix elements,

For g, such that $\Omega > 2\Delta_g$:

$$V_{kg}^{bu}(n)V_{gk}^{u\sigma}(-n) = \langle\Psi_k^b(n-1)|\hat{V}^S|v_g\rangle\langle v_g|\hat{V}^S|\Psi_k^\sigma(n-1)\rangle = \langle\Psi_k^b(n-1)|\hat{S}^v|\Psi_k^\sigma(n-1)\rangle. \tag{B.38}$$

Similarly all other matrix element combinations ($V_{kg}^{\alpha\beta}(n)V_{gk}^{\gamma\delta}(-n)$) for different g points ($\Omega > 2\Delta_g$ $\Omega < 2\Delta_g$) can be obtained.

The additional Θ function puts constraint on the values of n that goes into the summation formula in the steady state rate equation. Consequently the contributions from $g : \Omega < 2\Delta_g$ become $O[A_0^2]$ and thus can be dropped. Incorporating all these, one obtains the M_k and Λ_k matrix elements as in Eq. 5.38.

B.6 Steady state solutions and Current matrix elements

Using the expressions for Floquet states (Eq. B.25) one can easily calculate the M_k and Λ_k matrix elements in Eq. 5.39 to find the solution for Eq. 5.38 in the form, $\Pi_k \equiv t_k \hat{I} + \vec{R}_k \cdot \vec{\sigma}$, where each of the terms are given by

$$t_k = \frac{1 - \frac{2(p-q)}{p} \frac{A_0^2 |J_{0,k}^{\perp}|^2}{(p+q)^2 + (2\epsilon_k)^2}}{1 + \frac{(p-q)^2}{pq} \frac{A_0^2 |J_{0,k}^{\perp}|^2}{(p+q)^2 + (2\epsilon_k)^2}} \tag{B.39}$$

$$R_k^z = \frac{2q + t_k(p-q)}{p+q} \frac{\frac{\Omega}{2} - \Delta_k}{2\epsilon_k} \tag{B.40}$$

$$R_k^{x,y} = -\frac{A_0}{2\epsilon_k} \frac{(p+q)(2q + t_k(p-q))}{(p+q)^2 + (2\epsilon_k)^2} \left(J_{0,k}^{x,y} \mp \frac{2\epsilon_k}{p+q} J_{0,k}^{y,x} \right) \tag{B.41}$$

The current operator, up to first order in A_0, is given by

$$\begin{aligned} \hat{J} = & \sum_k^m \begin{pmatrix} c_{k,m}^\dagger & v_{k,m}^\dagger \end{pmatrix} \left(\vec{J}_{0,k} \cdot \vec{\sigma} \right) \begin{pmatrix} c_{k,m} \\ v_{k,m} \end{pmatrix} \\ & + A_0 \sum_k^m \begin{pmatrix} c_{k,m}^\dagger & v_{k,m}^\dagger \end{pmatrix} \left(\vec{J}_{1,k} \cdot \vec{\sigma} \right) \begin{pmatrix} c_{k,m\pm1} \\ v_{k,m\pm1} \end{pmatrix}. \end{aligned} \tag{B.42}$$

Using the Floquet state expressions (Eq. B.25) along with the current operator definition in frequency space (Eq. B.42), one can obtain the zero frequency component for the matrix elements of current operator, $\tilde{C}_k^{\alpha\beta}(0)$, in $\{\hat{I}, \vec{\sigma}\}$ basis to be

$$\begin{aligned}
&\tilde{C}_k^x(0) \equiv \frac{1}{2}\left(\tilde{C}_k^{ud}(0) + \tilde{C}_k^{du}(0)\right) \\
&\approx \frac{|x_k|}{1+|x_k|^2}\frac{J_{0,k}^x}{|J_{0,k}^\perp|}2J_{0,k}^z - \frac{A_0}{1+|x_k|^2}\left(J_{1,k}^x\, sr_k - J_{1,k}^y\, si_k\right) \\
&\tilde{C}_k^y(0) \equiv -\frac{1}{2i}\left(\tilde{C}_k^{up}(0) - \tilde{C}_k^{du}(0)\right) \\
&\approx \frac{|x_k|}{1+|x_k|^2}\frac{J_{0,k}^y}{|J_{0,k}^\perp|}2J_{0,k}^z - \frac{A_0}{1+|x_k|^2}\left(J_{1,k}^y\, sr_k - J_{1,k}^x\, si_k\right) \\
&\tilde{C}_k^z(0) \equiv \frac{1}{2}\left(\tilde{C}_k^{uu}(0) - \tilde{C}_k^{dd}(0)\right) \\
&\approx \frac{1}{1+|x_k|^2}\left[J_{0,k}^z(1-|x_k|^2) + |x_k|\vec{J}_{0,k}\cdot\vec{J}_{1,k}\right] \\
&\text{with}\;\; sr_k \equiv 1 + \frac{(J_{0,k}^x)^2 - (J_{0,k}^y)^2}{|J_{0,k}^\perp|^2}|x_k|^2 \;\;\text{and}\;\; si_k \equiv \frac{2J_{0,k}^x\, J_{0,k}^y}{|J_{0,k}^\perp|^2}|x_k|^2.
\end{aligned} \tag{B.43}$$

The $\pm\Omega$ frequency components of the matrix elements of current operator, $\tilde{C}_k^{\alpha\beta}(\pm\Omega)$, are given by

$$\begin{aligned}
&\tilde{C}_k^{uu}(\Omega) = \frac{A_0}{2\epsilon_k}\left(|J_{0,k}^\perp|^2 + J_{1,k}^z(\Omega - 2\Delta_k)\right) = \tilde{C}_k^{uu}(-\Omega) \\
&\tilde{C}_k^{dd}(\pm\Omega) = -\tilde{C}_k^{uu}(\pm\Omega) \\
&\tilde{C}_k^{ud}(-\Omega) = -\frac{J_{0,k}^x - iJ_{0,k}^y}{1+|x_k|^2} \quad \tilde{C}_k^{ud}(\Omega) = \frac{|x_k|^2}{1+|x_k|^2}(J_{0,k}^x - iJ_{0,k}^y) \\
&\tilde{C}_k^{du}(\Omega) = \left[\tilde{C}_k^{ud}(-\Omega)\right]^* \quad \tilde{C}_k^{du}(-\Omega) = \left[\tilde{C}_k^{ud}(\Omega)\right]^*.
\end{aligned} \tag{B.44}$$

Bibliography

[1] Y. Li, N. Zaki, V. O. Garlea, A. T. Savici, D. Fobes, Z. Xu, F. Camino, C. Petrovic, G. Gu, P. D. Johnson, J. M. Tranquada, and I. A. Zaliznyak, "Electronic properties of the bulk and surface states of $Fe_{1+y}Te_{1x}Se_x$," *Nature Materials*, vol. 20, pp. 1221–1227, 4 2021.

[2] Z. Shi, X. Hong, H. A. Bechtel, B. Zeng, M. C. Martin, K. Watanabe, T. Taniguchi, Y.-R. Shen, and F. Wang, "Observation of a luttinger-liquid plasmon in metallic single-walled carbon nanotubes," *Nature Photonics*, vol. 9, pp. 515–519, Aug. 2015.

[3] S. Wang, S. Zhao, Z. Shi, F. Wu, Z. Zhao, L. Jiang, K. Watanabe, T. Taniguchi, A. Zettl, C. Zhou, and F. Wang, "Nonlinear luttinger liquid plasmons in semiconducting single-walled carbon nanotubes," *Nature Materials*, vol. 19, pp. 986–991, Sep 2020.

[4] H. Lohani, T. Hazra, A. Ribak, Y. Nitzav, H. Fu, B. Yan, M. Randeria, and A. Kanigel, "Band inversion and topology of the bulk electronic structure in $FeSe_{0.45}Te_{0.55}$," *Phys. Rev. B*, vol. 101, p. 245146, Jun 2020.

[5] Z. Wang, P. Zhang, G. Xu, L. K. Zeng, H. Miao, X. Xu, T. Qian, H. Weng, P. Richard, A. V. Fedorov, H. Ding, X. Dai, and Z. Fang, "Topological nature of the $FeSe_{0.5}Te_{0.5}$ superconductor," *Phys. Rev. B*, vol. 92, p. 115119, Sep 2015.

[6] P. Zhang, K. Yaji, T. Hashimoto, Y. Ota, T. Kondo, K. Okazaki, Z. Wang, J. Wen, G. D. Gu, H. Ding, and S. Shin, "Observation of topological superconductivity on the surface of an iron-based superconductor," *Science*, vol. 360, no. 6385, pp. 182–186, 2018.

[7] D. Wang, L. Kong, P. Fan, H. Chen, S. Zhu, W. Liu, L. Cao, Y. Sun, S. Du, J. Schneeloch, R. Zhong, G. Gu, L. Fu, H. Ding, and H.-J. Gao, "Evidence for majorana bound states in an iron-based superconductor," *Science*, vol. 362, pp. 333–335, 10 2018.

[8] T. Machida, Y. Sun, S. Pyon, S. Takeda, Y. Kohsaka, T. Hanaguri, T. Sasagawa, and T. Tamegai, "Zero-energy vortex bound state in the superconducting topological surface state of Fe(Se,Te)," *Nature Materials*, vol. 18, 8 2019.

[9] G. Xu, B. Lian, P. Tang, X.-L. Qi, and S.-C. Zhang, "Topological superconductivity on the surface of fe-based superconductors," *Phys. Rev. Lett.*, vol. 117, p. 047001, Jul 2016.

[10] T. Barik and J. D. Sau, "Signatures of nontopological patches on the surface of topological insulators," *Phys. Rev. B*, vol. 105, p. 035128, Jan 2022.

[11] Z. Wang, J. O. Rodriguez, L. Jiao, S. Howard, M. Graham, G. D. Gu, T. L. Hughes, D. K. Morr, and V. Madhavan, "Evidence for dispersing 1d majorana channels in an iron-based superconductor," *Science*, vol. 367, no. 6473, pp. 104–108, 2020.

[12] L. Fu and C. L. Kane, "Superconducting proximity effect and majorana fermions at the surface of a topological insulator," *Phys. Rev. Lett.*, vol. 100, p. 096407, Mar 2008.

[13] T. Barik and J. D. Sau, "Half unit cell shift defect induced helical states in fe-based chalcogenide superconductors," *arXiv:2305.15373*.

[14] T. Giamarchi and O. U. Press, *Quantum Physics in One Dimension*. International Series of Monographs on Physics, Clarendon Press, 2004.

[15] T. Barik, Y.-Z. Chou, and J. D. Sau, "Probing spin excitations in a luttinger liquid with superconducting boundaries," *Manuscript in preparation*.

[16] T. Barik and J. D. Sau, "Nonequilibrium nature of nonlinear optical response: Application to the bulk photovoltaic effect," *Phys. Rev. B*, vol. 101, p. 045201, Jan 2020.

[17] A. I. Larkin and Y. N. Ovchinnikov *Sov. Phys. JETP*, vol. 28, no. 6, p. 1200, June 1969.

[18] L. Fu and C. L. Kane, "Topological insulators with inversion symmetry," *Phys. Rev. B*, vol. 76, p. 045302, Jul 2007.

[19] H. Suzuura and T. Ando, "Crossover from symplectic to orthogonal class in a two-dimensional honeycomb lattice," *Phys. Rev. Lett.*, vol. 89, p. 266603, Dec 2002.

[20] L. Fu and C. L. Kane, "Time reversal polarization and a Z_2 adiabatic spin pump," *Phys. Rev. B*, vol. 74, p. 195312, Nov 2006.

[21] Z. Wang, P. Zhang, G. Xu, L. K. Zeng, H. Miao, X. Xu, T. Qian, H. Weng, P. Richard, A. V. Fedorov, H. Ding, X. Dai, and Z. Fang, "Topological nature of the $FeSe_{0.5}Te_{0.5}$ superconductor," *Physical Review B*, vol. 92, 9 2015.

[22] Z. Wang, J. O. Rodriguez, L. Jiao, S. Howard, M. Graham, G. D. Gu, T. L. Hughes, D. K. Morr, and V. Madhavan, "Evidence for dispersing 1d majorana channels in an iron-based superconductor," *Science*, vol. 367, no. 6473, pp. 104–108, 2020.

[23] B. A. Bernevig, T. L. Hughes, and S.-C. Zhang, "Quantum spin hall effect and topological phase transition in HgTe quantum wells," *Science*, vol. 314, 12 2006.

[24] P. Zhang, K. Yaji, T. Hashimoto, Y. Ota, T. Kondo, K. Okazaki, Z. Wang, J. Wen, G. D. Gu, H. Ding, and S. Shin, "Observation of topological superconductivity on the surface of an iron-based superconductor," *Science*, vol. 360, no. 6385, pp. 182–186, 2018.

[25] H. Lohani, T. Hazra, A. Ribak, Y. Nitzav, H. Fu, B. Yan, M. Randeria, and A. Kanigel, "Band inversion and topology of the bulk electronic structure in $FeSe_{0.45}Te_{0.55}$," *Phys. Rev. B*, vol. 101, p. 245146, Jun 2020.

[26] T. Machida, Y. Sun, S. Pyon, S. Takeda, Y. Kohsaka, T. Hanaguri, T. Sasagawa, and T. Tamegai, "Zero-energy vortex bound state in the superconducting topological surface state of Fe(Se,Te)," *Nature Materials*, vol. 18, 8 2019.

[27] X. Wu, S. Qin, Y. Liang, H. Fan, and J. Hu, "Topological characters in $FeTe_{1-x}Se_x$ thin films," *Phys. Rev. B*, vol. 93, p. 115129, Mar 2016.

[28] D. Wang, L. Kong, P. Fan, H. Chen, S. Zhu, W. Liu, L. Cao, Y. Sun, S. Du, J. Schneeloch, R. Zhong, G. Gu, L. Fu, H. Ding, and H.-J. Gao, "Evidence for majorana bound states in an iron-based superconductor," *Science*, vol. 362, pp. 333–335, 10 2018.

[29] X. Chen, M. Chen, W. Duan, X. Zhu, H. Yang, and H.-H. Wen, "Observation and characterization of the zero energy conductance peak in the vortex core state of $FeTe_{0.55}Se_{0.45}$," *http://arxiv.org/abs/1909.01686*, 9 2019.

[30] S. Zhu, L. Kong, L. Cao, H. Chen, M. Papaj, S. Du, Y. Xing, W. Liu, D. Wang, C. Shen, *et al.*, "Nearly quantized conductance plateau of vortex zero mode in an iron-based superconductor," *Science*, vol. 367, no. 6474, pp. 189–192, 2020.

[31] A. Ghazaryan, P. L. S. Lopes, P. Hosur, M. J. Gilbert, and P. Ghaemi, "Effect of zeeman coupling on the majorana vortex modes in iron-based topological superconductors," *Physical Review B*, vol. 101, 1 2020.

[32] A. Y. Kitaev, "Fault-tolerant quantum computation by anyons," *Annals of Physics*, vol. 303, no. 1, pp. 2 – 30, 2003.

[33] C. Nayak, S. H. Simon, A. Stern, M. Freedman, and S. Das Sarma, "Non-abelian anyons and topological quantum computation," *Rev. Mod. Phys.*, vol. 80, pp. 1083–1159, Sep 2008.

[34] C. Nayak, M. Freedman, and S. Das Sarma, "Majorana zero modes and topological quantum computation," *npj Quantum Information*, vol. 1, May 2015.

[35] J.-P. Xu, M.-X. Wang, Z. L. Liu, J.-F. Ge, X. Yang, C. Liu, Z. A. Xu, D. Guan, C. L. Gao, D. Qian, Y. Liu, Q.-H. Wang, F.-C. Zhang, Q.-K. Xue, and J.-F. Jia, "Experimental detection of a majorana mode in the core of a magnetic vortex inside a topological insulator-superconductor $Bi_2Te_3/NbSe_2$ heterostructure," *Phys. Rev. Lett.*, vol. 114, p. 017001, Jan 2015.

[36] H.-H. Sun, K.-W. Zhang, L.-H. Hu, C. Li, G.-Y. Wang, H.-Y. Ma, Z.-A. Xu, C.-L. Gao, D.-D. Guan, Y.-Y. Li, C. Liu, D. Qian, Y. Zhou, L. Fu, S.-C. Li, F.-C. Zhang, and J.-F. Jia, "Majorana zero mode detected with spin selective andreev reflection in the vortex of a topological superconductor," *Phys. Rev. Lett.*, vol. 116, p. 257003, Jun 2016.

[37] Q. Liu, C. Chen, T. Zhang, R. Peng, Y.-J. Yan, C.-H.-P. Wen, X. Lou, Y.-L. Huang, J.-P. Tian, X.-L. Dong, G.-W. Wang, W.-C. Bao, Q.-H. Wang, Z.-P. Yin, Z.-X. Zhao, and D.-L. Feng, "Robust and clean majorana zero mode in the vortex core of high-temperature superconductor $Li_{0.84}Fe_{0.16}(OH)FeSe$," *Phys. Rev. X*, vol. 8, p. 041056, Dec 2018.

[38] R. Song, P. Zhang, and N. Hao, "Phase-manipulation-induced majorana mode and braiding realization in iron-based superconductor Fe(Te,Se)," *Phys. Rev. Lett.*, vol. 128, p. 016402, Jan 2022.

[39] A. Tamai, A. Y. Ganin, E. Rozbicki, J. Bacsa, W. Meevasana, P. D. C. King, M. Caffio, R. Schaub, S. Margadonna, K. Prassides, M. J. Rosseinsky, and F. Baumberger, "Strong electron correlations in the normal state of the iron-based $FeSe_{0.42}Te_{0.58}$ superconductor observed by angle-resolved photoemission spectroscopy," *Phys. Rev. Lett.*, vol. 104, p. 097002, Mar 2010.

[40] F. Chen, B. Zhou, Y. Zhang, J. Wei, H.-W. Ou, J.-F. Zhao, C. He, Q.-Q. Ge, M. Arita, K. Shimada, H. Namatame, M. Taniguchi, Z.-Y. Lu, J. Hu, X.-Y. Cui, and D. L. Feng, "Electronic structure of $Fe_{1.04}Te_{0.66}Se_{0.34}$," *Phys. Rev. B*, vol. 81, p. 014526, Jan 2010.

[41] F. Chen, B. Zhou, Y. Zhang, J. Wei, H.-W. Ou, J.-F. Zhao, C. He, Q.-Q. Ge, M. Arita, K. Shimada, H. Namatame, M. Taniguchi, Z.-Y. Lu, J. Hu, X.-Y. Cui, and D. L. Feng, "Electronic structure of $Fe_{1.04}Te_{0.66}Se_{0.34}$," *Phys. Rev. B*, vol. 81, p. 014526, Jan 2010.

[42] C. W. J. Beenakker, "Universal limit of critical-current fluctuations in mesoscopic josephson junctions," *Phys. Rev. Lett.*, vol. 67, pp. 3836–3839, Dec 1991.

[43] D. L. Maslov, M. Stone, P. M. Goldbart, and D. Loss, "Josephson current and proximity effect in luttinger liquids," *Phys. Rev. B*, vol. 53, pp. 1548–1557, Jan 1996.

[44] C. Wang, X. Liu, L. Kang, B.-L. Gu, Y. Xu, and W. Duan *Phys. Rev. B*, vol. 96, p. 115147, 2017.

[45] I. O. Kulik, "Macroscopic Quantization and the Proximity Effect in S-N-S Junctions," *Soviet Journal of Experimental and Theoretical Physics*, vol. 30, p. 944, Jan. 1969.

[46] M. Fabrizio and A. O. Gogolin, "Interacting one-dimensional electron gas with open boundaries," *Phys. Rev. B*, vol. 51, pp. 17827–17841, Jun 1995.

[47] P. De Gennes, *Superconductivity Of Metals And Alloys*. CRC Press, 2018.

[48] J. Bardeen and J. L. Johnson, "Josephson current flow in pure superconducting-normal-superconducting junctions," *Phys. Rev. B*, vol. 5, pp. 72–78, Jan 1972.

[49] J. W. Harter, Z. Y. Zhao, J. Yan, D. G. Mandrus, and D. Hsieh *Science*, vol. 356, p. 295, 2017.

[50] Z. Li and F. Nori *Phys. Rev. B*, vol. 99, p. 155146, 2019.

[51] K. W. Kim, T. Morimoto, and N. Nagaosa *Phys. Rev. B*, vol. 95, p. 035134, 2017.

[52] F. de Juan, A. G. Grushin, T. Morimoto, and J. E. Moore *Nat. Commun.*, vol. 8, p. 15995, 2017.

[53] V. I. Belinicher, V. K. Malinovskii, and B. I. Sturman *Sov. Phys. JETP*, vol. 46 (2), p. 362, August 1977.

[54] V. I. Belinicher *Sov. Phys. JETP*, vol. 48 (2), p. 322, August 1978.

[55] V. I. Belinicher and B. I. Struman *Usp. Fiz. Nauk*, vol. 130, pp. 415–458, 1980.

[56] B. I. Struman and V. M. Fridkin, *The photovoltaic and photorefractive effects in noncentrosymmetric materials*. Philadelphia: Gordon and Breach Science Publishers, 1992.

[57] V. M. Fridkin, *Photoferroelectrics*. Berlin: Springer-Verlag Berlin Heidelberg, 1979.

[58] E. Deyo, L. E. Golub, E. L. Ivchenko, and B. Spivak *arxiv.org/pdf/0904.1917.pdf*.

[59] J. Sipe and A. Shkrebtii *Phys. Rev. B*, vol. 61, p. 5337, 2000.

[60] R. von Baltz and W. Kraut *Phys. Rev. B*, vol. 23, p. 10, 1981.

[61] T. Morimoto and N. Nagaosa *Phys. Rev. B*, vol. 94, p. 035117, 2016.

[62] A. M. Cook, B. M. Fregoso, F. de Juan, S. Coh, and J. E. Moore *Nat. Commun.*, vol. 8, p. 14176, 2017.

[63] L. Z. Tan and A. M. Rappe *Phys. Rev. Lett.*, vol. 116, p. 237402, 2016.

[64] B. M. F. T. Rangel, B. S. Mendoza, T. Morimoto, J. E. Moore, and J. B. Neaton *Phys. Rev. Lett.*, vol. 119, p. 067402, 2017.

[65] S. M. Young and A. M. Rappe *Phys. Rev. Lett.*, vol. 109, p. 116601, 2012.

[66] L. Z. Tan, F. Zheng, S. M. Young, F. Wang, S. Liu, and A. M. Rappe *npj Computational materials*, vol. 2, p. 16026, 2016.

[67] M. Nakamura, S. Horiuchi, F. Kagawa, N. Ogawa, T. Kurumaji, Y. Tokura, and M. Kawasaki *Nat. Commun.*, vol. 8, p. 281, 2017.

[68] S.-J. Gong, F. Zheng, and A. M. Rappe *Phys. Rev. Lett.*, vol. 121, p. 017402, 2018.

[69] N. Ogawa, M. Sotome, Y. Kaneko, M. Ogino, and Y. Tokura *Phys. Rev. B*, vol. 96, p. 241203(R), 2017.

[70] G. B. Osterhoudt, L. K. Diebel, M. J. Gray, X. Yang, J. Stanco, X. Huang, B. Shen, N. Ni, P. J. W. Moll, Y. Ran, and K. S. Burch *Nature Materials*, vol. 18, p. 471, 2019.

[71] M. J. Rice and E. J. Mele *Phys. Rev. Lett.*, vol. 49, p. 1455, 1982.

[72] J. O. Daniel E. Parker, Takahiro Morimoto and J. E. Moore *Phys. Rev. B*, vol. 99, p. 045121, 2019.

[73] V. Yakovenko, *private communication*.

[74] S. Sachdev, *Quantum Phase Transitions*. Cambridge, UK: Cambridge University Press, second edition ed., 2011.

[75] N. Goldenfeld, *Lectures on phase transitions and the renormalization group*. Boca Raton: CRC Press, 2018.

[76] V. Fridkin *Crystallographic Reports*, vol. 46, no. 4, pp. 654–658, 2001.

[77] C. Zener *Proc. R. Soc. London A*, vol. 137, p. 696, 1932.

[78] T. Morimoto and N. Nagaosa *Science Advances*, vol. 2, p. e1501524, 2016.

[79] T. Iadecola, T. Neupert, and C. Chamon *Phys. Rev. B*, vol. 91, p. 235133, 2015.